STATE OF THE CLIMATE IN 2023

GLOBAL OCEANS

G. C. Johnson and R. Lumpkin, Eds.

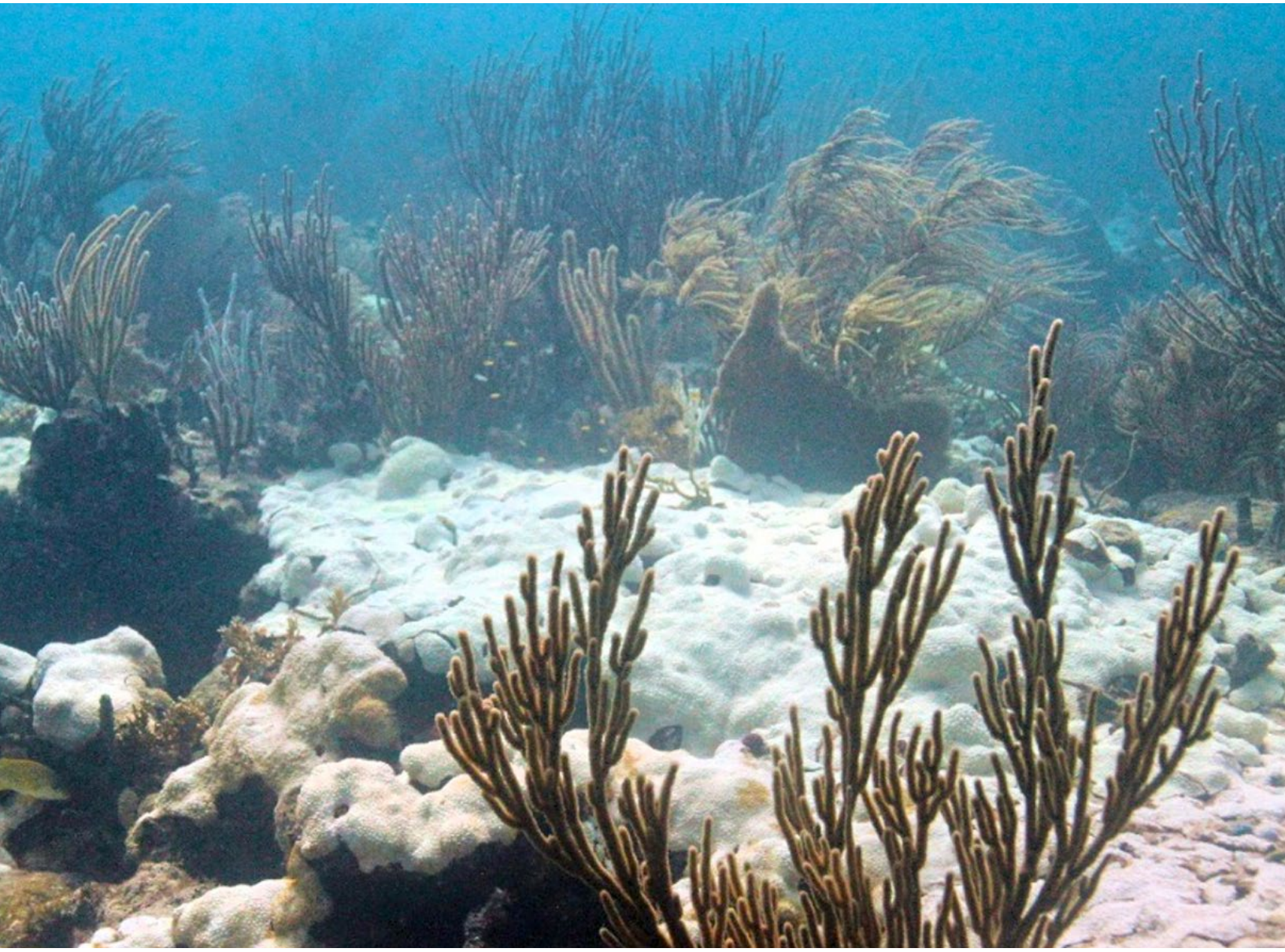

Special Online Supplement to the *Bulletin of the American Meteorological Society* Vol. 105, No. 8, August 2024

https://doi.org/10.1175/BAMS-D-24-0100.1

Corresponding author: Gregory C. Johnson / Gregory.C.Johnson@noaa.gov

STATE OF THE CLIMATE IN 2023
Global Oceans

Editors

Jessica Blunden
Tim Boyer

Chapter Editors

Anthony Arguez
Josh Blannin
Peter Bissolli
Kyle R. Clem
Howard J. Diamond
Matthew L. Druckenmiller
Robert J. H. Dunn
Catherine Ganter
Nadine Gobron
Gregory C. Johnson
Rick Lumpkin
Rodney Martinez
Ademe Mekonnen
John B. Miller
Twila A. Moon
Marilyn N. Raphael
Carl J. Schreck III
Laura Stevens
Richard L. Thoman
Kate M. Willett
Zhiwei Zhu

Technical Editor

Lukas Noguchi

BAMS Special Editor for Climate

Timothy DelSole

American Meteorological Society

Cover Credit:
Extensive bleaching of the soft coral Palythoa caribaeorum on Emerald Reef, Key Biscayne, Florida. Image credit: NOAA

How to cite this document:
Global Oceans is one chapter from the *State of the Climate in 2023* annual report and is available from https://doi.org/10.1175/BAMS-D-24-0100.2. Compiled by NOAA's National Centers for Environmental Information, *State of the Climate in 2023* is based on contributions from scientists from around the world. It provides a detailed update on global climate indicators, notable weather events, and other data collected by environmental monitoring stations and instruments located on land, water, ice, and in space. The full report is available from https://doi.org/10.1175/2024BAMSStateoftheClimate.1.

Citing the complete report:
Blunden, J. and T. Boyer, Eds., 2024: "State of the Climate in 2023". *Bull. Amer. Meteor. Soc.*, **105** (8), Si–S483 https://doi.org/10.1175/2024BAMSStateoftheClimate.1.

Citing this chapter:
Johnson, G. C. and R. L. Lumpkin, Eds., 2024: Global Oceans [in "State of the Climate in 2023"]. *Bull. Amer. Meteor. Soc.*, **105** (8), S156–S213, https://doi.org/10.1175/BAMS-D-24-0100.1.

Citing a section (example):
Yu, L., C. Liu, P. W. Stackhouse, J. Garg, and R. A. Weller, 2024: Global ocean heat, freshwater, and momentum fluxes [in "State of the Climate in 2023"]. *Bull. Amer. Meteor. Soc.*, **105** (8), S178–S182, https://doi.org/10.1175/BAMS-D-24-0100.1.

Editor and Author Affiliations (alphabetical by name)

Alexander, Michael A., NOAA/OAR Physical Sciences Laboratory, Boulder, Colorado

Amaya, Dillon J., NOAA/OAR Physical Sciences Laboratory, Boulder, Colorado

Beckley, Brian, KBR, Inc., Greenbelt, Maryland; NASA Goddard Space Flight Center, Greenbelt, Maryland

Boyer, Tim, NOAA/NESDIS National Centers for Environmental Information, Silver Spring, Maryland

Bringas, Francis, NOAA/OAR Atlantic Oceanographic and Meteorological Laboratory, Miami, Florida

Carter, Brendan R., Cooperative Institute for Climate, Ocean, and Ecosystem Studies, University of Washington, Seattle, Washington; NOAA/OAR Pacific Marine Environmental Laboratory, Seattle, Washington

Cetinić, Ivona, NASA Goddard Space Flight Center, Greenbelt, Maryland; Universities Space Research Association, Columbia, Maryland

Chambers, Don P., College of Marine Science, University of South Florida, St. Petersburg, Florida

Chan, Duo, School of Ocean and Earth Science, University of Southampton, Southampton, United Kingdom

Cheng, Lijing, International Center for Climate and Environment Sciences, Institute of Atmospheric Physics, Chinese Academy of Sciences, Beijing, China

Dong, Shenfu, NOAA/OAR Atlantic Oceanographic and Meteorological Laboratory, Miami, Florida

Elipot, Shane, Rosenstiel School of Marine, Atmospheric, and Earth Science, University of Miami, Miami, Florida

Feely, Richard A., NOAA/OAR Pacific Marine Environmental Laboratory, Seattle, Washington

Franz, Bryan A., NASA Goddard Space Flight Center, Greenbelt, Maryland

Fu, Yao, School of Earth and Atmospheric Sciences, Georgia Institute of Technology, Atlanta, Georgia

Gao, Meng, NASA Goddard Space Flight Center, Greenbelt, Maryland; Science Systems and Applications Inc., Lanham, Maryland

Garg, Jay, ADNET Systems, Inc., Hampton, Virginia

Giglio, Donata, Department of Atmospheric and Oceanic Sciences, University of Colorado Boulder, Boulder, Colorado

Gilson, John, Scripps Institution of Oceanography, University of California San Diego, La Jolla, California

Goes, Marlos, Cooperative Institute for Marine and Atmospheric Studies, University of Miami, Miami, Florida; NOAA/OAR Atlantic Oceanographic and Meteorological Laboratory, Miami, Florida

Graham, Garrett, Cooperative Institute for Satellite Earth System Studies, North Carolina State University, Asheville, North Carolina

Hamlington, Benjamin D., Center for Coastal Physical Oceanography, Old Dominion University, Norfolk, Virginia

Hobbs, Will, Australian Antarctic Program Partnership, Institute for Marine and Antarctic Studies; Australian Research Council Centre of Excellence for Climate Extremes, University of Tasmania, Hobart, Australia

Hu, Zeng-Zhen, NOAA/NWS National Centers for Environmental Prediction Climate Prediction Center, College Park, Maryland

Huang, Boyin, NOAA/NESDIS National Centers for Environmental Information, Asheville, North Carolina

Ishii, Masayoshi, Department of Atmosphere, Ocean, and Earth System Modeling Research, Meteorological Research Institute, Japan Meteorological Agency, Tsukuba, Japan

Jacox, Michael G., NOAA/NMFS Southwest Fisheries Science Center, Monterey, California; NOAA/OAR Physical Sciences Laboratory, Boulder, Colorado

Jersild, Annika, Earth System Science Interdisciplinary Center/Cooperative Institute for Satellite Earth System Studies, University of Maryland, College Park, Maryland

Jevrejeva, Svetlana, National Oceanography Centre, Liverpool, United Kingdom

Johns, William E., Rosenstiel School of Marine, Atmospheric, and Earth Science, University of Miami, Miami, Florida

Johnson, Gregory C., NOAA/OAR Pacific Marine Environmental Laboratory, Seattle, Washington

Killick, Rachel. E., Met Office Hadley Center, Exeter, United Kingdom

Kuusela, Mikael, Department of Statistics and Data Science, Carnegie Mellon University, Pittsburg, Pennsylvania

Landschützer, Peter, Flanders Marine Institute, InnovOcean Campus, Ostend, Belgium

Leuliette, Eric, NOAA/NWS NCWCP Laboratory for Satellite Altimetry, College Park, Maryland

Liu, Chao, Department of Physical Oceanography, Woods Hole Oceanographic Institution, Woods Hole, Massachusetts

Locarnini, Ricardo, NOAA/NESDIS National Centers for Environmental Information, Silver Spring, Maryland

Lozier, Susan M., School of Earth and Atmospheric Sciences, Georgia Institute of Technology, Atlanta, Georgia

Lumpkin, Rick, NOAA/OAR Atlantic Oceanographic and Meteorological Laboratory, Miami, Florida

Lyman, John M., Cooperative Institute for Marine and Atmospheric Research, University of Hawaii, Honolulu, Hawaii; NOAA/OAR Pacific Marine Environmental Laboratory, Seattle, Washington

Merrifield, Mark A., Scripps Institution of Oceanography, University of California San Diego, La Jolla, California

Mishonov, Alexey, Earth System Science Interdisciplinary Center/Cooperative Institute for Satellite Earth System Studies, University of Maryland, College Park, Maryland; NOAA/NESDIS National Centers for Environmental Information, Silver Spring, Maryland

Mitchum, Gary T., College of Marine Science, University of South Florida, St. Petersburg, Florida

Moat, Ben I., National Oceanography Centre, Southampton, United Kingdom

Nerem, R. Steven, Colorado Center for Astrodynamics Research, Cooperative Institute for Research in Environmental Sciences, University of Colorado Boulder, Boulder, Colorado

Oe, Mitsuho, Japan Meteorological Agency, Tokyo, Japan

Perez, Renellys C., NOAA/OAR Atlantic Oceanographic and Meteorological Laboratory, Miami, Florida

Pita, Ivenis, Cooperative Institute for Marine and Atmospheric Studies, University of Miami, Miami, Florida; NOAA/OAR Atlantic Oceanographic and Meteorological Laboratory, Miami, Florida

Purkey, Sarah G., Scripps Institution of Oceanography, University of California San Diego, La Jolla, California

Reagan, James, NOAA/NESDIS National Centers for Environmental Information, Silver Spring, Maryland

Sato, Kanako, Japan Agency for Marine-Earth Science and Technology, Yokosuka, Japan

Schmid, Claudia, NOAA/OAR Atlantic Oceanographic and Meteorological Laboratory, Miami, Florida

Smeed, David A., National Oceanography Centre, Southampton, United Kingdom

Smith, Ryan H., NOAA/OAR Atlantic Oceanographic and Meteorological Laboratory, Miami, Florida

Stackhouse, Jr., Paul W., NASA Langley Research Center, Hampton, Virginia

Sukianto, Thea, Department of Statistics and Data Science, Carnegie Mellon University, Pittsburg, Pennsylvania

Sweet, William, NOAA/NOS Center for Operational Oceanographic Products and Services, Silver Spring, Maryland

Thompson, Philip R., Cooperative Institute for Marine and Atmospheric Research, University of Hawaii, Honolulu, Hawaii

Editor and Author Affiliations (continued)

Triñanes, Joaquin A., Laboratory of Systems, Technological Research Institute, Universidad de Santiago de Compostela, Campus Universitario Sur, Santiago de Compostela, Spain; Cooperative Institute for Marine and Atmospheric Studies, University of Miami, Miami, Florida; NOAA/OAR Atlantic Oceanographic and Meteorological Laboratory, Miami, Florida

Volkov, Denis L., Cooperative Institute for Marine and Atmospheric Studies, University of Miami, Miami, Florida; NOAA/OAR Atlantic Oceanographic and Meteorological Laboratory, Miami, Florida

Wanninkhof, Rik, NOAA/OAR Atlantic Oceanographic and Meteorological Laboratory, Miami, Florida

Weller, Robert A., Department of Physical Oceanography, Woods Hole Oceanographic Institution, Woods Hole, Massachusetts

Westberry, Toby K., Oregon State University, Corvallis, Oregon

Widlansky, Matthew J., Cooperative Institute for Marine and Atmospheric Research, University of Hawaii, Honolulu, Hawaii

Willis, Josh K., Jet Propulsion Laboratory, California Institute of Technology, Pasadena, California

Yin, Xungang, NOAA/NESDIS National Centers for Environmental Information, Asheville, North Carolina

Yu, Lisan, Department of Physical Oceanography, Woods Hole Oceanographic Institution, Woods Hole, Massachusetts

Zhang, Huai-min, NOAA/NESDIS National Centers for Environmental Information, Asheville, North Carolina

Editorial and Production Team

Allen, Jessicca, Graphics Support, Cooperative Institute for Satellite Earth System Studies, North Carolina State University, Asheville, North Carolina

Camper, Amy V., Graphics Support, Innovative Consulting and Management Services, LLC, NOAA/NESDIS National Centers for Environmental Information, Asheville, North Carolina

Haley, Bridgette O., Graphics Support, NOAA/NESDIS National Centers for Environmental Information, Asheville, North Carolina

Hammer, Gregory, Content Team Lead, Communications and Outreach, NOAA/NESDIS National Centers for Environmental Information, Asheville, North Carolina

Love-Brotak, S. Elizabeth, Lead Graphics Production, NOAA/NESDIS National Centers for Environmental Information, Asheville, North Carolina

Ohlmann, Laura, Technical Editor, Innovative Consulting and Management Services, LLC, NOAA/NESDIS National Centers for Environmental Information, Asheville, North Carolina

Noguchi, Lukas, Technical Editor, Innovative Consulting and Management Services, LLC, NOAA/NESDIS National Centers for Environmental Information, Asheville, North Carolina

Riddle, Deborah B., Graphics Support, NOAA/NESDIS National Centers for Environmental Information, Asheville, North Carolina

Veasey, Sara W., Visual Communications Team Lead, Communications and Outreach, NOAA/NESDIS National Centers for Environmental Information, Asheville, North Carolina

3. Table of Contents

3. GLOBAL OCEANS

G. C. Johnson and R. Lumpkin, Eds.

a. Overview

—G. C. Johnson and R. Lumpkin

A shift out of a triple-dip La Niña to a neutral state starting in February and then into an El Niño in May that strengthened through December was a defining event for the global oceans in 2023. Global sea-surface temperatures (SSTs) shattered record highs in 2023, as did global ocean heat content and global sea level. The global average annual SST anomaly was 0.13°C above the previous record set in 2016, also an El Niño year. Marine heatwaves were exceptionally widespread, long-lived, and record-breaking in many regions. From 2022 to 2023, ocean heat content from 0 dbar to 2000 dbar increased at a rate equivalent to ~0.7 W m^{-2} of energy applied over the surface area of Earth, and global sea level increased by ~8.1 mm. In addition, the oceans absorbed anthropogenic carbon at a rate of ~3.8 Pg C yr^{-1} in 2023, with concomitant acidification, slightly above the 2013–22 average of ~3.5 Pg C yr^{-1}. In haiku form:

El Niño roars in,
with record marine heatwaves,
as seas warm, rise, sour.

In the Pacific Ocean—with the shift from La Niña to El Niño—SSTs, sea-surface salinities, 0-m–2000-m ocean heat content, and sea level all increased in the eastern tropical Pacific and decreased in the western tropical Pacific from 2022 to 2023. Additionally, surface currents across the equatorial Pacific in 2023 were strongly anomalously eastward. Fluxes of carbon dioxide from ocean to atmosphere were lower than average during 2023 off Peru and out to about 120°W in the equatorial Pacific as a result of the strong coastal El Niño but higher than average in the central equatorial Pacific. Chlorophyll-*a* anomalies were low in a wedge in the central and eastern equatorial Pacific, but high just outside that wedge. The Pacific Decadal Oscillation continued in a negative phase in 2023 that has held since 2020, with SST, ocean heat content, and sea-surface height values in the center of the North Pacific basin all higher than average, and relatively lower values around the edges. A persistent 2020–23 poleward shift in the Kuroshio extension continued to be evident in both ocean heat content and zonal surface current anomalies.

The Indian Ocean dipole shifted from negative in 2022 to positive in 2023, with positive SST, ocean heat content, and sea-level anomalies in the west and negative anomalies in the east. Surface currents near the equator were anomalously westward. The most notable sea-surface salinity anomaly feature in the Indian Ocean in 2023 was a strong fresher-than-average patch north of the equator.

In the Atlantic, SST, ocean heat content, and sea level were all well above average across much of the basin in 2023, with below-average values of ocean heat content anomalies southeast of Greenland, and lower values of SST anomalies east of northern Greenland. In 2023, the anomaly patterns were similar to 2022, but values were generally higher. Sea-surface salinity was anomalously high in salty subtropical regions and anomalously low around the Intertropical Convergence Zone and in the Greenland Sea. Updates in time series of the Atlantic meridional overturning circulation at various latitudes revealed little direct evidence of a trend over the past few decades.

Arctic Ocean conditions for 2023 are discussed in detail in Chapter 5, and Southern Ocean conditions in Chapter 6.

b. Sea-surface temperature

—X. Yin, B. Huang, D. Chan, G. Graham, Z.-Z. Hu, and H.-M. Zhang

Here, sea-surface temperature (SST) changes over 2022–23 and their uncertainties are assessed over the global ocean and individual ocean basins based on the ERSSTv5 (Huang et al. 2017) and two supporting datasets, the HadSST.4.0.1.0 (Kennedy et al. 2019) and the DOISST v2.1 (Huang et al. 2021). SST anomalies (SSTAs) are calculated relative to 1991–2020 monthly climatologies. The magnitudes of SSTAs are compared against the SST standard deviations (SDs) during the baseline period.

With a transition from a triple-dip 2020–23 La Niña (Li et al. 2023; Jiang et al. 2023) to El Niño in early 2023, historic high SST records were continually set starting in March and throughout the remainder of the year. Based on the DOISST v2.1, daily global mean SST rapidly climbed, with a trend of 0.15°C per month during the first quarter of 2023 following the dissipation of La Niña. The daily mean global SST first surpassed the previous record-high SST of 18.78°C, which was set on 6 March 2016. Then, after a series of SST record-breaking events, it reached a new record high of 18.82°C on 4 April 2023. After a seasonal decrease during April–May, daily global mean SST began to rise again, setting new records numerous times until 22 August, when a historic high daily global mean SST of 18.99°C was recorded. Meanwhile, since 13 March 2023 and continuing through the end of the year, daily global mean SST had remained record high for the time of year in DOISST v2.1, which started in 1981. For the year as a whole, 2023 was the warmest year in the 170-year records, since the pre-industrial era, according to ERSSTv5, a monthly SST product with records since January 1854. The annual average global mean SSTA in 2023 was +0.41±0.01°C, exceeding that of 2016, now the second warmest year (+0.28±0.01°C) on record by a large margin. The warmest 10 years for the global ocean in terms of SST were all from the last decade, with SSTAs ranging from +0.13±0.1°C to +0.41±0.1°C. Here, the uncertainties, reported as 95% confidence intervals, were estimated by a Student's t-test using a 500-member ERSSTv5 ensemble with randomly drawn parameter values within reasonable ranges during SST reconstructions (Huang et al. 2015, 2020).

Annual mean SSTAs for 2023 (Fig. 3.1a) were above normal nearly globally, resulting in large-area, long-duration, high-magnitude marine heatwaves in many regions (see Sidebar 3.1 for details). With the emerging El Niño, SSTAs in the eastern tropical Pacific were more than +0.5°C near the dateline and increased eastward to more than +2°C off the coast of South America. In the North Pacific, except off the west coast of North America, SSTAs in the midlatitudes were above normal, reaching +1.5°C, consistent with a negative phase of the Pacific Decadal Oscillation (PDO; Mantua and Hare 2002). From the subtropical South Pacific to the Southern Ocean, SSTAs were positive (+0.5°C) in the west but negative (–0.5°C) in the east. The Indian Ocean in 2023 was characterized by warm anomalies in the west and weak cold anomalies in the east, congruent with an annual mean Indian Ocean dipole (IOD; Saji et al. 1999) index of +0.59, ranking as the third highest annual mean since 1854. Over nearly the entire Atlantic Ocean, SSTs were above normal, with SSTAs ranging between +0.2°C and +1.0°C. The North Atlantic Ocean was particularly warm, with SSTAs above +1.0°C in the east. SSTAs of +0.5°C and above were observed in parts of the Arctic and sub-Arctic Oceans, particularly in the Barents Sea.

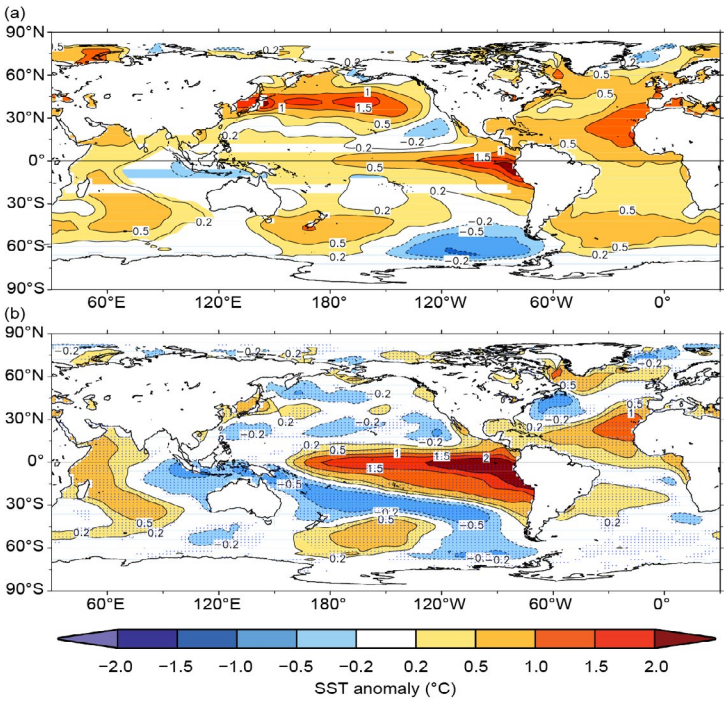

Fig. 3.1. (a) Annual mean sea-surface temperature anomalies (SSTAs) in 2023 (°C) and (b) difference of annual mean SSTAs from the previous year (2023 minus 2022; °C). SSTAs are based on the 1991–2020 climatologies. The stippled areas in panel (b) indicate that the 2023-minus-2022 SSTA difference is significant at 95% confidence.

The 2023-minus-2022 SST differences (Fig. 3.1b) show a substantial SST increase in the equatorial Pacific, owing to the transition from La Niña conditions in 2022 to the onset of El Niño in 2023. In this region, SSTs increased by over 1.5°C near the dateline and by more than 2.0°C east of approximately 120°W. In the Indian Ocean, the east–west SSTA contrast was reversed, consistent with negative monthly IOD indices in 2022 and positive values in 2023. In 2023, the North Atlantic became extremely warm with record-high monthly mean SSTs for the time of year observed from March through December in the 170-year records of the ERSSTv5. Over the subtropical North Atlantic and the seas south of Greenland, SSTs in 2023 were substantially higher than in 2022. The western North Atlantic Ocean in 2023 was substantially colder than in 2022 (Fig. 3.1b) but still warmer than the climatology (Fig. 3.1a).

Seasonal mean SSTAs (Fig. 3.2) provide detailed insights into the evolution of SSTs in 2023. The seasonal changes of the El Niño–Southern Oscillation (ENSO) status were reflected in the tropical Pacific Ocean seasonal SSTAs. In boreal winter (Fig. 3.2a), the La Niña conditions resulted in SSTAs between –1.0°C and –0.2°C. In boreal spring (Fig.3.2b), high positive SSTAs (+1.0°C to +2.0°C) in the seas off the coast of South America were associated with a strong coastal El Niño, a precursor of a basin-scale El Niño (Rasmusson and Carpenter 1982; Hu et al. 2019). El Niño conditions emerged in May and were evident in the June–August average (Fig. 3.2c) and strengthened in boreal autumn (Fig. 3.2d), as indicated by the progressive westward expansion of the positive SSTAs (>+1.0°C) and the areas encompassed by the 1-SD and 2-SD SSTA contours. Along with the ENSO phase transition, the zonal SSTA contrast in the tropical Indian Ocean also shifted from near-neutral IOD status in winter (+0.11 during January–March) to a strong positive IOD status in summer (+0.71 during July–September) and autumn (+1.34 during October–December). In the winter and spring, SSTAs in the North Pacific Ocean were mainly positive with negative values along the coastal and tropical regions (Figs. 3.2a,b). In the summer

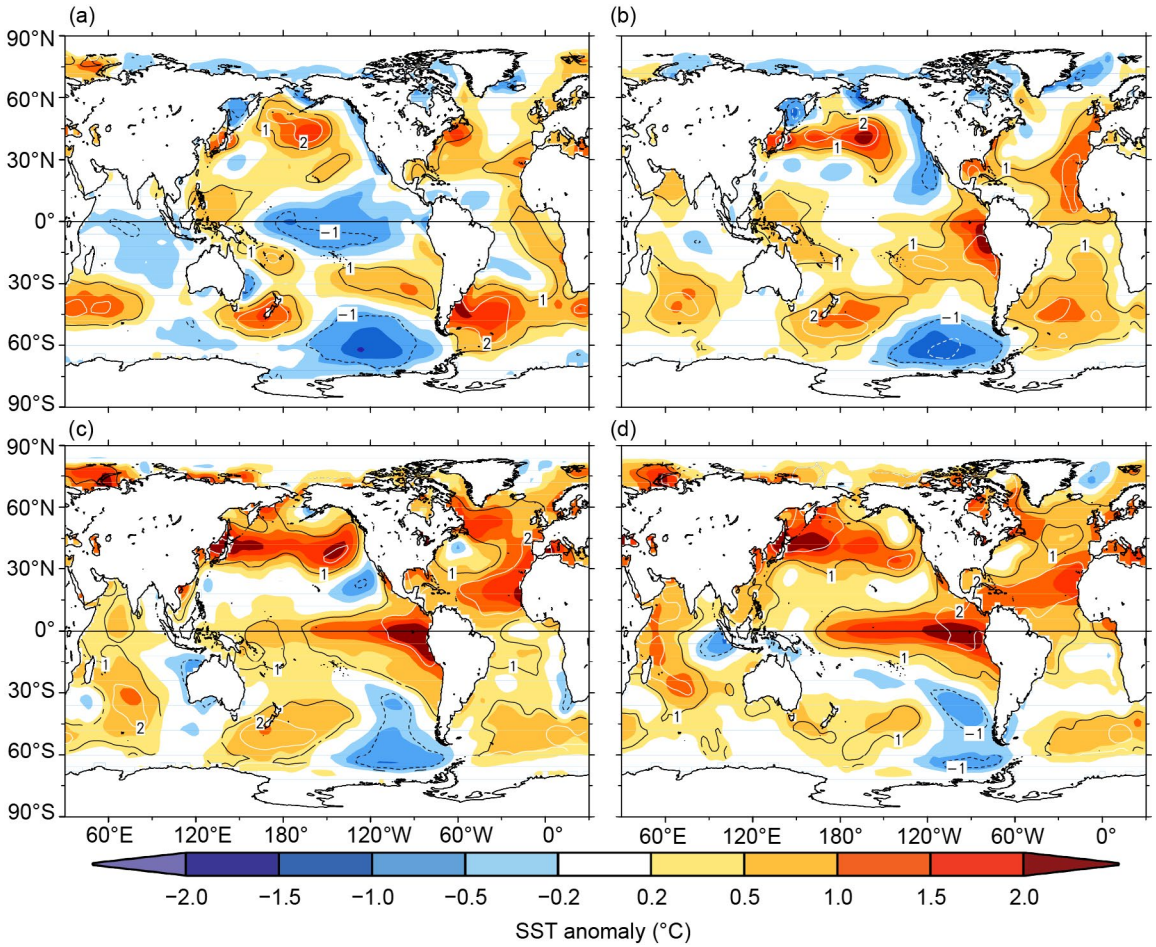

Fig. 3.2. Seasonal mean sea-surface temperature anomalies (SSTAs) of ERSSTv5 (°C; shading) for (a) Dec 2022–Feb 2023, (b) Mar–May 2023, (c) Jun–Aug 2023, and (d) Sep–Nov 2023. The normalized seasonal mean SSTAs based on the seasonal mean standard deviations (SDs) over 1991–2020 are indicated by contours of –2 (dashed white), –1 (dashed black), 1 (solid black), and 2 (solid white).

and autumn, SSTAs were almost all positive in the basin and exceeded +1.0°C in the midlatitudes (Figs. 3.2c,d). For the North Atlantic Ocean, positive SSTAs were dominant year round and were particularly strong in the summer and autumn with SSTAs greater than +0.5°C over almost the entire basin. Large warming areas with SSTAs greater than 2-SD were found in the southeastern part of the basin during the summer to autumn seasons, which significantly contributed to the record-breaking SSTs in the North Atlantic during that time. In the Southern Hemisphere, a sizable area of positive SSTA appeared in each ocean. Between the Pacific and Atlantic positive SSTA areas, there was a comparable area of negative SSTA in the South Pacific and Southern Ocean. This feature was present in all seasons, but it was most pronounced in boreal winter (Fig. 3.2a).

For the global ocean, southern oceans, and individual basins in the tropics and subtropics, annual mean SSTA time series based on ERSSTv5 (Fig. 3.3) are presented with time series from HadSST.4.0.1.0 and DOISST v2.1. The estimated linear trends (Table 3.1) for the period beginning at the start of the twenty-first century (2000–23) are larger than those for the longer period that dates to the mid-twentieth century (1950–2023) both globally and in all regions. The global ocean trends are 0.17±0.06°C decade^{-1} and 0.11±0.01°C decade^{-1} for the two periods, respectively. On a regional scale, for 1950–2023 vs. 2000–23 trends, the warming acceleration rate is the highest for the North Pacific (0.10±0.04°C decade^{-1} vs 0.42±0.13°C decade^{-1}) and the lowest for the tropical Indian Ocean (0.14±0.02°C decade^{-1} vs 0.16±0.08°C decade^{-1}). During the longer term since 1950, trends among different regions are comparable, ranging from 0.10°C decade^{-1} to 0.14°C decade^{-1} with the highest in the tropical Indian Ocean. During the shorter term since 2000, trends among different regions are widely spread, ranging from 0.14°C decade^{-1} to 0.42°C decade^{-1}, with the highest trend in the North Pacific.

Table 3.1. Linear trends (°C decade^{-1}) of global and regional mean annual sea-surface temperature anomalies (SSTAs) from ERSSTv5, HadSST4.0.1.0, and DOISST v2.1. The uncertainties at 95% confidence are estimated by accounting for the effective sampling number quantified by lag-1 autocorrelation on the degrees of freedom of annual mean SSTs.

Product	Region	1950–2023	2000–23
HadSST.4.0.1.0	Global	0.12±0.02	0.19±0.06
DOISST	Global	N/A	0.20±0.05
ERSSTv5	Global	0.11±0.01	0.17±0.06
ERSSTv5	Tropical Pacific (30°S–30°N)	0.10±0.03	0.14±0.14
ERSSTv5	North Pacific (30°N–60°N)	0.10±0.04	0.42±0.13
ERSSTv5	Tropical Indian (30°S–30°N)	0.14±0.02	0.16±0.08
ERSSTv5	North Atlantic (30°N–60°N)	0.13±0.05	0.21±0.10
ERSSTv5	Tropical Atlantic (30°S–30°N)	0.12±0.02	0.18±0.08
ERSSTv5	Southern oceans (30°S–60°S)	0.10±0.02	0.14±0.05

The global trends calculated from different SST products, ranging from 0.11°C decade^{-1} to 0.12°C decade^{-1} over 1950–2023 and from 0.17°C decade^{-1} to 0.20°C decade^{-1} over 2000–23, are statistically indistinguishable considering the uncertainties (Table 3.1). As shown in Fig. 3.3, the departures of both DOISST v2.1 and HadSST.4.0.1.0 from ERSSTv5 are largely within the 2-SD

envelope (gray shading), which was derived from a 500-member ensemble analysis based on ERSSTv5 and centered on the SSTAs of ERSSTv5 (Huang et al. 2020). Particularly, the long-term SST time series of the North Atlantic shows large interdecadal variations (Fig. 3.3f). These variations are mainly associated with the Atlantic Multidecadal Variability (AMV; Schlesinger and Ramankutty 1994; Yin et al. 2023).

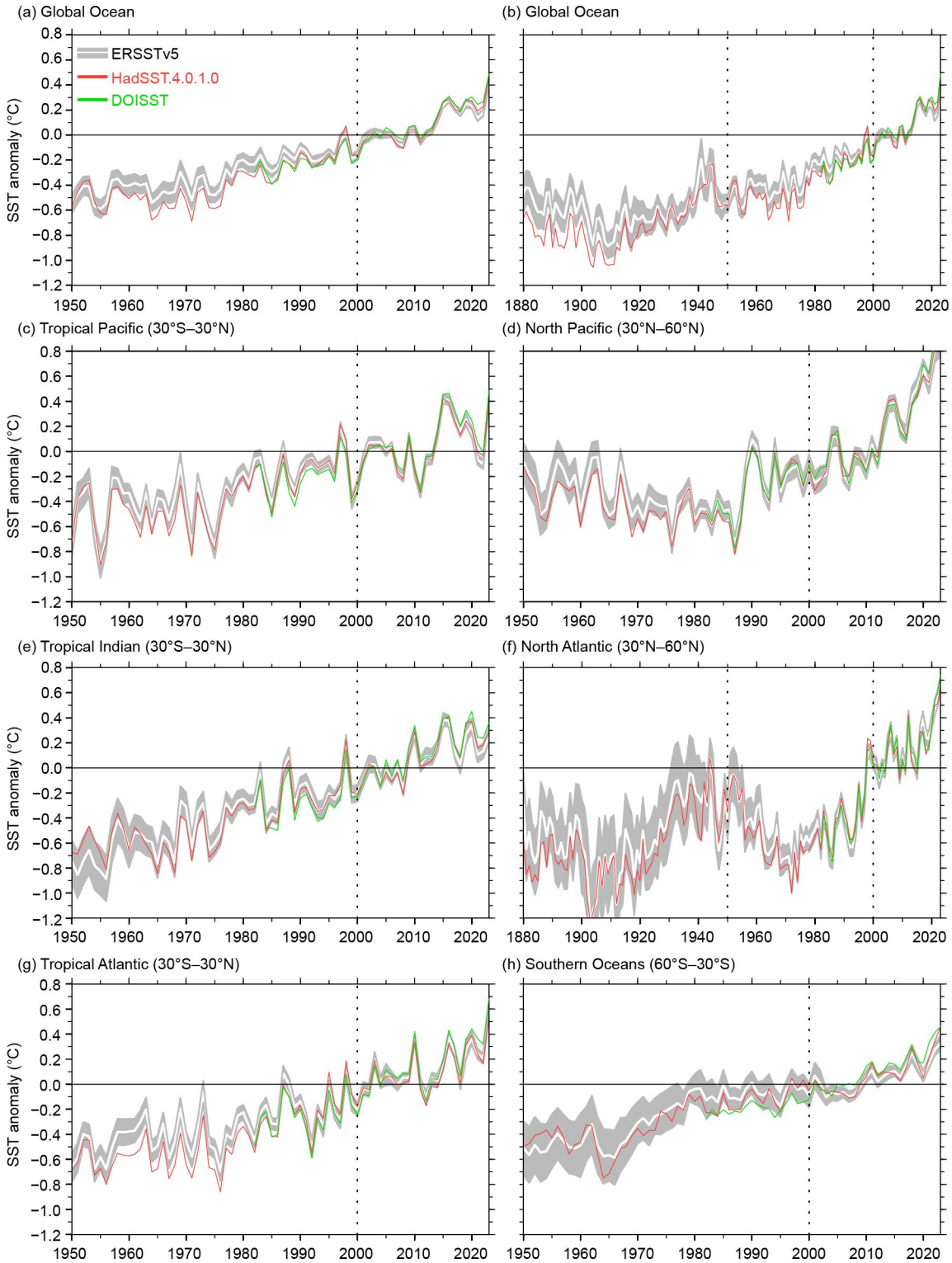

Fig. 3.3. Annual mean sea-surface temperature anomalies (SSTAs; °C) of ERSSTv5, (solid white) and 2 standard deviations (SDs, gray shading) of ERSSTv5, SSTAs of HadSST.4.0.1.0 (solid red), and SSTAs of DOISST (solid green) for the period 1950–2023 except for (b) and (f). (a) Global ocean, (b) global ocean in 1880–2023, (c) tropical Pacific, (d) North Pacific, (e) tropical Indian, (f) North Atlantic for 1880–2023, (g) tropical Atlantic, and (h) Southern oceans (30°S–60°S). The 2-SD envelope was derived from a 500-member ensemble analysis based on ERSSTv5 and centered on SSTAs of ERSSTv5. The years 2000 and 1950 are indicated by dotted vertical black lines.

Sidebar 3.1: **Marine heatwaves in 2023**

M. G. JACOX, D. J. AMAYA, AND M. A. ALEXANDER

Marine heatwaves (MHWs)—transient periods of exceptionally high ocean temperatures—have been linked to a myriad of impacts on ocean physics, chemistry, and biology, and consequently on human economies and communities (e.g., Holbrook et al. 2019; Smith et al. 2021, 2023). These events, which can last many months, are often defined as exceeding the 90th percentile of sea-surface temperature anomalies (SSTAs) for a given location and time of year (Hobday et al. 2016). As a result, MHWs are observed roughly 10% of the time at any given location by definition. However, MHW events in 2023 far exceeded what is considered "typical", with record-breaking extremes (in terms of area coverage and intensity) observed all over the world. Here, we use monthly SST data from NOAA's OISSTv2.1 dataset (Reynolds et al. 2007; Huang et al. 2021), using a 1991–2020 climatological period, to illustrate the exceptional global coverage and intensity of MHWs in 2023.

Marine heatwaves were widespread in 2023, with most of the ocean experiencing extreme temperatures at some point during the year (Fig. SB3.1). More than 85% of the global ocean experienced an MHW for at least one month in 2023, 50% experienced four months or more of MHWs, and 29% experienced six months or more. For reference, over 1982–2023, 44% of the ocean experienced at least one MHW month each year on average, with just 11% and 4% experiencing at least four and six months, respectively. Several regions, including the eastern tropical and North Atlantic, the Sea of Japan, the Arabian Sea, the Southern Ocean near New Zealand, and the eastern tropical Pacific, were in an MHW state for at least 10 months of 2023. These areas accounted for ~4% of the global ocean, or ~10 times the area that would typically experience such persistent MHWs in an average year (0.4%). In contrast, the regions with anomalously low MHW activity were concentrated in the northeast Pacific (subtropics, Gulf of Alaska, eastern Bering Sea), the eastern Indian Ocean, the Arctic Ocean, and several sectors of the Southern Ocean (Fig. SB3.1).

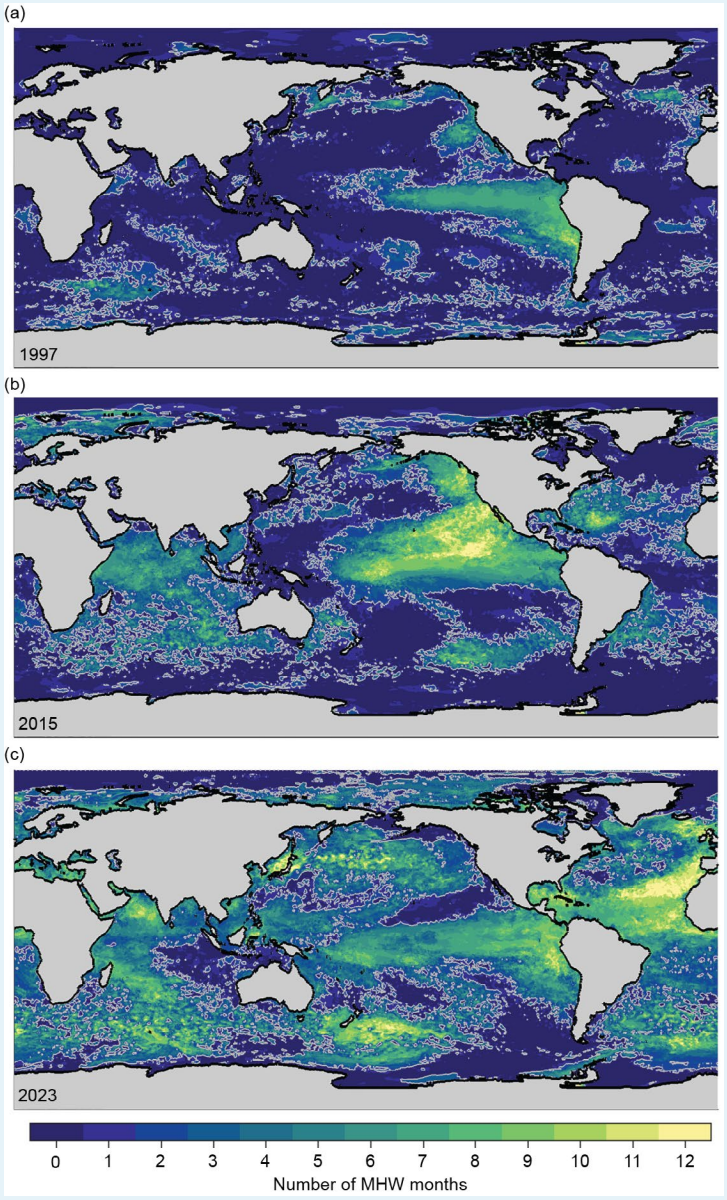

Fig. SB3.1. Global marine heatwave (MHW) coverage during three years characterized by the onset of major El Niño events: (a) 1997, (b) 2015, and (c) 2023. Colors indicate the number of months in each year for which an MHW was present at each OISSTv2.1 grid cell (0.25° resolution). The deepest blues, surrounded by a gray contour, indicate regions that experienced MHWs in only one month or not at all. MHWs were calculated using a 90% threshold of monthly sea-surface temperature anomalies relative to the 1991–2020 climatology from OISSTv2.1.

During 2023, global MHW coverage progressively increased through boreal winter, spring, and summer, reaching a peak coverage of ~40% of the global ocean area in August and remaining elevated through the end of the year (https://psl.noaa.gov/marine_heatwaves/#report). This increased prevalence of MHWs coincided with the development of a strong El Niño, a well-known driver of MHWs particularly in the eastern Pacific and Indian Oceans (Holbrook et al. 2019). However, relative to 1997 and 2015, two other years featuring the onset of strong El Niños, 2023 still stands out as exceptional for the widespread nature of MHWs (Fig. SB3.1). Throughout the year MHWs were persistent not only in hotspots typically associated with El Niño events, but also other areas including much of the Atlantic and western Pacific Oceans, which saw relatively little MHW activity in 1997 and 2015.

Marine heatwaves were not only widespread and persistent in 2023, but in many regions, they exhibited temperatures that were unprecedented in the observational record (section 3b). To contextualize MHW intensity in 2023 relative to 40+ years of observed ocean temperature anomalies, we compare the highest MHW intensity (i.e., warmest monthly SSTA) reached in 2023 to SSTAs from all prior months in the OISSTv2.1 observational period (1982–2023; 504 months total). Over portions of every major ocean basin as well as many inland seas—a total of 13% of the global ocean area—the highest monthly SSTA in at least the last 40 years (bright yellow areas in Fig. SB3.2) occurred in 2023. Similarly, 50% of the ocean areas experienced one of their top 10 monthly SSTAs on record. For reference, across all prior years (1982–2022), on average 2% of the ocean set an all-time high for monthly SSTA each year, and only 14% recorded a top-10 highest monthly SSTA. The exceptional coverage and intensity of MHWs in 2023 are closely related; comparison of MHW persistence (Fig. SB3.1) and maximum intensity (Fig. SB3.2) illustrates that regions exposed to MHW conditions for longer also tended to be regions with exceptionally high peak MHW intensities. In terms of cumulative intensity (i.e., the product of intensity and duration), those regions were especially heavily impacted.

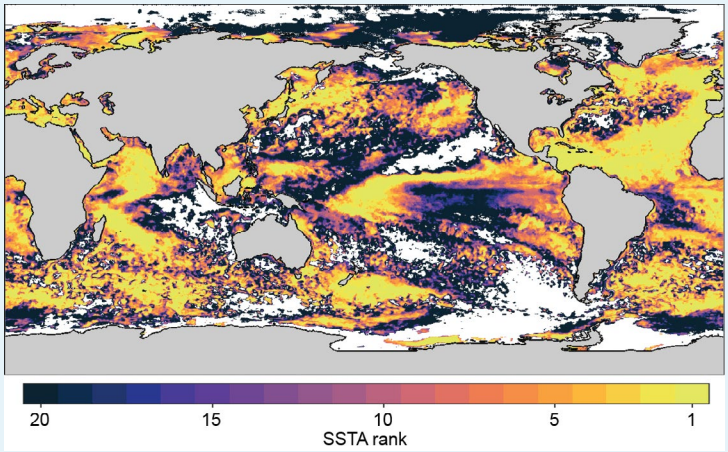

Fig. SB3.2. Intensity of 2023 marine heatwaves (MHWs) relative to historical conditions during the satellite record. Colors indicate the rank of 2023's highest monthly sea-surface temperature anomalies (SSTAs) relative to SSTAs for all months from 1982 to 2023 (N=504). SSTAs were calculated relative to the 1991–2020 climatology from OISSTv2.1. White areas did not experience any MHWs in 2023 based on monthly SSTAs.

c. Ocean heat content

—G. C. Johnson, J. M. Lyman, T. Boyer, L. Cheng, D. Giglio, J. Gilson, M. Ishii, R. E. Killick, M. Kuusela, R. Locarnini, A. Mishonov, M. Oe, S. G. Purkey, J. Reagan, K. Sato, and T. Sukianto

The oceans are central to the storage and transport of heat in Earth's climate system (IPCC 2021). They absorbed ~89% of the excess heat entering Earth's climate system from 1971 to 2020 (von Schuckmann et al. 2023). Since this warming is greatest at the surface, it has increased the strength and duration of marine heatwaves (e.g., Oliver et al. 2021; Sidebar 3.1) and the stratification of the upper ocean (e.g., Li et al. 2020), with impacts on biogeochemical cycles, ocean circulation, and ecosystems. This warming is linked to increased energy to fuel tropical cyclones (e.g., Walsh et al. 2016), sea-level rise (section 3f), melting of sea ice, ice shelves, and marine terminating glaciers and ice sheets (IPCC 2021), and coral bleaching (e.g., Hughes et al. 2017). Here, we discuss ocean temperature and heat content anomalies for 2023 relative to 2022 as well as a 1993–2022 climatology. We focus primarily on the upper 2 km, where temperature profiles collected by the Argo array, which first reached sparse near-global coverage around 2005, have greatly improved ocean sampling and the ability to map subsurface ocean temperature fields.

Weekly maps of ocean heat content anomaly (OHCA) relative to a 1993–2022 baseline mean (Fig. 3.4) as well as temperature for 58 pressure layers from 0 dbar to 2000 dbar were generated using Random Forest regression following Lyman and Johnson (2023) with V2.1 improvements as described at https://www.pmel.noaa.gov/rfrom/. In situ ocean temperature profiles, including Argo data downloaded from an Argo Global Data Assembly Centre in January 2024 (http://doi.org/10.17882/42182#98916), were used for training data for these maps, and prediction variables included satellite sea-surface height and temperature, location, and time. Since these maps are deeper than the 0 m–700 m maps shown in earlier reports, anomaly, year-to-year difference, and trend values are generally slightly larger. In situ global estimates of OHCA for three depth layers (0 m–700 m, 700 m–2000 m, and 2000 m–6000 m) from five different research groups (Fig. 3.6) are also discussed.

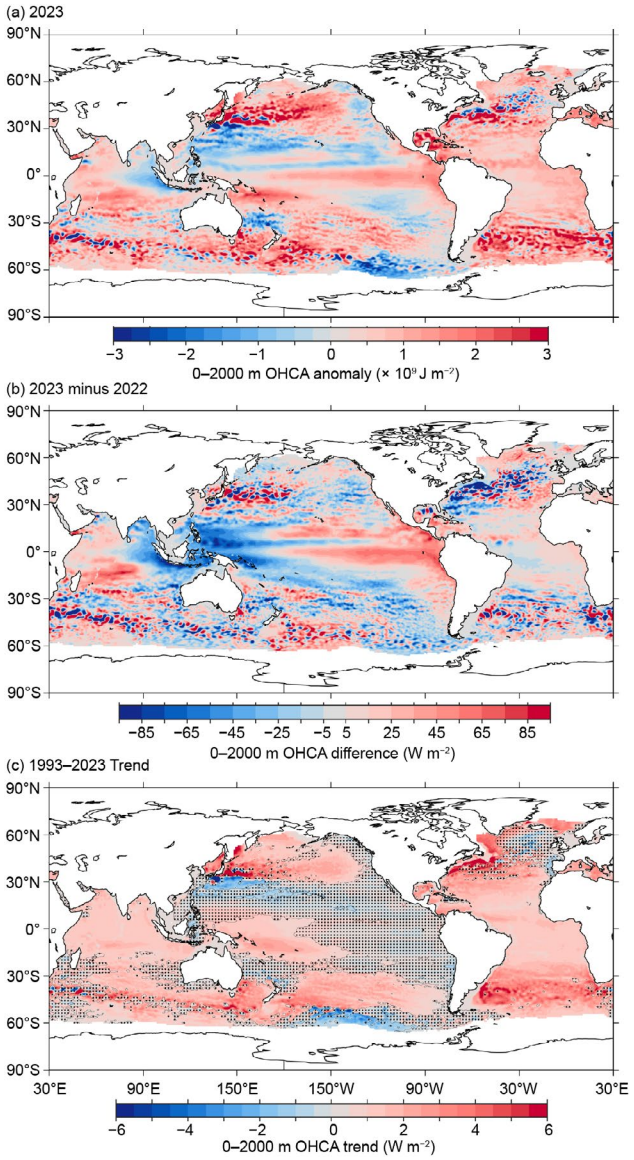

Fig. 3.4. (a) RFROM v2 estimate of 0-m–2000-m ocean heat content anomaly (OHCA; × 10^9 J m^{-2}) for 2023 analyzed following Lyman and Johnson (2023) with v2 improvements as in https://www.pmel.noaa.gov/rfrom/. In situ OHCA profiles are used as training data and satellite sea-surface height, satellite sea-surface temperatures, overlying layer properties, location, and time are predictors. Values are displayed relative to a 1993–2022 baseline. (b) 2023-minus-2022 combined estimates of OHCA expressed as a local surface heat flux equivalent (W m^{-2}). For (a) and (b) comparisons, note that 95 W m^{-2} applied over one year results in a 3 × 10^9 J m^{-2} change of OHCA. (c) Linear trend for 1993–2023 annual OHCA (W m^{-2}). Areas with statistically insignificant trends at 5%–95% confidence (taking into account the decorrelation time scale of the residuals when estimating effective degrees of freedom) are stippled.

After three consecutive years of La Niña conditions that persisted through January 2023, El Niño conditions were established by May 2023 and strengthened through the end of the year. Hence, the 2023-minus-2022 difference of 0-m–2000-m OHCA (Fig. 3.4b) shows a decrease in the west and an increase in the east in the tropical Pacific. Ocean heat content anomalies for 2023 (Fig. 3.4a) were positive all across the equatorial Pacific but stronger in the east, partly because anomalously near-surface eastward currents on the

equator (see Fig. 3.18a) driven by relaxation of the easterly trade winds (see Fig. 3.13a) carried warm water from the west to the east. Low values in 2023-minus-2022 differences are found close to the coast of the Americas at higher latitudes and farther west at lower latitudes, likely owing to a Rossby Wave signature of the La Niñas propagating from the eastern boundary westward. Differences around the western boundary current extensions exhibit energetic mesoscale features and are generally positive in 2023 relative to 2022. As in 2022, the centers of the North and South Pacific continued to be anomalously warm in 2023, with colder conditions around the edges, consistent with a continued negative Pacific Decadal Oscillation index in the Northern Hemisphere (section 3b). Again, the cold anomalies just south of the Kuroshio Extension and warm anomalies within that current that persisted in 2023 are associated with a northward shift of that current (see Figs. 3.18a, 3.20). Also again, Pacific marginal seas all remained warmer than climatological means in 2023.

In the tropical Indian Ocean, the 2023-minus-2022 difference of OHCA (Fig. 3.4b) decreased in the east and increased in the west, consistent with a transition from a negative to a positive phase of the Indian Ocean dipole index in 2023, with relatively cold SST anomalies in the east and warm anomalies in the west. The 2023 OHCA (Fig. 3.4a) were negative in the east between Australia and Indonesia and generally positive elsewhere.

The 2023-minus-2022 difference of OHCA (Fig. 3.4b) in the Atlantic Ocean was weakly positive in most of the tropics and the northern North Atlantic, with warming in the Caribbean Sea. Warming in the Labrador and Irminger Seas is consistent with a relatively warm vintage of Upper North Atlantic Deep Water formed in 2023. Among the substantial midlatitude variability was a cooling on the north side of the Gulf Stream extension from 2022 to 2023, suggesting a southward shift in the axis of that current. Again, the broad pattern of upper OHCA in 2023 (Fig. 3.4a) is similar to that in 2022 and 2021, with much of the Atlantic Ocean exhibiting upper OHCA above the 1993–2022 average (Fig. 3.4a). One exception, as in recent years, is the cooler-than-average conditions southeast of Greenland.

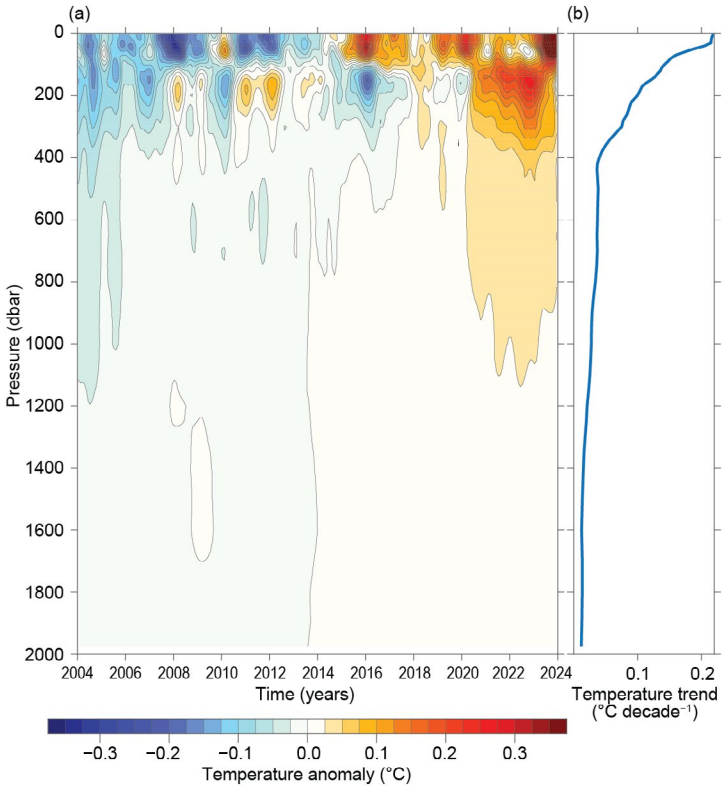

Fig. 3.5. (a) Near-global (66.5°S–81.5°N, but excluding seasonally ice-covered regions within that latitude range) average monthly ocean temperature anomalies (°C; from RFROM v2, Lyman and Johnson [2023]) relative to 2004–23 average monthly values, smoothed with a five-month Hanning filter and contoured at 0.025°C intervals (see color bar) vs. pressure and time. (b) Linear trend of temperature anomalies over time for 2004–23 in (a) plotted vs. pressure in °C decade^{-1} (blue line).

As expected, the large-scale statistically significant regional patterns in the 1993–2023 local linear trends of 0-m–2000-m OHCA (Fig. 3.4c) are similar to those for 0 m–700 m for 1993–2022 (Johnson et al. 2022) and earlier reports. However, since those earlier figures are for 0 m–700 m, and those of this year's report are for 0 m–2000 m, the amplitudes this year are higher, especially in the western boundary current extensions and Antarctic Circumpolar Current, where variability extends deep. A long-term warming trend in the Labrador Sea is also apparent in the deeper analysis, and the warming trend in the Greenland Sea is considerably stronger with the deeper maps. These are both locations of deep wintertime convection that has generally weakened and shoaled since 1993, resulting in warming of deep waters (e.g., Yashayaev and Loder 2017; Lauvset et al. 2018). Also, since the new machine learning algorithm used for the first time this year is less noisy, there are more areas with statistically significant trends, neither just because the time series is longer by one year, nor just because the analysis extends deeper.

Near-global average seasonal temperature anomalies (Fig. 3.5a) since 2004 show a marked contrast between 2023 and the previous three years, with warm anomalies surface-intensifying

as El Niño strengthened, in contrast to the subsurface warm anomalies from 100 m to 400 m evident during La Niña conditions from 2020 to 2022. This pattern arises as relaxation of the tropical Pacific trade winds allows warm waters in the western equatorial Pacific to spread eastward. The thermocline in the east deepens as a result. In the west, as the thermocline shoals, cold waters replace the warmer waters there as a consequence. Other El Niño years (e.g., 2009/10, 2015/16, and 2018/19) show a similar pattern, with La Niña years (e.g., 2007/08, 2010/11, and 2011/12, as well as 2020/21, 2021/22, and 2022/23) having the opposite signature. A warming trend (Fig. 3.5b) is strongest near the surface but extends all the way to the 2000-dbar sampling limit of Core Argo floats.

Globally integrated annually averaged OHCA estimates from 0 m–700 m and 700 m–2000 m from multiple research groups are presented in Fig. 3.6. Year-round, near-global sampling in both of those layers commenced around 2005 from Argo, making estimates relatively certain after that date. However, deep expendable bathythermographs sampling to 700 m were deployed extensively over much of the globe (with the notable exception of the high southern latitudes) starting in the early 1990s (Lyman and Johnson 2014), hence the upper layer results may be fairly robust back to 1993. Results for the 700-m–2000-m layer, which is quite sparsely sampled prior to about 2005, should be interpreted with caution in earlier years.

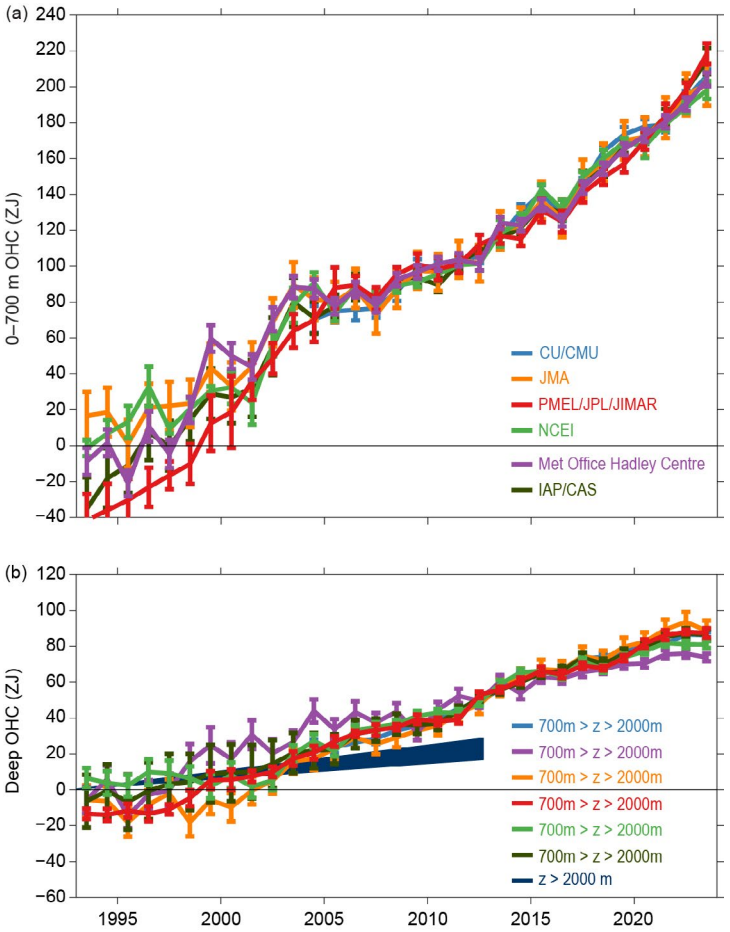

The various estimates of annual globally integrated 0-m–700-m OHCA (Fig. 3.6a) consistently show large increases since 1993, with all six analyses reporting 2023 as a record high. In contrast, 700-m–2000-m OHCA annual analyses (Fig. 3.6b) generally show negligible changes or small heat losses from 2022 to 2023, although a long-term warming trend is clear in this layer. The water column from 0 m to 700 m gained 13±5 ZJ and from 700 m to 2000 m lost 1.4±1.9 ZJ (means and standard deviations given) from 2022 to 2023. Causes of differences among estimates are discussed in Johnson et al. (2015), except for the new PMEL estimate, which differs considerably in methodology from the other estimates presented, as outlined in the second paragraph of this section.

The estimated linear rates of heat gain for each of the five global integral estimates of 0-m–700-m OHCA that extended from

Fig. 3.6. (a) Annual average global integrals of in situ estimates of upper (0-m–700-m) ocean heat content anomaly (OHCA; ZJ; 1 ZJ = 10^{21} J) for the period 1993–2022 with standard errors of the mean. The Meteorological Research Institute (MRI)/Japan Meteorological Agency (JMA) estimate is an update of Ishii et al. (2017). The Pacific Marine Environmental Laboratory (PMEL)/Jet Propulsion Laboratory (JPL)/Joint Institute for Marine and Atmospheric Research estimate is computed from RFROM v2 after Lyman and Johnson (2023). The Met Office Hadley Centre estimate is computed from gridded monthly temperature anomalies following Palmer et al. (2007) and Good et al. (2013). Both the PMEL and Met Office estimates use Cheng et al. (2014) eXpendable BathyThermograph (XBT) corrections and Gouretski and Cheng (2020) mechanical bathythermograph corrections. The NCEI estimate follows Levitus et al. (2012). The Institute of Atmospheric Physics (IAP)/Chinese Academy of Sciences (CAS) estimate was substantially revised from previous years as reported in Cheng et al. (2024). The CU/CMU estimate is detailed in Giglio et al. (2024). See Johnson et al. (2014) for details on uncertainties, methods, and datasets. For comparison, all estimates have been individually offset (vertically on the plot), first to their individual 2005–22 means (the best sampled time period) and then to their collective 1993 mean. (b) Annual average global integrals of in situ estimates of intermediate (700-m–2000-m) OHCA for 1993–2022 (ZJ) with standard errors of the mean and a long-term trend with one standard error uncertainty shown from September 1992 to July 2013 for deep and abyssal (z>2000 m) OHCA following Purkey and Johnson (2010) but updated using all repeat hydrographic section data available from https://cchdo.ucsd.edu/ as of Jan 2024.

1993 through 2023 (Fig. 3.6a) range from 0.39±0.05 W m^{-2} to 0.49±0.13 W m^{-2} applied over the surface area of Earth (Table 3.2) rather than the surface area of the ocean, to better compare to the top-of-the-atmosphere energy imbalance (e.g., Loeb et al. 2021; section 2f1). Linear trends from the 700-m–2000-m layer over the same time period range from 0.17±0.03 W m^{-2} to 0.24±0.04 W m^{-2}. Using repeat hydrographic section data collected from 1981 through 2023 to update the estimate of Purkey and Johnson (2010) for 2000 m–6000 m, the linear trend is 0.07±0.03 W m^{-2} from September 1992 to July 2013 (these dates are global average times of first and last sampling of the sections), consistent with previously reported decadal warming of Antarctic Bottom Water. Summing the three layers (despite their slightly different time periods as given above), the full-depth ocean heat gain rate applied to Earth's entire surface ranges from 0.65 W m^{-2} to 0.79 W m^{-2}.

Table 3.2. Trends of ocean heat content increase (in W m^{-2} applied over the 5.1 × 10^{14} m^2 surface area of Earth) from six different research groups over three depth ranges (see Fig. 3.6 for details). For the upper (0-m–700-m) and intermediate (700-m–2000-m) depth ranges, estimates cover 1993–2022, with 5%–95% uncertainties based on the residuals taking their temporal correlation into account when estimating degrees of freedom (Von Storch and Zwiers 1999). The 2000-m–6000-m depth range estimate, an update of Purkey and Johnson (2010), uses data from 1981 to 2022, having a global average start and end date of September 1992 to July 2013, again with 5%–95% uncertainty.

Research Group	0 m–700 m Global ocean heat content trends (W m^{-2})	700 m–2000 m Global ocean heat content trends (W m^{-2})	2000 m–6000 m Global ocean heat content trends (W m^{-2})
MRI/JMA	0.39±0.05	0.24±0.04	—
PMEL/JPL/JIMAR	0.49±0.13	0.23±0.01	—
NCEI	0.40±0.05	0.19±0.04	—
Met Office Hadley Centre	0.41±0.07	0.17±0.03	—
IAP/CAS	0.45±0.07	0.21±0.03	—
Purkey and Johnson	—	—	0.07±0.03

d. Salinity

—G. C. Johnson, J. Reagan, J. M. Lyman, T. Boyer, C. Schmid, and R. Locarnini

1. INTRODUCTION

The density of the ocean, crucial for its vertical stratification and interaction with the atmosphere, is determined by variations in ocean salinity and temperature. The thermal wind relation connects lateral density variations and vertical shear of ocean currents. In cold high latitudes, where temperature fluctuations are minimal, salinity variation mostly determines the vertical density structure. Various factors, including advection, precipitation and evaporation, river run-off, ice melt, and ice freezing (Ren et al. 2011; Yu 2011) contribute to salinity variations that impact crucial ocean–atmosphere exchanges of heat and dissolved gases, influencing phenomena like marine heatwaves, ocean carbon dioxide uptake, tropical cyclones, and deep or bottom water formation, as well as nutrient and oxygen exchange between the surface mixed layer and denser waters below.

The global average practical salinity stands at approximately 34.7, with surface values falling below 28.0 or exceeding 37.4 for only 1% of the ocean surface area each. Note that all salinity values used in this section are reported as observed, on the dimensionless Practical Salinity Scale-78 (PSS-78; Fofonoff and Lewis 1979). Generally, regions dominated by evaporation, such as the subtropics, exhibit higher salinity values, while areas where precipitation prevails, like the Intertropical Convergence Zone (ITCZ) and high latitudes, have fresher water (e.g., Wüst 1936; Schmitt 1995). Multi-decadal trends in ocean salinity have provided evidence for increases in the hydrological cycle over the ocean with global warming (Durack et al. 2012; Skliris et al. 2014, 2016). Springtime sea-surface salinity (SSS) values in the subtropical North Atlantic Ocean have exhibited skill in forecasting summer monsoon rainfall in the African Sahel (Li et al. 2016).

To investigate interannual changes of subsurface salinity, all available salinity profile data are quality controlled following Boyer et al. (2018) and then used to derive 1° monthly mean gridded salinity anomalies relative to a long-term monthly mean for the years 1955–2017 (Zweng et al. 2018) at standard depths from the surface to 2000 m. In recent years, the largest source of salinity profiles are the profiling floats of the Argo program (Riser et al. 2016). These data are a mix of real-time (preliminary) and delayed-mode (scientific quality-controlled) observations. Hence, the estimates presented here may be subject to instrument biases, such as a positive salinity drift identified in a subset of Argo Conductivity-Temperature-Depth, and will change after all data are subjected to scientific quality control. The SSS analysis relies on Argo data downloaded in January 2024, with annual anomaly maps relative to a seasonal climatology generated following Johnson and Lyman (2012) as well as monthly maps of bulk (as opposed to skin) SSS data from the Blended Analysis of Surface Salinity (BASS; Xie et al. 2014). BASS blends in situ SSS data with data from the *Aquarius* (Le Vine et al. 2014; mission ended in June 2015), Soil Moisture and Ocean Salinity (SMOS; Font et al. 2013), and the Soil Moisture Active Passive (SMAP; Fore et al. 2016) satellite missions. Despite the larger uncertainties of satellite data relative to Argo data, their higher spatial and temporal sampling allows higher spatial and temporal resolution maps than are possible using in situ data alone at present.

2. SEA-SURFACE SALINITY

—G. C. Johnson and J. M. Lyman

As noted in previous reports (e.g., Johnson et al. 2020), since salinity has no direct feedback to the atmosphere, unlike sea-surface temperature (SST) anomalies, which are often damped by heat exchange with the atmosphere, large-scale SSS anomalies can be quite persistent. In the tropical Pacific, both the ITCZ and the South Pacific Convergence Zone became saltier from 2022 to 2023 (Fig. 3.7b), with a slight freshening band just south of the ITCZ. The western equatorial Pacific became much fresher over that time period, although anomalies in the freshening region were of both signs in 2023 (Fig. 3.7a). There was also a large freshening in the climatologically fresh area west of Central America. As in 2022, in the North Pacific, the center of the basin was mostly anomalously salty in 2023, and the periphery was generally anomalously fresh. South of 30°S, the Pacific remained primarily salty in 2023, as it was in 2022, with a relatively fresh band to the north and northeast of New Zealand.

In the Atlantic, SSS freshened from 2022 to 2023 in the region of the ITCZ and the eastern equatorial area, as well off the coast of North America. The center of the subtropics in both hemispheres tended a bit saltier. The largest change was in the Caribbean Sea, which got much saltier from 2022 to 2023 (Fig. 3.7b), although its eastern portion remained anomalously fresh in 2023 compared to the long-term mean (Fig. 3.7a), as it was very anomalously fresh in 2022. The regions around the subtropical salinity maximum were anomalously salty in both the North and South Atlantic, as for many other recent years, including 2022, and the ITCZ was anomalously fresh.

The equatorial Indian Ocean freshened all the way across from 2022 to 2023, whereas south of about 8°S the basin mostly got saltier (Fig. 3.7b). These changes resulted in an anomalously fresh band across much of the Indian Ocean just north of the equator in 2023 (Fig. 3.7a), while south of the equator the ocean was mostly anomalously fresh about halfway across the basin west of Australia and mostly anomalously salty elsewhere.

Sea-surface salinity trends from 2005 to 2023 are mostly statistically insignificant, but there is statistically significant freshening around Hawaii and in the eastern third of the Pacific ITCZ, as well as in the Gulf of Alaska, the northeastern portion of the North Atlantic Ocean, and the Greenland, Iceland, and Norwegian Seas. With the exception of the area around Hawaii, these are all climatologically fresh areas. Salty trends are evident in portions of the subtropics in all the ocean basins, which are climatologically salty, as well as in the western Pacific sector of the Southern Ocean, which is not. This "salty gets saltier and fresh gets fresher" trend, which has been evident to varying degrees and discussed in *State of the Climate* reports since 2006, is expected on a warming Earth: As the atmosphere warms, it can hold more moisture, enabling an increased hydrological cycle over the ocean (Held and Soden 2006; Durack and Wijffels 2010).

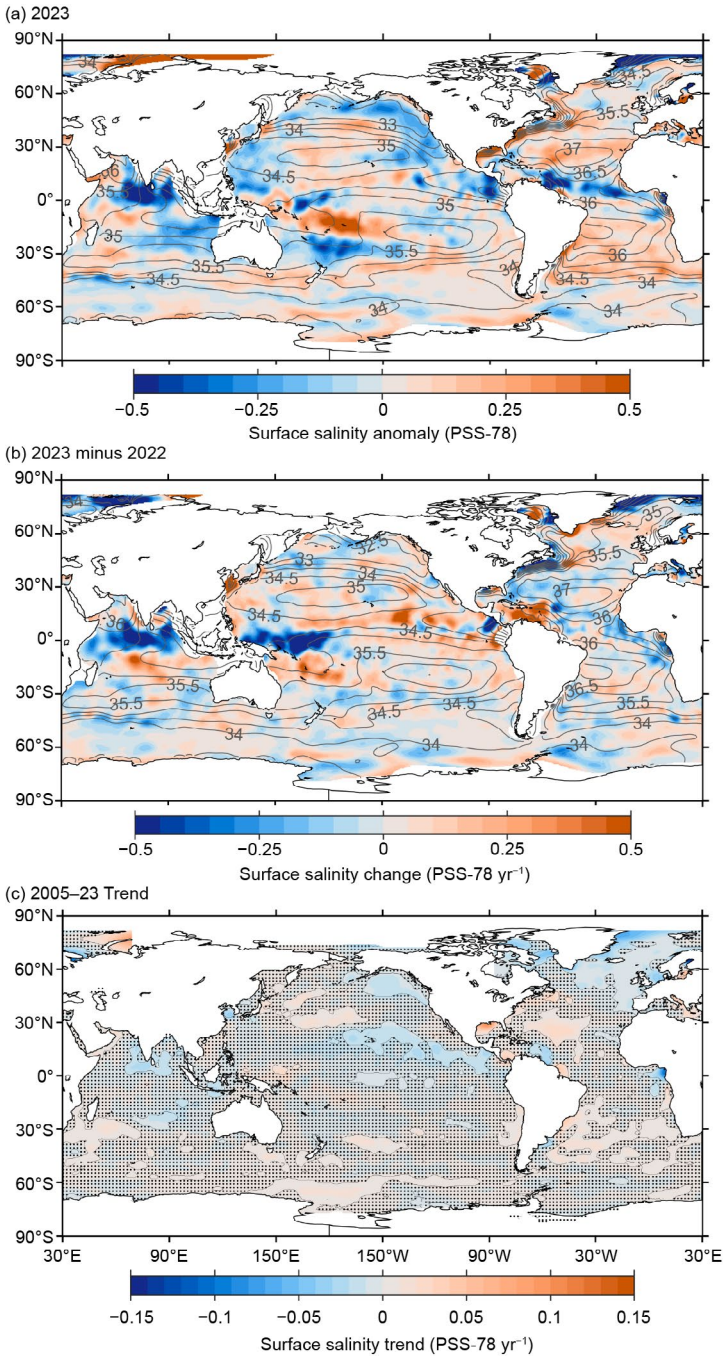

Fig. 3.7. (a) Map of the 2023 annual surface salinity anomaly (colors, PSS-78) with respect to monthly climatological 1955–2012 salinity fields from WOA13v2 (yearly average; gray contours at 0.5 intervals, PSS-78). (b) Difference of 2023 and 2022 surface salinity maps (colors, PSS-78 yr^{-1}). White ocean areas are too data-poor (retaining <80% of a large-scale signal) to map. (c) Map of local linear trends estimated from annual surface salinity anomalies for 2005–23 (colors, PSS-78 yr^{-1}). Areas with statistically insignificant trends at 5%–95% confidence (taking into account the decorrelation time scale of the residuals when estimating effective degrees of freedom) are stippled. All maps are made using Argo data.

In 2023, the seasonal BASS (Xie et al. 2014) SSS anomalies (Fig. 3.8) show the progressions of many of the features in the annual anomaly map using Argo data alone (Fig. 3.7a) and with higher spatial resolution, albeit with less accuracy. Fresh anomalies build in the far western equatorial Pacific while salty anomalies build in the Pacific ITCZ. The South Pacific Convergence Zone stays anomalously salty all year long, with the fresh band to the south of it diminishing slightly in amplitude over the course of the year. In the Atlantic, the build-up of a fresh anomaly in the ITCZ is apparent as the year

progresses. In September–November 2023, the fresh anomaly across much of the equatorial Indian Ocean becomes apparent, while over the course of the year in that basin the eastern fresh anomalies seen west of Australia diminish in amplitude.

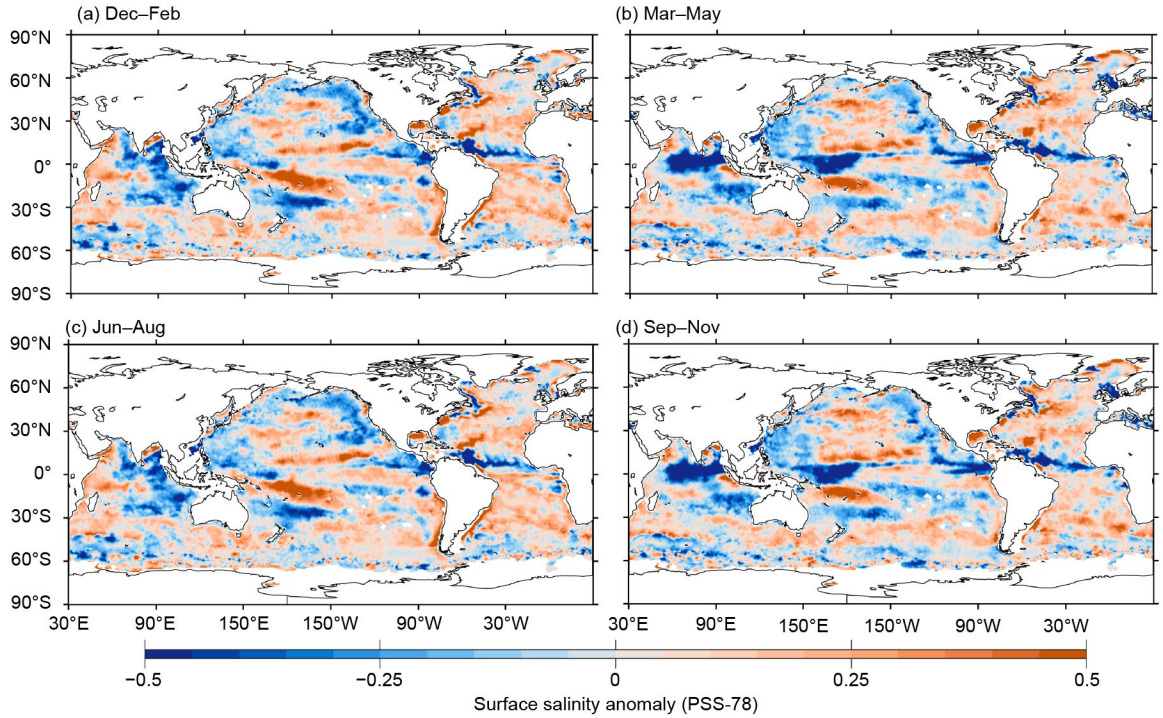

Fig. 3.8. Seasonal maps of sea-surface salinity (SSS) anomalies (colors) from monthly blended maps of satellite and in situ salinity data (BASS; Xie et al. 2014) relative to monthly climatological 1955–2012 salinity fields from WOA13v2 for (a) Dec 2022–Feb 2023, (b) Mar–May 2023, (c) Jun–Aug 2023, and (d) Sep–Nov 2023.

3. SUBSURFACE SALINITY

—J. Reagan, T. Boyer, C. Schmid, and R. Locarnini

Surface salinity enters the ocean interior primarily through two pathways (Talley 2002): subduction (downward movement along isopycnal [constant density] surfaces) and convection (deep vertical mixing). Salinity is a nearly conservative tracer, which allows the SSS footprint to be tracked through the interior ocean. Thus, SSS anomalies can propagate through the deep ocean, which can impact subsurface ocean dynamics through changes in density and is therefore an important seawater component to monitor.

The basin-average Atlantic salinity anomalies (Fig. 3.9a) for 2023 continue a pattern that has been evident since 2020 of persistent positive anomalies throughout the entire 0-m–1000-m water column, with the largest anomalies (>0.07) in the upper 100 m. From 2022 to 2023, the Atlantic became saltier from the surface down to 600 m (Fig. 3.9b), with the largest change occurring at ~30 m (change of ~+0.012 from 2022 to 2023). This contrasts with the freshening of ~−0.015 that occurred between 2021 and 2022 in the upper 50 m of the Atlantic (Reagan et al. 2023). Based on the zonal average salinity changes from 2022 to 2023 in the Atlantic (Fig. 3.9c), the salinity increase in Fig. 3.9b is primarily associated with basin-wide salinification at depth (>200 m) and localized increases in the upper 200 m centered at 40°S, 20°S, 15°N, and >60°N. The large (>0.09) near-surface increase near 15°N is due to the 2022 to 2023 salinity increase in the Caribbean Sea (Fig 3.7b) dominating the Atlantic zonal average in this area.

The 2023 basin-average Pacific salinity anomalies (Fig. 3.9d) are quite different than what was observed from 2018 through 2022 in the upper 300 m. In 2023, there is a transition of positive (~0.01) salinity anomalies to weak (<|−0.01|) fresh salinity anomalies in the 100-m–300-m layer and a transition of weak fresh anomalies (<|−0.01|) to salty anomalies (>0.01) in the upper 100 m throughout the year. This transition is apparent when looking at the 2022-to-2023 difference in basin-average Pacific salinity anomalies (Fig. 3.9e), where there is salinification in the upper 125 m (max of ~0.015 in the upper 50 m) and freshening between 150 m and 300 m (max of ~−0.015 at 200 m). The primary reason for the upper 125-m salinification can be seen in the

2022 to 2023 changes in zonal-average salinity (Fig. 3.9f), where there are zonal increases in near-surface salinity (>0.03) between 10°S and 25°S, and 10°N and 30°N that are subducted equatorward to ~150-m depth. The 2022 to 2023 freshening between 150 m and 300 m can be attributed to weak large-scale freshening (Fig. 3.9f).

The Indian basin-average salinity anomaly pattern that has prevailed since 2020 continued into 2023, but with some noticeable changes (Fig. 3.9g). The weak (<0.01) positive salinity anomalies that were prevalent in 2022 dissipated in 2023 over much of 0 m–1000 m, with a clear freshening trend throughout 2023 in the upper 50 m (>|−0.06| by the end of 2023). These changes manifest as an overall freshening between 2022 and 2023 (Fig. 3.9h) for nearly the entire 0-m–1000-m water column of the Indian basin, with the strongest freshening (~−0.025) in the upper 30 m. This overall freshening from 2022 to 2023 contrasts with what was seen between 2021 and 2022, where there was salinification (Reagan et al. 2023). The strong freshening near the surface is primarily associated with the freshening between 5°S and 10°N (Fig 3.7b) and is evident in the 2022-to-2023 zonally-averaged salinity changes for the Indian basin (Fig. 3.9i). In the upper 50 m just north of the equator, the zonally-averaged salinity change from 2022 to 2023 approaches ~−0.30. There are also large (> |−0.06|) zonally-averaged freshening changes between 2022 and 2023 of between 75 m–175 m and 10°S and 20°S.

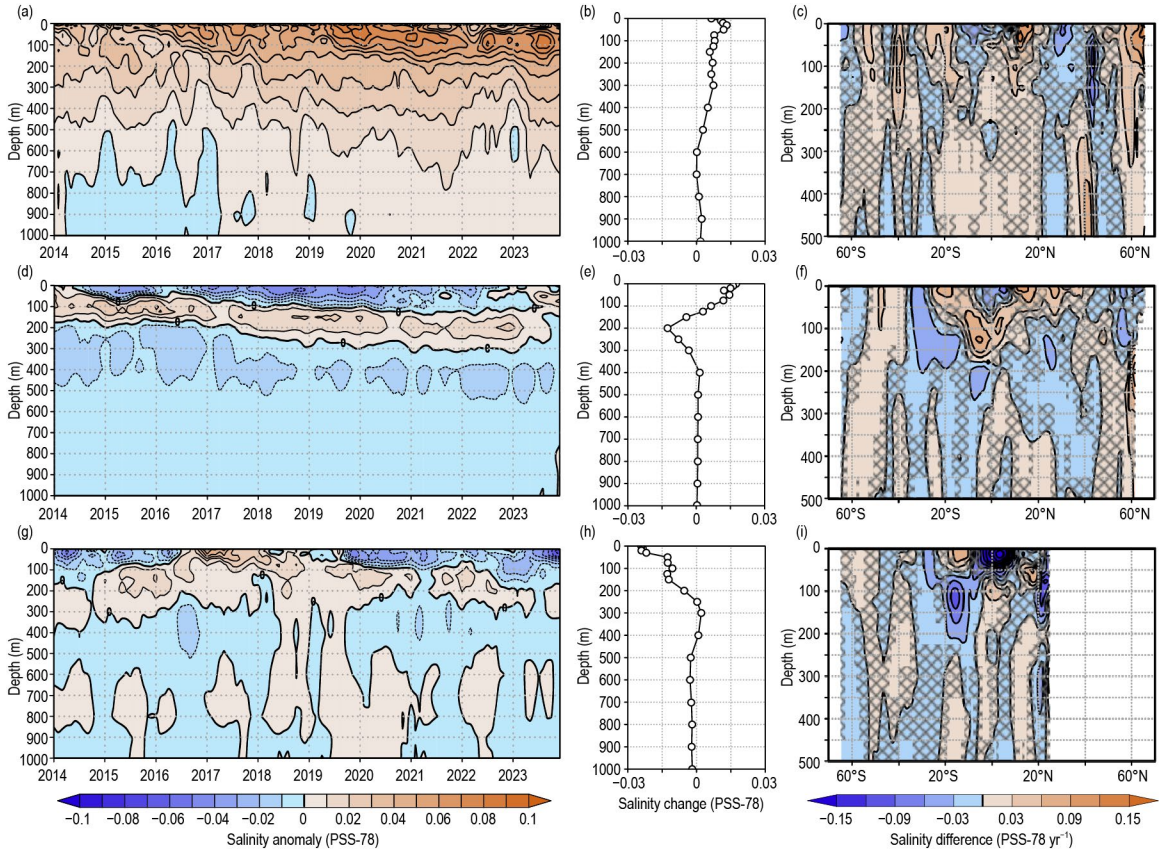

Fig. 3.9. Average monthly salinity anomalies from 0 m to 1000 m for the period 2014–23 for the (a) Atlantic, (d) Pacific, and (g) Indian basins. Change in salinity from 2022 to 2023 for the (b) Atlantic, (e) Pacific, and (h) Indian basins. Change in the 0-m–500-m zonal-average salinity from 2022 to 2023 in the (c) Atlantic, (f) Pacific, and (i) Indian basins with areas of statistically insignificant change, defined as <±1 std. dev. and calculated from all year-to-year changes between 2005 and 2023, stippled in dark gray. Data were smoothed using a three-month running mean. Anomalies are relative to the long-term (1955–2017) WOA18 monthly salinity climatology (Zweng et al. 2018).

The zonally-averaged salinity trends for 2005–23 for all three major ocean basins (Fig. 3.10) are similar in time and space to what was shown for the 2005–21 (Reagan et al. 2022) and 2005–22 (Reagan et al. 2023) time periods; thus, this discussion will focus on regions where the 2022-to-2023 salinity change (Fig. 3.9) has acted to strengthen or weaken these trends. The Atlantic 2022-to-2023 salinification north of 50°N (Fig. 3.9c) and between 0 m and 100 m acts to weaken the predominant freshening trend that has been observed since 2005 (Fig. 3.10a), whereas the 2022-to-2023 freshening between 25°N and 35°N in the upper 150 m has acted to weaken the

predominant salinification trend in this region. The Pacific freshening from 2022 to 2023 (Fig. 3.9f) between 20°S and 35°S in the upper 200 m has acted to weaken the longer-term salinification trend in this region (Fig. 3.10b). Finally, despite salinity decreasing from 2022 to 2023 by ~0.24 in the upper 50 m near the equator of the Indian basin (Fig. 3.9i), this region remains an area of insignificant salinity trends over the longer term (Fig. 3.10c) due to its large interannual variability. Overall, the significant salinity trends in all three major basins are reflective of the footprint of an amplifying hydrological cycle (Durack and Wijffels 2010; Durack et al. 2012; Skliris et al. 2014) where fresh regions are becoming fresher due to enhanced precipitation and salty regions are becoming saltier due to enhanced evaporation. These changes are then subducted into the interior ocean where they are evident in the trends shown in Fig. 3.10.

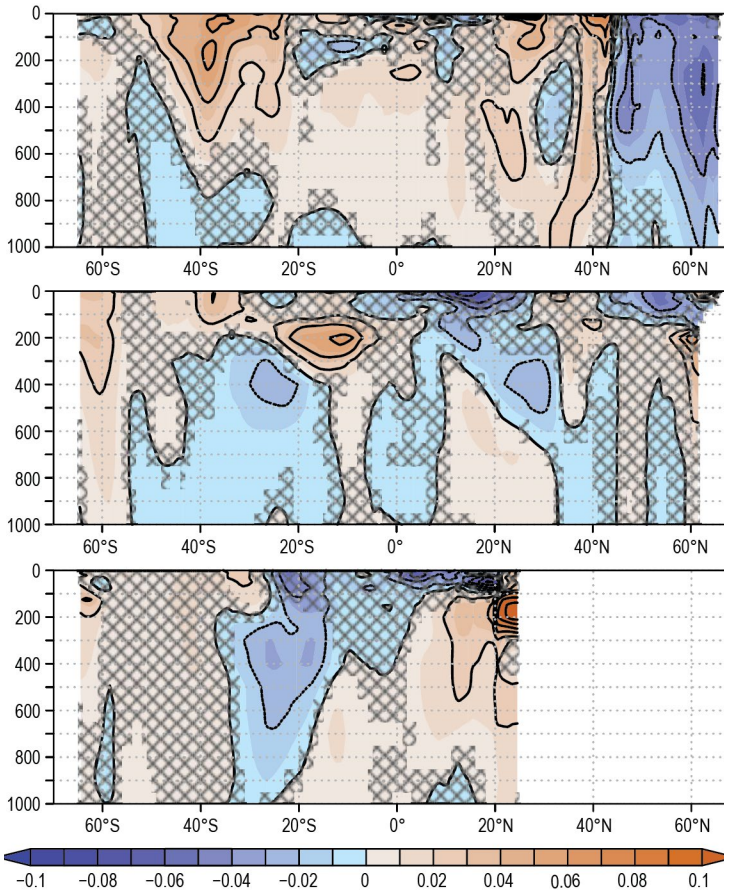

Fig. 3.10. Linear trend of zonally-averaged salinity from 2005 to 2023 over the upper 1000 m for the (a) Atlantic, (b) Pacific, and (c) Indian basins. The salinity trend is per decade and computed using least squares regression. Areas that are stippled in dark gray are not significant at the 95% confidence interval.

e. Global ocean heat, freshwater, and momentum fluxes

—L. Yu, C. Liu, P. W. Stackhouse, J. Garg, and R. A. Weller

The ocean and the atmosphere interact through the exchange of heat, freshwater, and momentum across their interface. These air–sea fluxes are key to maintaining the global climate system's equilibrium in response to incoming solar radiation. The ocean absorbs the majority of shortwave radiation reaching Earth's surface and redistributes this energy to the atmosphere through longwave radiation, evaporation (latent heat flux), and conduction (sensible heat flux). Any remaining heat is stored in the ocean and transported by the ocean's surface currents, predominantly driven by wind stress. Evaporation not only mediates heat but also moisture transfer, the latter of which, together with precipitation, determines the surface freshwater flux across the open ocean. Changes in these air–sea fluxes act as pivotal drivers for changes in ocean circulation, thereby affecting the global distribution of heat and salt from the tropics to the poles.

Here we examine the surface heat flux, freshwater flux, and wind stress in 2023 and their changes from 2022. The net surface heat flux (Q_{net}) comprises four components: net shortwave (SW), net longwave (LW), latent heat (LH), and sensible heat (SH). We calculate the net surface freshwater flux into the ocean, excluding inputs from rivers and glaciers, as the difference between precipitation (P) and evaporation (E), referred to as the $P–E$ flux. Data from multiple research groups are synthesized to produce global maps of Q_{net}, $P–E$, and wind stress (Figs. 3.11, 3.12, 3.13) and provide a long-term time series (Fig. 3.14).

The net SW and LW fluxes in 2022 and 2023 were sourced from the Fast Longwave and Shortwave Radiative Fluxes (FLASHFlux) version 4B product (Stackhouse et al. 2006), which have been radiometrically scaled to the surface SW and LW products from the Clouds and the Earth's Radiant Energy Systems (CERES) Surface Energy Balanced and Filled (EBAF) Edition 4.2

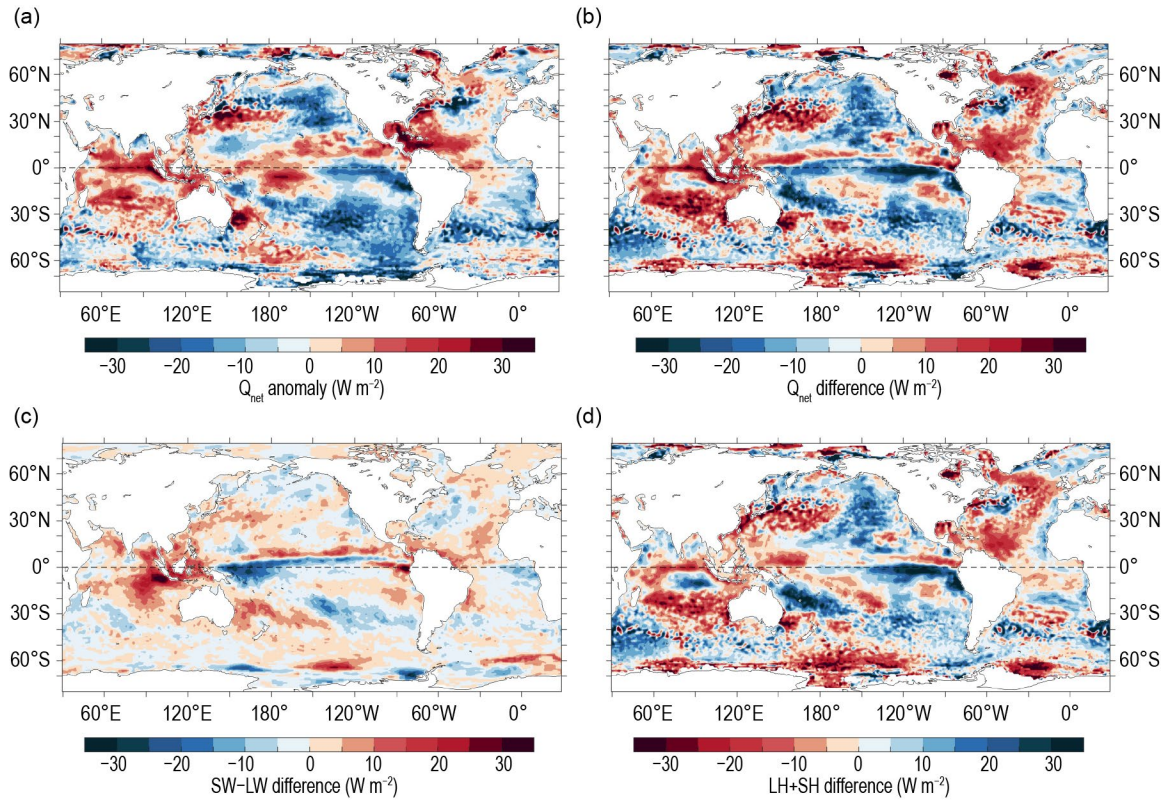

Fig. 3.11. (a) Surface heat flux (Q_{net}) anomalies (W m^{-2}) for 2023 relative to the 2001–15 climatology. Positive values denote ocean heat gain. (b) 2023-minus-2022 difference for (b) Q_{net}, (c) net surface radiation shortwave (SW) + longwave (LW), and (d) turbulent heat fluxes latent heat (LH) + sensitive heat (SH), respectively. Positive tendencies denote more ocean heat gain in 2023 than in 2022. LH+SH are from WHOI OAFlux2, and SW+LW is from the NASA FLASHFlux version 4B adjusted to CERES Surface EBAF Ed4.2. Net radiative fluxes defined as the difference between the incoming and outgoing radiation (positive indicates radiative flux into the ocean).

(Loeb et al. 2018; Kato et al. 2018). *P* was derived from the Global Precipitation Climatology Project (GPCP) version 2.3 products (Adler et al. 2018). Estimates for LH, SH, *E*, and wind stress were produced by the second generation of the Objectively Analyzed Air–Sea Heat Fluxes (OAFlux2; Yu and Weller 2007; Yu 2019), computed from satellite retrievals and the bulk parameterization Coupled Ocean Atmosphere Response Experiment (COARE) version 3.6 (Fairall et al. 2003). The Q_{net} time series begins in 2001, aligning with the availability of CERES EBAF 4.2 products, while the *P*–*E* and wind-stress time series extend back 36 years, starting in 1988.

1. SURFACE HEAT FLUXES

The 2023 Q_{net} anomaly pattern (Fig. 3.11a) highlights positive anomalies (indicating downward heat input and a warming effect on the ocean surface) in the western equatorial Pacific warm pool, the northwestern tropical Atlantic warm pool (including the Gulf of Mexico), and the tropical Indian Ocean. In contrast, negative Q_{net} anomalies (indicating upward heat release and a cooling effect on the ocean surface) are observed in the eastern equatorial Pacific cold tongue, as well as the northeastern and southeastern Pacific and the South Atlantic. This distinct east–west contrast in Q_{net} anomalies across the equatorial Pacific Ocean reflects the sea-surface temperature anomaly (SSTA) pattern (see Fig. 3.1a) associated with the shifting El Niño–Southern Oscillation (ENSO) conditions in 2023. The shift from a triple-dip La Niña early in the year to El Niño conditions by May resulted in substantial surface warming of over 1.5°C in the eastern equatorial Pacific. Concurrently, the Indian Ocean transitioned from a near-neutral condition to a positive Indian Ocean dipole (IOD) in boreal summer, leading to extensive warming in its western basin and moderate cooling in the eastern basin. Interestingly, the surface warming in the tropical Indian Ocean is positively correlated with Q_{net} anomalies, whereas the warming in the eastern equatorial Pacific shows a negative correlation with Q_{net} anomalies. The positive Q_{net} anomalies in the Indian Ocean suggest that the heat absorbed at the surface contributed to regional warming during the positive IOD phase. Conversely, the negative Q_{net} anomalies in the eastern equatorial Pacific cold tongue indicate that heat was released from the ocean to the atmosphere, tempering the surface warming induced by El Niño.

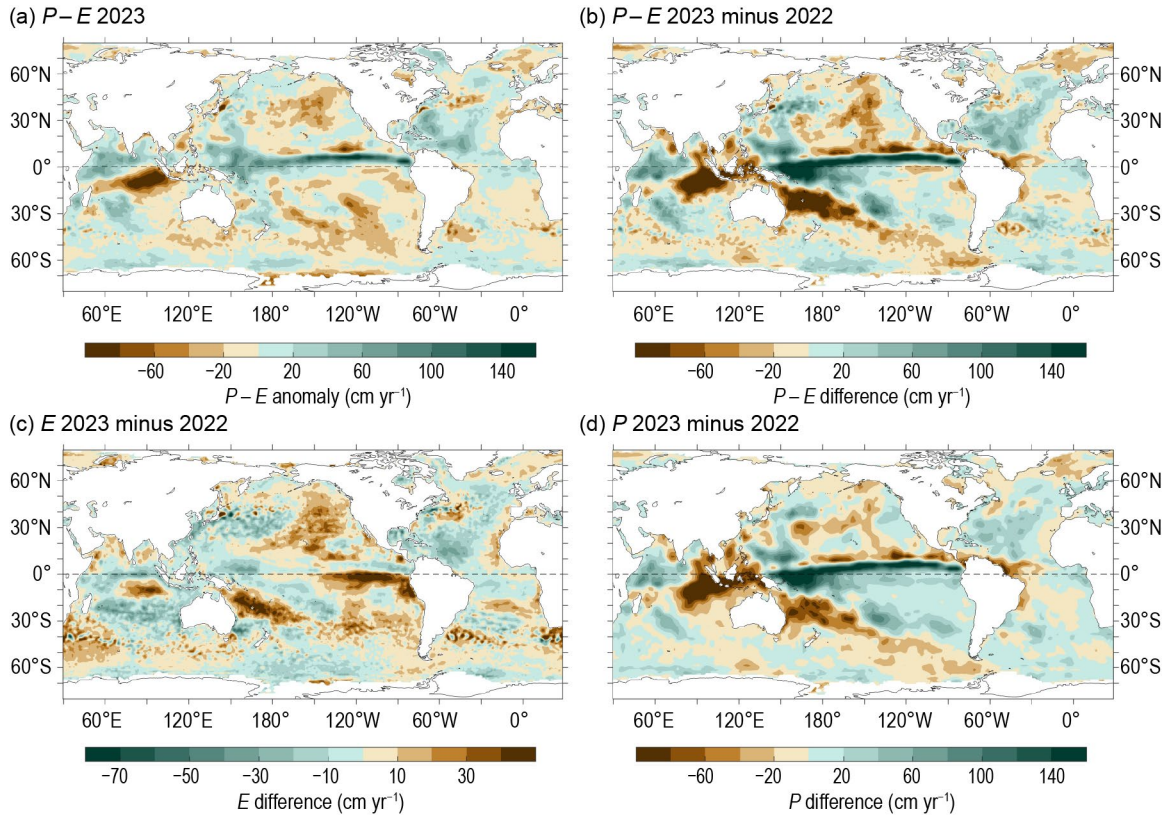

Fig. 3.12. (a) Surface freshwater precipitation (*P*) – evaporation (*E*) flux anomalies (cm yr^{-1}) for 2023 relative to the 1988–2015 climatology. Positive values denote ocean freshwater gain. 2023-minus-2022 differences for (b) *P*–*E*, (c) *E*, and (d) *P*. Positive (negative) values denote ocean freshwater gain (loss). *P* is the GPCP version 2.3 product, and *E* is from WHOI OAFlux2.

The 2023-minus-2022 Q_{net} difference pattern (Fig. 3.11b) deviates from the 2023 anomaly pattern in the tropical Pacific, largely due to the intricate impacts of ENSO on the four Q_{net} components. Net downward surface radiation (SW+LW; Fig. 3.11c) reduced along the Intertropical Convergence Zone (ITCZ) north of the equator and in the South Pacific Convergence Zone (SPCZ) in the western equatorial Pacific (indicated by blue shading). Meanwhile, upward surface turbulent heat flux (LH+SH; Fig. 3.11d) increased in the central and eastern equatorial Pacific (also highlighted by blue shading), driven by surface warming from El Niño. This combination led to predominantly net heat loss in the equatorial Pacific during 2023. In contrast, in the tropical Indian Ocean, the positive 2023-minus-2022 Q_{net} differences were attributed to increased downward surface radiation in the eastern basin, associated with reduced convection due to a positive IOD. Turbulent heat loss increased by about 15 W m^{-2} at the center of SW+LW positive anomalies but decreased by over 15 W m^{-2} across a broader area around the periphery, leading to a marked net heat gain in the Indian Ocean from 2022 to 2023. Comparatively, the Q_{net} changes in the tropical Pacific were moderate, with predominantly weak positive tendencies.

The extratropical North Pacific in 2023 was characterized by negative Q_{net} anomalies in the east, which encircled the positive anomalies extending along the Kuroshio Extension and its recirculation gyre between 20°N and 40°N. Interestingly, the North Atlantic displayed a reversed pattern: large positive Q_{net} anomalies across the basin surrounded negative anomalies near the Gulf Stream extension between 30°N and 50°N. These patterns of Q_{net} anomalies were primarily driven by surface turbulent heat fluxes in response to contrasting changes in surface winds across these two basins (Fig. 3.13b). Weaker winds in the broad North Atlantic reduced turbulent heat loss, resulting in increased Q_{net} (positive anomalies), while stronger winds in the eastern North Pacific intensified turbulent heat loss, leading to reduced Q_{net} (negative anomalies).

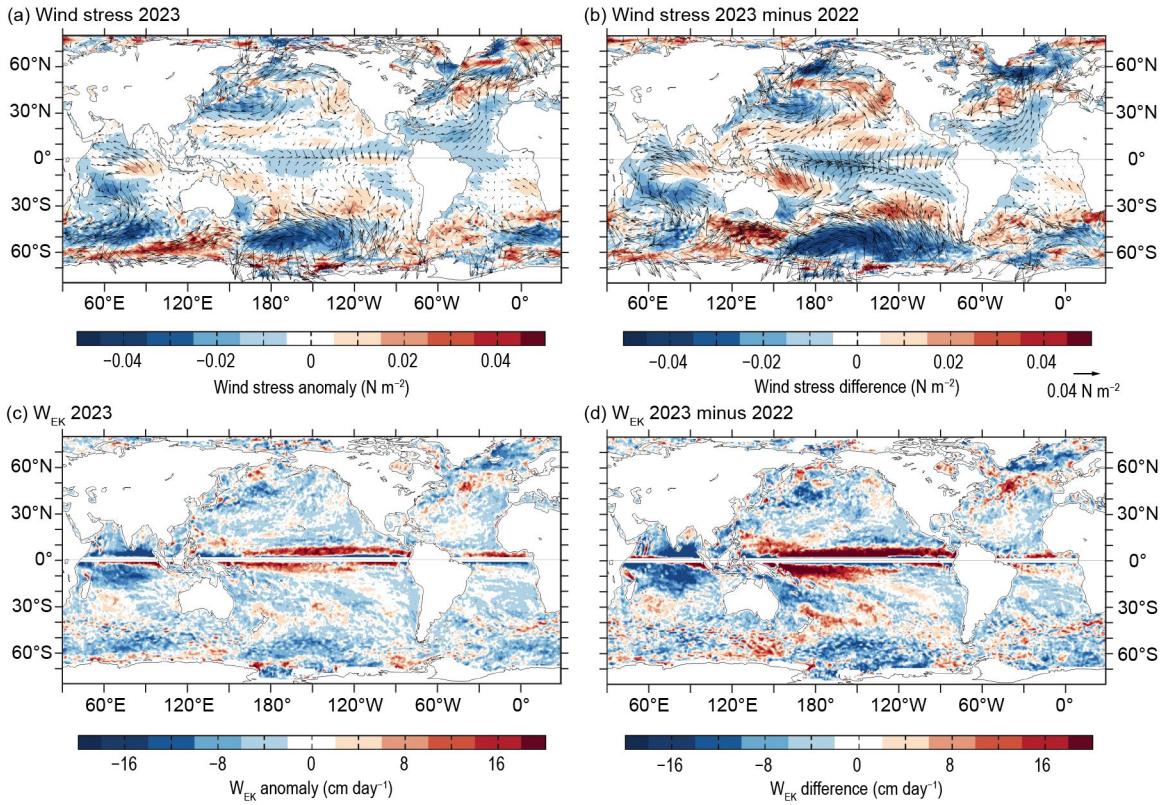

Fig. 3.13. (a) Wind stress magnitude (shaded) and vector anomalies (N m^{-2}) for 2023 relative to a 2001–22 climatology. (b) 2023-minus-2022 differences in wind stress. (c) Ekman vertical velocity (W_{EK}; cm day^{-1}) anomalies for 2023 relative to a 1988–2015 climatology. Positive (negative) values denote upwelling (downwelling). (d) 2023-minus-2022 differences of W_{EK}. Wind stress and W_{EK} fields are from WHOI OAFlux2.

In the North Atlantic, positive Q_{net} anomalies occurred at two locations: the Gulf of Mexico and the Sargasso Sea to its east (10°N–30°N) and the subpolar gyre including the Labrador and the Irminger Seas (40°N–65°N). Negative Q_{net} anomalies (net upward heat release; a cooling effect on the ocean surface) dominated the tropical Atlantic between 30°S and 30°N and also the subtropical North Pacific (5°N–20°N) and the eastern North Pacific (30°N–60°N). The magnitude of maximum positive and negative anomalies exceeded 20 W m^{-2} in some localized bands.

2. SURFACE FRESHWATER FLUXES

The 2023 *P*–*E* anomalies (Fig. 3.12a) show increased rainfall across the ITCZ and SPCZ of the tropical Pacific. This contrasts sharply with the substantial decrease in *P*–*E*, exceeding 30 cm yr^{-1}, in the southeastern equatorial Indian Ocean. These anomalies corresponded with SST changes, marking the transition weakly negative IOD index in the tropical Indian Ocean to a strongly positive one (IOD index of 0.596). This coincided with the ENSO phase transition, as shown in Figs. 3.2c,d. In the eastern Indian Ocean, cooler SSTAs suppressed rainfall, whereas warmer SSTAs in the western basin enhanced rainfall. The *P*–*E* modifications associated with the ENSO and IOD transitions are more readily seen in the 2023-minus-2022 difference pattern (Fig. 3.12b), which displays the anomalies with larger magnitudes because the change in phase between years is more marked than the 2023 difference from the long-term mean.

The 2023-minus-2022 differences in *E* reveal a marked increase (>20 cm yr^{-1}) in ocean evaporation across the Pacific Ocean, most notably in the eastern equatorial Pacific, along the southern periphery of the SPCZ in the southern Pacific and in the eastern regions of both the northern and southern Pacific. The 2023-minus-2022 differences in *P* (Fig. 3.12d) show that the drying condition was most acute in the southeastern tropical Indian Ocean, where rainfall reduced by over 80 cm within a year. Similar drying trends were observed in the southwestern Pacific along the southern periphery of the SPCZ. In the Atlantic Ocean, the most substantial change occurred in the North Atlantic, where a reduction in *E* and an increase in *P* amplified the net *P*–*E* by over 40 cm yr^{-1}. In other parts of the Atlantic, changes in *P*–*E* were comparatively mild.

3. WIND STRESS

In 2023, the equatorial Pacific was marked by predominantly negative wind stress anomalies, indicating a decrease in the strength of equatorial easterly winds associated with the transition to El Niño (Fig. 3.13a). The northeast trade winds slightly increased in the tropical North Pacific but weakened in the tropical North Atlantic. In mid- to high latitudes, wind anomalies exceeding 0.02 N m^{-2} occurred in the eastern Pacific and Atlantic. Over the Antarctic Circumpolar Current (ACC) region between 50°S and 60°S, the Southern Hemisphere westerlies exhibited a substantial weakening, especially in the Indo-Pacific sector where the largest anomalies fell below −0.04 N m^{-2}. Meanwhile, the midlatitude westerlies in both the North Pacific and North Atlantic also weakened, despite a marginal strengthening of their core near 50°N. The 2023-minus-2022 differences (Fig. 3.13b) emphasize the year's distinct anomaly pattern: a strengthening of trade winds in the tropical North Pacific and a weakening in the tropical South Pacific, coupled with a general decrease in westerlies across both hemispheres.

Wind patterns exhibit substantial spatial variability. These spatial variations in winds lead to divergence and convergence in Ekman transport, resulting in a vertical velocity known as Ekman pumping, characterized by downwelling (directed downward) and upwelling (directed upward) velocities, represented by W_{EK}, at the base of the Ekman layer. The computation of W_{EK} follows the equation: $W_{EK} = 1/\rho\nabla\times(\tau/f)$, where ρ is the density and *f* the Coriolis force. The 2023 W_{EK} anomalies showed distinct positive values in narrow equatorial bands of the Pacific and Atlantic Oceans and marked negative values in the equatorial Indian Ocean, each with magnitudes exceeding 16 cm day^{-1} (Fig. 3.13c). These patterns indicate a weakening of the regional climatological conditions, attributable to the resurgence of El Niño in the second half of the year. The 2023-minus-2022 W_{EK} differences (Fig.3.13d) display a similar spatial pattern but with greater intensities, highlighting the transition from La Niña in 2022 to El Niño in 2023. Outside of the equatorial zones, W_{EK} anomalies with substantial magnitudes were observed at higher latitudes, notably negative anomalies in the Pacific sector of the ACC regions. These anomalies correlate with a decrease in the strength of the Southern Hemisphere westerlies (Fig. 3.13b).

4. LONG-TERM PERSPECTIVE

A long-term perspective on the change in ocean-surface forcing functions in 2023 is presented within the framework of three-decade annual-mean time series of Q_{net}, *P*–*E*, and wind stress averaged across the global ice-free oceans (Figs. 3.14a–c). Anomalies in Q_{net} are referenced to the 2001–15 mean, where positive anomalies indicate increased net downward heat flux into the ocean, thereby contributing to ocean surface warming. The *P*–*E* and wind stress time series span 36 years, starting in 1988, and are referenced to the 1988–2015 mean. Positive anomalies in *P*–*E* denote increased freshwater flux into the ocean, leading to sea-surface freshening. Similarly, positive anomalies in wind stress denote increased magnitude of wind stress. The error bars in the time series represent one standard deviation of year-to-year variability.

Annual means of Q_{net}, *P*–*E*, and wind stress serve as indicators of the heat, freshwater, and momentum balance at the ocean surface. Q_{net} remained relatively stable from 2001 to 2010 but showed an upward trend between 2011 and 2016. During the later period, Q_{net} increased by approximately 3±1 W m^{-2}, from ~–1±1 W m^{-2} during the 2011 La Niña to a peak at ~2±1 W m^{-2} during the strong 2016 El Niño event. This increase in Q_{net} coincided with a 0.35°C increase in global-mean SST (see Fig. 3.3). Subsequently, Q_{net} decreased during the 2017/18 La Niña and continued its decline throughout the 2020–23 triple-dip La Niña. In 2023, Q_{net} was approximately 0.6±1 W m^{-2} lower than in 2022 but still higher than the 2001–10 average.

The *P*–*E* time series shows distinct decadal variability across the three decades. There was a notable downward trend in the 1990s, followed by a relatively stable period in the 2000s, and marked interannual fluctuations in the 2010s. Following its peak during 2015/16, *P*–*E* decreased by approximately 4±2 cm yr^{-1} to a low in 2019, remaining near this low throughout the 2020–23 La Niña. This reduction in *P*–*E* can be primarily attributed to increased evaporation in recent years, driven by higher SSTs (see Fig. 3.3). The 2023 *P*–*E* was slightly up by 0.8±2 cm yr^{-1} compared to 2022.

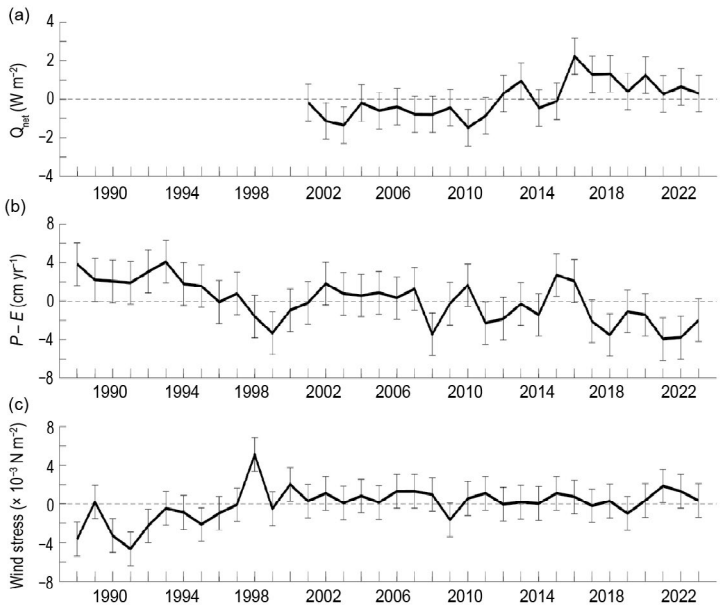

Fig. 3.14. Annual mean time series of global ocean-surface (a) net surface heat flux (Q_{net}; W m^{-2}) from a combination of CERES EBAF4.2 shortwave (SW) + longwave (LW) and WHOI OAFlux2 latent heat (LH) + sensitive heat (SH). The 2023 Q_{net} is based on FLASHFlux SW+LW as adjusted to EBAF and OAFlux2 LH+SH. (b) Net freshwater flux anomaly (*P*–*E*; cm yr^{-1}) from a combination of GPCP *P* and OAFlux2 *E*. (c) Wind stress magnitude anomalies (N m^{-2}) from WHOI OAFlux2. Error bars denote one standard deviation of annual-mean variability.

The wind stress time series features a generally stable value over the past two decades, following a substantial regime shift around 1999. The 1990s were characterized by a marked intensification of wind stress. From 2000 onward, the values have been relatively consistent, despite minor interannual fluctuations. There was a slight reduction in wind stress in 2009 and a minor increase in 2021. In 2023, wind stress levels showed a marginal decrease compared to the prior year.

f. Sea level variability and change

—P. R. Thompson, M. J. Widlansky, E. Leuliette, D. P. Chambers, B. Beckley, W. Sweet, B. D. Hamlington, S. Jevrejeva, M. A. Merrifield, G. T. Mitchum, and R. S. Nerem

Annual average global mean sea level (GMSL) from satellite altimetry (1993–present; Beckley et al. 2021) reached a new high in 2023, rising to 101.4 mm above 1993 (Fig. 3.15a). This marks the 12th consecutive year (and 28th out of the last 30) that GMSL increased relative to the previous year, continuing a multi-decadal trend of 3.2±0.4 mm yr^{-1} and acceleration of 0.075±0.025 mm yr^{-2} in GMSL during the satellite altimetry era (Fig. 3.15a). A quadratic fit with corrections for the eruption of Mount Pinatubo (Fasullo et al. 2016) yields a climate-driven trend of 3.1±0.4 mm yr^{-1} and acceleration of 0.092±0.025 mm yr^{-2} (updated from Nerem et al. 2018).

In addition to long-term change, record-high GMSL during 2023 reflects the onset of a strong El Niño event during May 2023 (see section 4b for details), which caused GMSL to increase sharply due to the impact of the El Niño–Southern Oscillation on precipitation patterns and ocean heat content (Nerem et al. 1999; Hamlington et al. 2020). Annually averaged GMSL from satellite altimetry increased 8.1±1.5 mm from 2022 to 2023, which is the third largest year-over-year increase in the satellite record. During previous strong El Niño events in 1997/98 and 2015/16, GMSL anomalies about the trend peaked in September and October, respectively. The ongoing 2023/24 event will peak later, as GMSL during 2023 reached its maximum during December and could continue to increase into 2024.

Data from Argo profiling floats analyzed by Scripps Institution of Oceanography (SIO; Roemmich and Gilson 2009) show the 0-dbar–2000-dbar steric (i.e., density-related) contribution to GMSL change was 1.4±0.3 mm yr^{-1} during 2005–23 (Fig. 3.15a). Mass concentration anomalies from the Gravity Recovery and Climate Experiment (GRACE) and GRACE Follow-On (GRACE-FO) missions produced by the NASA Jet Propulsion Laboratory (JPL; Wiese et al. 2022) show the mass contribution to GMSL change was 2.1±0.3 mm yr^{-1} during 2005–23 (Fig. 3.15a). The trend in the sum of steric and mass contributions, 3.4±0.5 mm yr^{-1}, agrees within uncertainties with the GMSL trend of

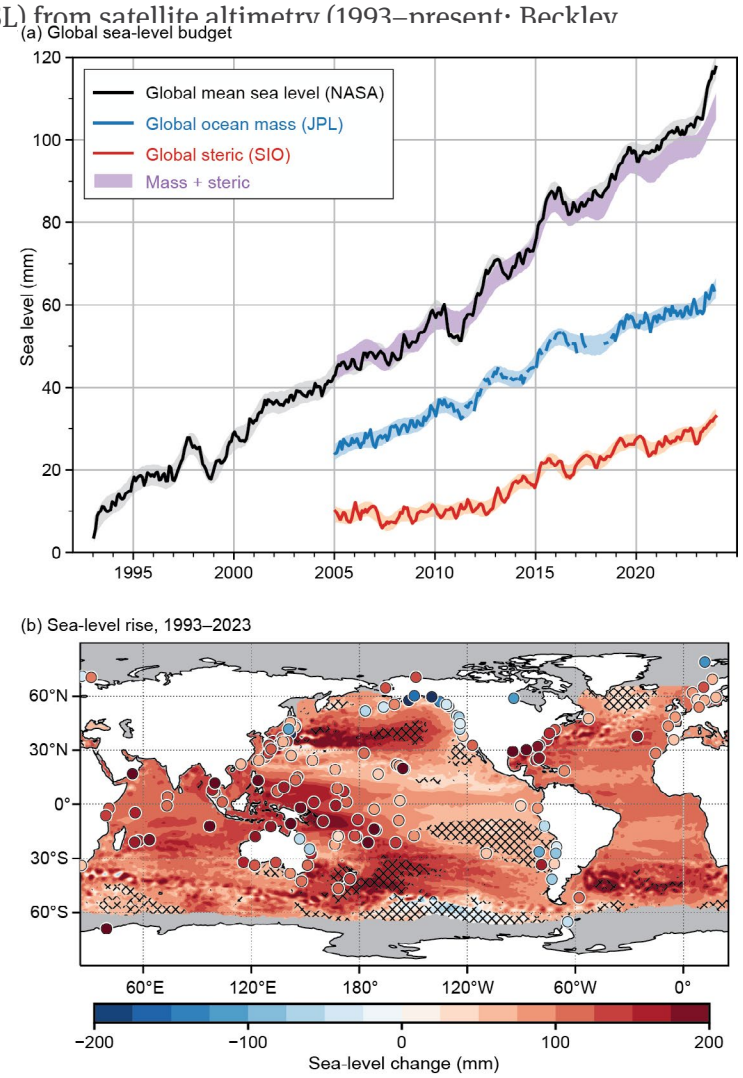

Fig. 3.15. (a) Global mean sea level (GMSL; mm) observed by satellite altimeters (1993–2023) produced with support from the NASA Sea Level Change and Ocean Surface Topography Science Teams (black). Monthly global ocean mass (2005–23) from GRACE and GRACE-FO calculated from mass concentrations produced by the NASA Jet Propulsion Laboratory (blue). GRACE and GRACE-FO data within 300 km of land were excluded in both ocean mass time series. Monthly global mean steric sea level (2005–23) from Scripps Institute of Oceanography (SIO) Argo data (red). Shading around the mass and steric series represents a 95% confidence range based on Gaussian process regressions, which are used to produce a 95% confidence range for the sum of global ocean mass plus steric (purple). (b) Total local sea-level change (mm) during 1993–2023 as measured by satellite altimetry (contours) and tide gauges (circles). Hatching indicates local changes that differ from the change in GMSL by more than one standard deviation. The trend map was generated using gridded delayed-mode and near-real-time altimetry data produced by the Copernicus Climate Change Service and obtained from the Copernicus Marine Service. Tide-gauge observations were obtained from the University of Hawaii Sea Level Center Fast Delivery database.

3.8±0.4 mm yr^{-1} measured by satellite altimetry since 2005 (Leuliette and Willis 2011; Chambers et al. 2017).

Consistency between the GMSL time series and the sum of independent estimates of steric and mass contributions (i.e., the "sea-level budget") is a significant achievement that increases confidence in estimates of Earth's global energy imbalance (e.g., Hakuba et al. 2021; Marti et al. 2022). However, misclosure in the budget emerged around 2016, which motivated several investigations into the origin of the discrepancy (e.g., Chen et al. 2020; Barnoud et al. 2021). Recent reprocessing and retracking of satellite altimetry data (including Topography Experiment [TOPEX]), radiometer recalibrations during the Jason-3 mission (Brown et al. 2023), and revision of the altimeter orbit standard have reduced misclosure in the budget relative to previous analyses (Fig. 3.15a). These updates to the altimeter record lowered the observed linear trend during the budget period, 2005–23, by approximately 0.2 mm yr^{-1} (Beckley et al. 2023). Over the complete altimeter record, 1993–2023, the adjustments reduced the linear trend by approximately 0.2 mm yr^{-1} and decreased the acceleration by nearly 0.016 mm yr^{-2} (Beckley et al. 2023). Remaining misclosure in the budget since 2016 may be related to uncertainties in the global ocean mass budget (Chen et al. 2020), additional error sources in the altimeter measurements (Barnoud et al. 2021), and/or steric changes below 2000 m not sampled by Argo.

Spatial structure in sea-level change (Fig. 3.15b) has become increasingly uniform as the altimetry record has grown in length, because the impact of natural fluctuations on regional sea-level trends decreases as the record length increases. Presently, only a small fraction of the global ocean has experienced sea-level trends that differ from the global mean trend by more than one standard deviation (hatched areas, Fig. 3.15b). However, sea-level changes relative to land (i.e., the quantity measured by tide gauges; circles, Fig. 3.15b), which is most relevant for societal impacts, can differ substantially from satellite-derived changes in tectonically active regions (e.g., Japan) and areas strongly affected by glacial isostatic adjustment (e.g., Alaska; Fig. 3.15b).

Relative to the 1993–2022 altimetry baseline, annual sea-level anomalies during 2023 were positive nearly everywhere (Fig. 3.16a), which primarily reflects the increasingly uniform long-term trends in rising sea levels (Fig. 3.15b). The abrupt yearly change of sea levels in the tropical Indo-Pacific basin (Fig. 3.16b) reflects the onset of El Niño conditions, which ended three years of La Niña conditions, as well as a concurrent reversal of the Indian Ocean dipole

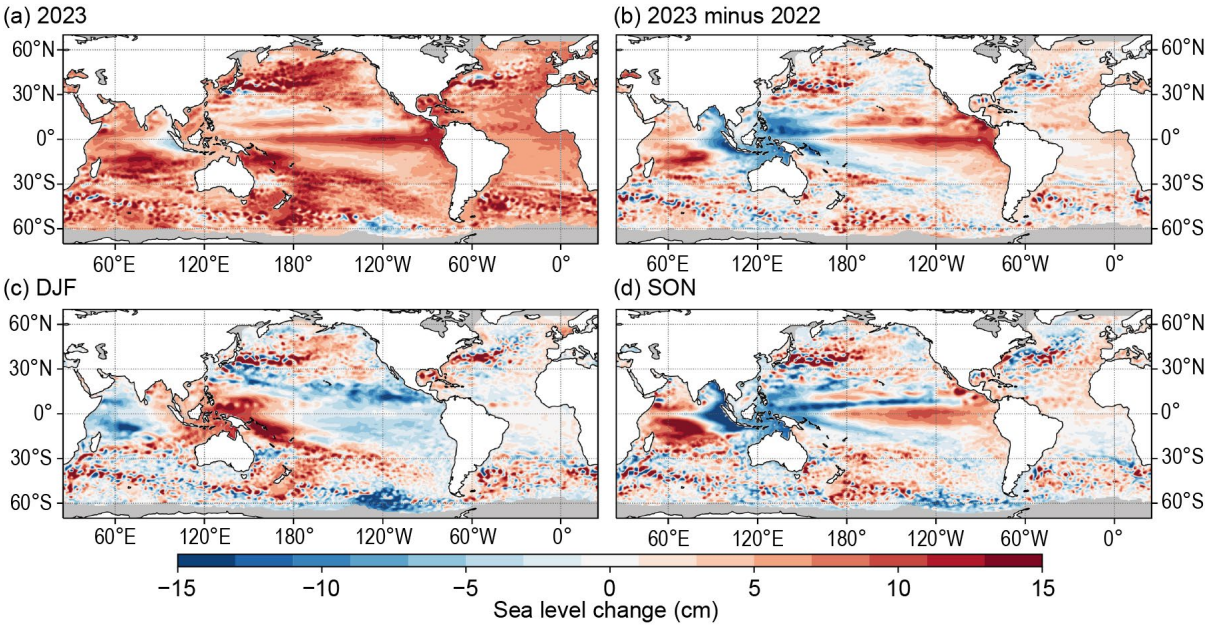

Fig. 3.16. (a) Annual average sea-level anomaly during 2023 relative to average sea level at each location during 1993–2022. (b) Average 2023-minus-2022 sea-level anomaly. (c) Average sea-level anomaly during DJF 2023 relative to the 1993–2022 DJF average. (d) Same as (c), but for SON. Units are given in cm. Global mean sea level was subtracted from panels (c),(d) to emphasize regional, non-secular change. These maps were generated using gridded delayed-mode and near-real-time altimetry data produced by the Copernicus Climate Change Service and obtained from the Copernicus Marine Service.

(IOD) from a weakly negative to positive phase. Compared to 2022, the two most noticeable sea-level changes were in the equatorial Pacific (falling and rising by up to 15 cm in the far western and eastern regions, respectively). Decreasing sea levels during 2023 compared to 2022 were also observed in the eastern Indian Ocean, both north and south of the equator, as well as throughout the Indonesian Throughflow region. Areas in the tropical south-central Indian Ocean and the tropical north-central Pacific also experienced notable year-over-year sea-level changes. The latter region, which includes Hawaii, is interesting because while the 2023 sea level compared to 2022 increased by 10 cm or more, the 2023 annual mean sea level was much closer to the long-term mean (i.e., locally, the year-to-year change only partly canceled the much lower sea levels of the preceding La Niña years). In the Atlantic, the 2023-minus-2022 differences were mostly either positive or nearly unchanged along all the continental coasts and throughout the basin interior (changes of generally 5 cm or less). In the midlatitudes as well as the Gulf of Mexico, year-to-year sea-level changes were larger in localized areas (positive and negative differences), which is common in such regions that are strongly affected by mesoscale oceanic eddies.

Development of El Niño combined with reversal of the IOD, both of which occurred during mid-2023, explains most of the inter-seasonal sea-level changes evident in the comparison of December–February (DJF) and September–November (SON) anomalies (Figs. 3.16c,d). In the Indian Ocean, the sea-level pattern clearly showed evidence of the Dipole Mode Index changing

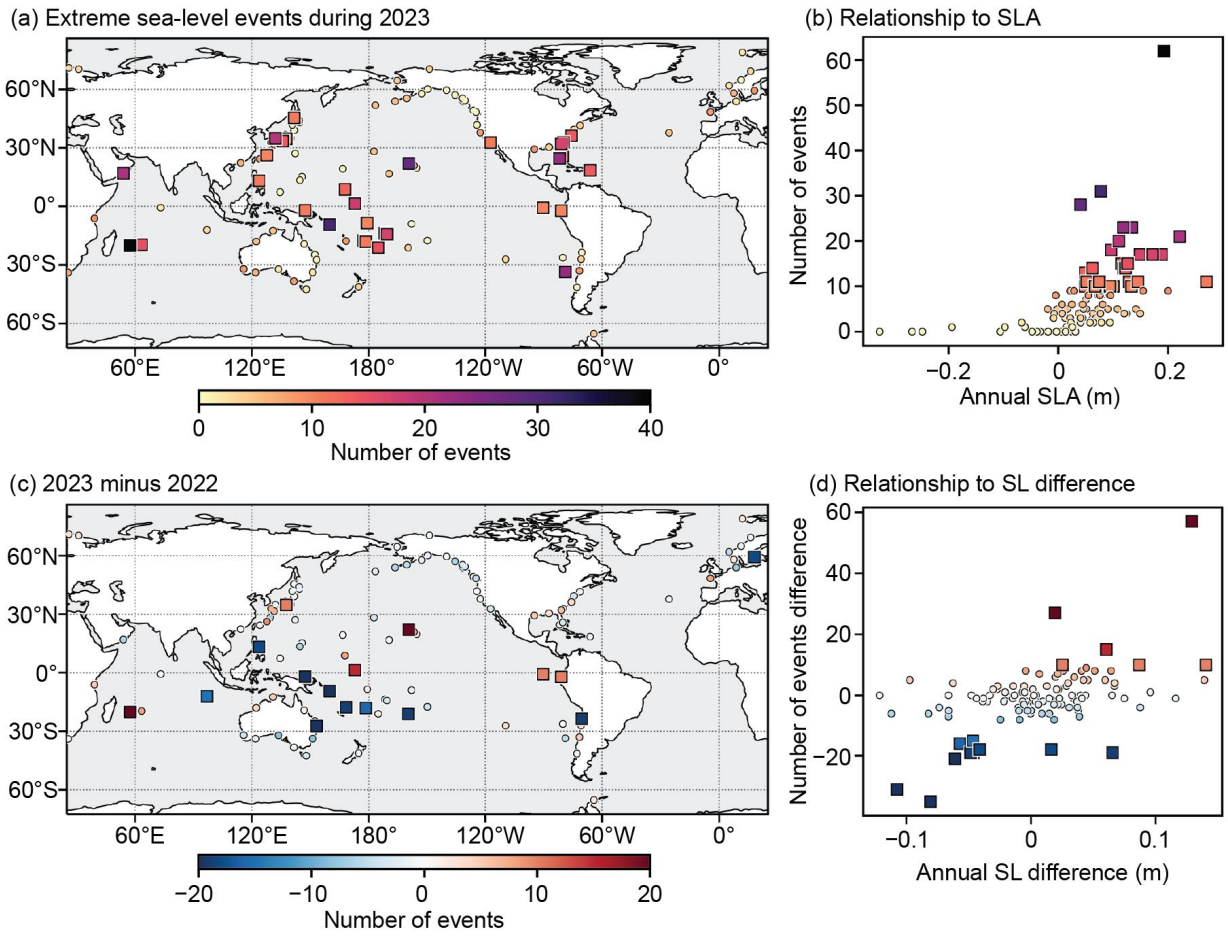

Fig. 3.17. (a) Number of extreme sea-level events from tide gauges during 2023. (b) Counts in (a) as a function of annual sea-level anomaly during 2023. Square markers in (a) and (b) highlight locations with more than 10 extreme events. (c) Change in the number of extreme sea-level events from 2022 to 2023. (d) Counts in (c) as a function of the change in annual sea level from 2022 to 2023. Square markers in (c) and (d) highlight locations where the magnitudes of changes in counts of extreme events were greater than 10. Counts of extreme sea-level events were calculated from hourly tide-gauge observations obtained from the University of Hawaii Sea Level Center Fast Delivery database. Only records with at least 80% completeness during 1993–2023 and 80% completeness during both 2022 and 2023, individually, were analyzed.

from weakly negative to positive during 2023 (i.e., sea-level anomalies increasing in the west and decreasing in the east; e.g., Fig. 8 in Kumar et al. 2020). Some of the highest regional sea-level anomalies during 2023 affected archipelagos in the Indian Ocean, such as Mauritius, Chagos, and the Seychelles, especially toward the end of the year. In the eastern Pacific, comparing DJF and SON, seasonal sea-level anomalies were also drastically different, especially around the Galapagos Islands and near the coasts of South and North America where 2023 ended with sea levels more than 15 cm above normal.

Ongoing trends, year-to-year variability, and seasonal changes in sea level impact coastal communities by increasing the magnitude and frequency of positive sea-level extremes that contribute to flooding and erosion. Minor impacts tend to emerge when local water levels exceed the 99th percentile of daily sea-level maxima (Sweet et al. 2014). Using 1993–2022 as the analysis epoch (consistent with the altimetry baseline), daily sea-level maxima that exceed the 99th percentile—hereafter referred to as extreme sea-level events—occurred more frequently in recent years compared to previous decades. Across 114 tide-gauge locations with sufficient data for analysis, the median number of extreme sea-level events per year and location increased from one during the 1993–97 pentad to four during the 2019–23 pentad. The 90th percentile of events per year and location increased from six during 1993–97 to 17 during 2019–23.

Thirty of the 114 locations experienced more than 10 extreme sea-level events during 2023, concentrated in the southwestern and equatorial Pacific Ocean, western boundary current regions in the Northern Hemisphere, and southern Indian Ocean (Fig. 3.17a) where annual sea-level anomalies were largest (Figs. 3.16a, 3.17b). The greatest number of events occurred in Mauritius (62), which experienced record-high monthly sea-level anomalies related to the strong positive IOD conditions during late 2023 (Fig. 3.16a). Large numbers of events also occurred in Kaua‘i, Hawai‘i (28), which were primarily related to local mesoscale variability rather than a basin-scale pattern of variability. Interestingly, the elevated numbers of extreme events in the southwestern Pacific during 2023 (Fig. 3.17a) also represent substantial year-over-year decreases from 2022 (Fig. 3.17b). Most of these events occurred early in 2023 prior to the development of El Niño and concurrent reduction of mean sea level in the region. The elevated numbers of events along the North Atlantic western boundary current system reflect a continuation of increased extreme sea levels from the previous year (Fig. 3.17c), which reflects warm ocean heat content anomalies (Fig. 3.4a) consistent with heat convergence in the subtropical gyre associated with the North Atlantic meridional overturning circulation (Volkov et al. 2023a) and weaker-than-average geostrophic currents (Fig. 3.22c).

g. Surface currents

—R. Lumpkin, F. Bringas, and R. C. Perez

This section describes variations of ocean surface currents, transports, and associated features, such as rings. Surface currents are obtained from in situ and satellite observations. Transports are derived from a combination of sea-surface height anomaly (from altimetry) and climatological hydrography. See Lumpkin et al. (2012) for details of these calculations. Zonal surface current anomalies are calculated with respect to a 1993–2022 climatology and are discussed below for individual ocean basins.

1. PACIFIC OCEAN

In 2023, zonal currents in the equatorial Pacific (Fig. 3.18a) exhibited annual mean eastward current anomalies exceeding 10 cm s^{-1} from 2°S to 4°N and between 160°E and 100°W, with the strongest anomalies of 23 cm s^{-1} at 160°E–170°W, associated with the May–December El Niño and weakened trade winds (Fig. 3.13a).

In 2020–23, the annual-average latitude of the Kuroshio Extension in the region 32°N–38°N, 141°E–153°E was shifted north of its long-term (1993–2023) location of 35.4°N, to a maximum of 36.8°N in 2021 and to 36.2°N in 2023 (Fig. 3.20b). This can be seen as alternating eastward/westward anomalies in

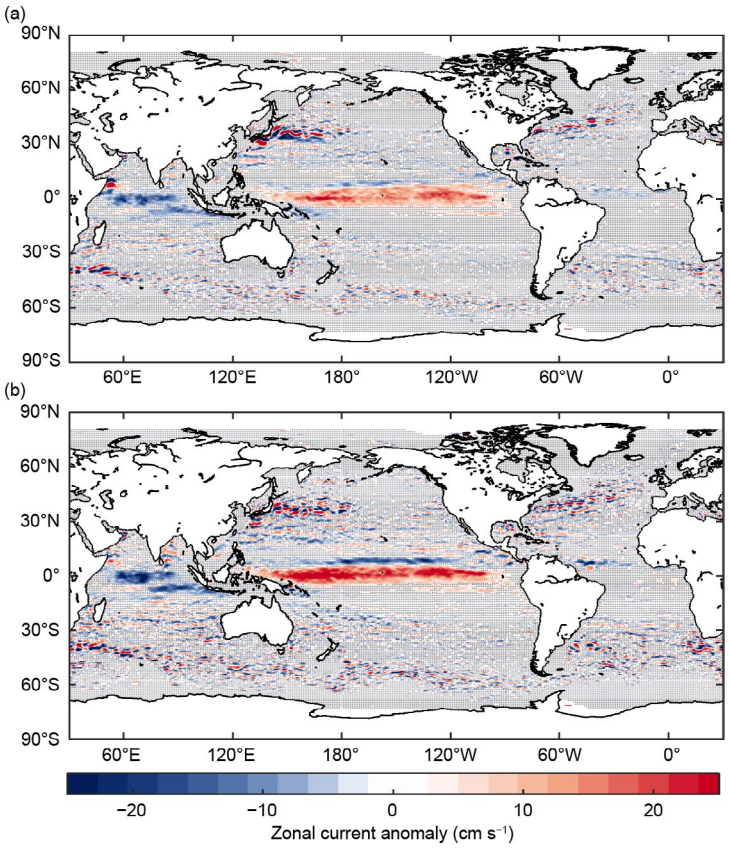

Fig. 3.18. Annually-averaged geostrophic zonal current anomalies with respect to the seasonal climatology (cm s^{-1}) for (a) 2023 and (b) 2023-minus-2022 anomalies, derived from a synthesis of drifters, altimetry, and winds. Values are only shown where they are significantly different from zero.

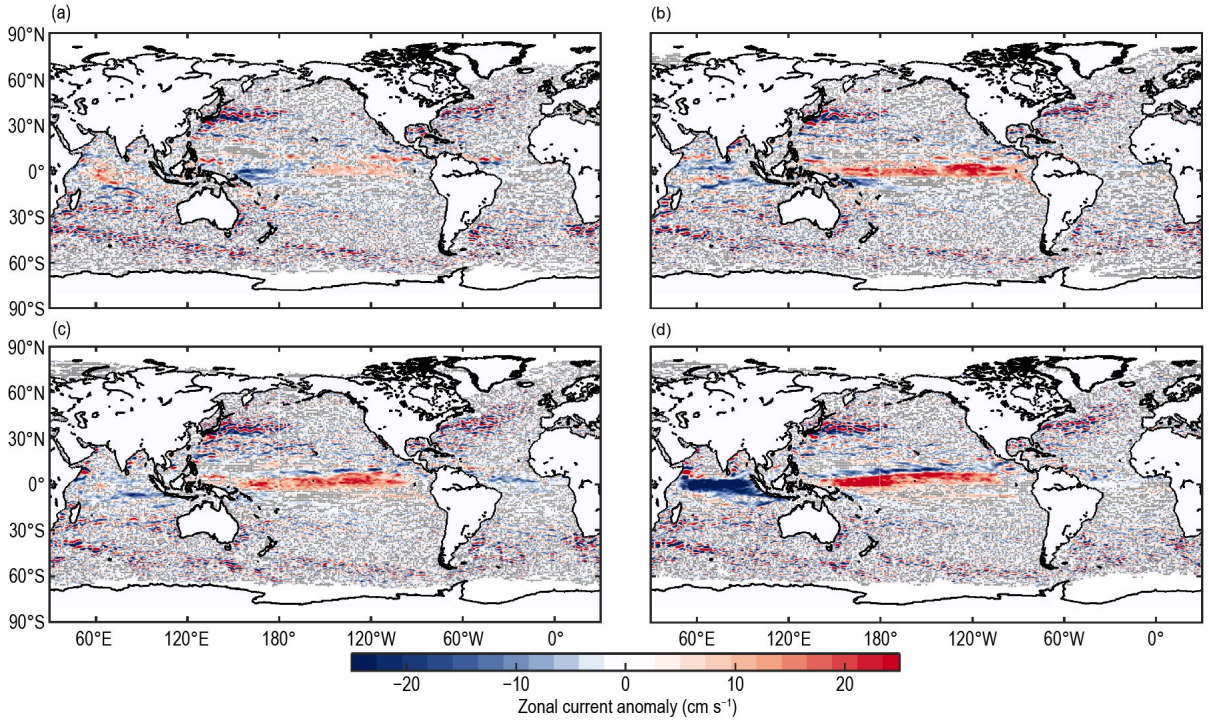

Fig. 3.19. Seasonally averaged zonal geostrophic anomalies with respect to seasonal climatology for (a) Dec 2022–Feb 2023, (b) Mar–May 2023, (c) Jun–Aug 2023, and (d) Sep–Nov 2023. Values are only shown where they are significantly different from zero.

Fig. 3.18a that persisted through the year (Fig. 3.19) and also in a band of increased ocean heat content anomalies (Fig. 3.4a). This large 2020–23 northward shift of the Kuroshio Extension (Fig. 3.20c) corresponded with an increase in averaged eddy kinetic energy (EKE; Fig 3.20d); this pattern is inconsistent with decadal shifts between increased/decreased EKE and a southward/northward shift of the Kuroshio Extension and arises due to a meander of the Kuroshio off the southern coast of Japan that has been present since 2017 (Qiu et al. 2020; Qiu and Chen 2021) and was still present in 2023 (Fig. 3.20b).

Because the equatorial eastward anomalies are a reversal of the La Niña-associated westward anomalies of 2022, the 2023-minus-2022 difference map (Fig. 3.18b) reaches eastward values exceeding 30 cm s^{-1} in the western equatorial Pacific. The lack of an intensified North Equatorial Countercurrent (NECC) in 2023, present in 2022, led to negative (westward) anomalies of 10 cm s^{-1}–15 cm s^{-1} in the difference map at 7°N–9°N across the central Pacific.

Equatorial zonal current anomalies were close to zero in December 2022–February 2023 (Fig. 3.19a), with weak (5 cm s^{-1}–10 cm s^{-1}) eastward anomalies at 3°S–3°N in the central and eastern basin consistent with a weakening of the westward South Equatorial Current (SEC) but residual westward anomalies in the western basin creating a dipole pattern. By March–May 2023 (Fig. 3.19b) the situation had changed dramatically, with equatorial eastward anomalies reaching 20 cm s^{-1} across the basin. These anomalies persisted through June–August (Fig. 3.19c), exceeding 10 cm s^{-1} from 2°S to 4°N. By September–November (Fig. 3.19d), the strongest anomalies were observed in the western basin, peaking at 40 cm s^{-1} between 0° and 1°N averaged in the longitude band 150°E–165°W and weakening anomalies in the central and eastern basin.

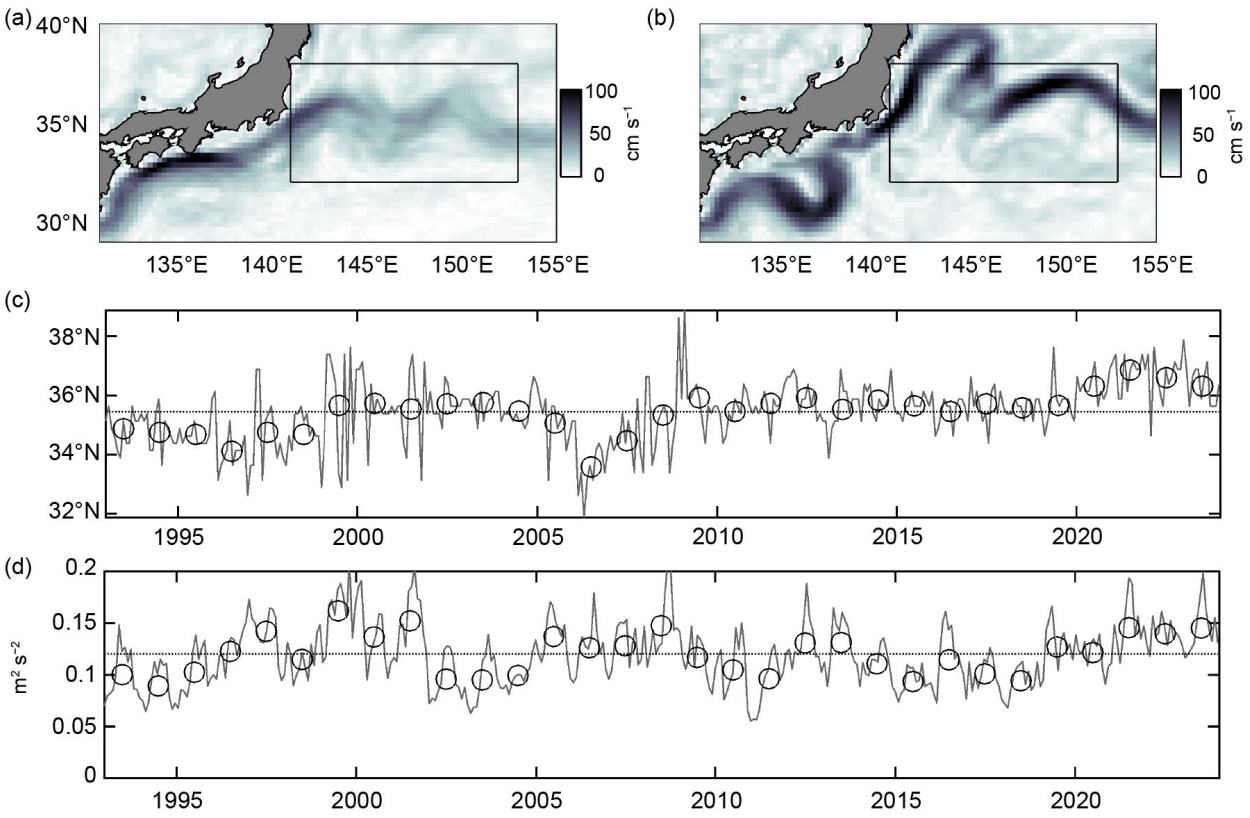

Fig. 3.20. (a) Climatological geostrophic surface current speed (cm s^{-1}) from Mulet et al. (2021) in the Kuroshio Current region (box) and surrounding regions. (b) 2023 mean geostrophic currents from MDT13 and Copernicus near-real-time altimetry. (c) Latitude of maximum zonal currents averaged in the Kuroshio Current region. (d) Mean eddy kinetic energy (m^2 s^{-2}) in the Kuroshio Current region.

2. INDIAN OCEAN

Annually-averaged zonal currents in the Indian Ocean (Fig. 3.18a) exhibited 5 cm s^{-1}–10 cm s^{-1} westward anomalies across the basin between 2°S and 3°N, with the strongest anomalies around 0°–1°N, driven by anomalously strong easterly wind anomalies (Fig. 3.13a). Because these current anomalies were much stronger than observed anomalies in 2022, the 2023-minus-2022 difference map (Fig. 3.18b) is similar to the 2023 anomaly map except near the western boundary offshore of Somalia. These anomalies were not present throughout much of the year (Fig. 3.19); they developed rapidly in September–November (Fig. 3.19d), when they exceeded 40 cm s^{-1} between the equator and 1°S.

As seen in 2022, relatively strong (15 cm s^{-1}–20 cm s^{-1}) negative/positive anomalies in the 2023 anomaly map (Fig. 3.18a) immediately offshore Somalia indicate a southward shift of the Somali Current extension (after leaving the coast and flowing eastward) and southern edge of the Great Whirl (Beal et al. 2013) compared to climatology. As in 2022, these alternating-sign anomalies developed in June–August 2023 (Fig. 3.19c) and strengthened to ±40 cm s^{-1} in September–November (Fig. 3.19d).

3. ATLANTIC OCEAN

Annual mean zonal current anomalies in the tropical Atlantic Ocean in 2023 did not exceed 4 cm s^{-1} (Fig. 3.18a). The 2023-minus-2022 difference map (Fig. 3.18b) is therefore dominated by the 2022 eastward anomalies of 10 cm s^{-1} at 7°N–8°N (Lumpkin et al. 2023). The year began (Fig. 3.19a) with ~10 cm s^{-1} eastward/westward anomalies north/south of 6°N in the western tropical Atlantic, indicating an acceleration and northward shift of the NECC. This pattern disappeared by March–May (Fig. 3.19b). In June–August (Fig. 3.19c), 5 cm s^{-1}–10 cm s^{-1} westward anomalies were present across the basin at 1°N–3.5°N, indicating a slight strengthening of the westward northern core of the SEC (see Lumpkin and Garzoli 2005). No significant zonal current anomalies were present in September–November (Fig. 3.19d).

The variability of key Atlantic Ocean currents is continuously monitored in near-real-time using a combination of in situ data and satellite altimetry (https://www.aoml.noaa.gov/phod/altimetry/cvar). In the southeastern Atlantic, the Agulhas Current shed six rings during 2023, a level of activity that, similar to the previous year, lies within the 1993–2022 average of four to six rings per year. At the same time, the annual transport was 50.9 Sv (1 Sv=10^6 m^3 s^{-1}) along a cross section at ~28°E and between 34°S and 40°S, only 0.1 Sv higher than the previous year, continuing the pattern of annual transports that have remained within 1 standard deviation of the long-term mean of 50.9±2.8 Sv since 2018. In the southwestern Atlantic, the Brazil Current transports waters of subtropical origin into subpolar regions. During 2023, the Brazil-Malvinas Confluence was located at 37.9°S, a southward shift of 0.5°S compared to 2022 and compatible with the long term mean of 37.8±0.6°S (see https://www.aoml.noaa.gov/phod/altimetry/cvar/mal/BM_ts.php), continuing the southward trend of the Confluence observed since 1993 at decadal time scales (Lumpkin and Garzoli 2011; Goni et al. 2011). In the tropical North Atlantic, the North Brazil Current (NBC) and associated rings serve as interhemispheric conduits for water masses and heat from the South Atlantic to reach the North Atlantic (Goni and Johns 2003). A portion of these waters enter the Caribbean Sea carrying low salinity Amazon River waters (Ffield 2007), known for creating barrier layer conditions that are often associated with hurricane intensification (e.g., Balaguru et al. 2012; Domingues et al. 2015). The average northwestward flow of the NBC in 2023 was 5.9 Sv, a decrease of 1.8 Sv with respect to the previous year and 1.1 Sv lower than its long term (1993–2022) mean value of 7.1±0.8 Sv. Similarly, during 2023 the retroflected flow experienced a sharp decrease of 7.6 Sv with respect to the previous year, for an average of 12.7 Sv, an anomaly of –2.2 Sv from the long-term mean transport of 14.9±1.8 Sv. This average transport during 2023 was within the lowest 15th percentile in terms of its annual mean transport and consistent with the decreased 2023 NECC strength compared to 2022, as the NECC is fed by this retroflection. While this retroflected flow exhibited positive anomalies during the first three months of 2023, negative anomalies prevailed during the rest of the year reaching values as large as 6 Sv during September and October. To the north, the Yucatan Current (YC) and Florida

Current (FC) also exhibited negative anomalies of –0.3 Sv and –1.1 Sv, respectively, compared to their 1993–2022 mean values of 27.8±0.9 Sv and 30.9±1.2 Sv. The YC transport was 0.6 Sv below its 2022 annual mean while the FC transport increased 0.5 Sv from the previous year. The negative anomalies observed in the NBC, especially during the first few months of 2023, are consistent with the negative anomalies by similar magnitude also observed during the last quarter of 2023 in the FC. These three currents constitute an important part of the Atlantic meridional overturning circulation surface pathways and, therefore, negative transport anomalies in the NBC may have first propagated through the Caribbean Sea, then into the Gulf of Mexico by the YC, and finally into the Florida Strait by the FC where anomalies of –5 Sv were observed at the end of 2023. With negative anomalies in the FC transport tied to higher coastal sea level and "sunny day" flooding events along the southeast coast of the United States (Ezer and Atkinson 2014; Domingues et al. 2016; Volkov et al. 2020), further studies addressing the delayed NBC to FC connection may help develop early warnings for such flooding events.

h. Meridional overturning circulation and heat transport in the Atlantic Ocean

—D. L. Volkov, J. K. Willis, W. Hobbs, Y. Fu, S. M. Lozier, W. E. Johns, D. A. Smeed, B. I. Moat, I. Pita, M. Goes, S. Dong, R. H. Smith, and S. Elipot

The meridional overturning circulation (MOC) and meridional heat transport (MHT) are essential indicators of the state of the large-scale ocean circulation and Earth's climate system. Most climate models and proxy-based reconstructions indicate that the Atlantic MOC may already be slowing down towards the end of this century in response to anthropogenic forcing (Weijer et al. 2020; Rahmstorf et al. 2015; Caesar et al. 2018, 2021). In this report, we provide updates on the MOC/MHT estimates across the Atlantic Ocean from the following observing platforms: 1) the Overturning in the Subpolar North Atlantic Program (OSNAP) array (Lozier et al. 2017), which consists of a West section from Canada to Greenland across the Labrador Sea and an East section from Greenland to Scotland, 2) the RAPID-Meridional Overturning Circulation and Heat-flux Array - Western Boundary Time Series (henceforth RAPID) array at ~26.5°N (Moat et al. 2023), and 3) from the combination of satellite and in situ data (synthetic MOC/MHT) at 41°N and at several latitudes in the South Atlantic (Fig. 3.21). As a highlight of this report, initial estimates indicate a record-high MOC/MHT at 41°N, albeit over a short (20-year) observational record.

The most recently published OSNAP time series covers August 2014 to June 2020 (Fu et al. 2023; Fig. 3.22a). The time-mean MOC across the full OSNAP array, consisting of West and East sections, is 16.7±0.6 Sv (the uncertainty is the standard error of the mean). The monthly MOC time series exhibits strong variability ranging from 10 Sv to 25 Sv. The overturning at OSNAP East (16.3±0.6 Sv) dominates the mean and variability of the total subpolar overturning in comparison to that at OSNAP West (3.0±0.5 Sv), consistent with the previously published results (Lozier et al. 2019; Li et al. 2021). Focusing on the seasonal variability, Fu et al. (2023) identified that the MOC peaks in spring (21.1±1.2 Sv) and reaches a minimum in winter (12.3±1.2 Sv) with an amplitude of ~9.0 Sv. Dense water formation in winter and its export are responsible for the peak of the MOC, while the southward Ekman transport, reaching its maximum strength in winter, corresponds to the minimum of the MOC and explains the timing of the MOC trough. The time-mean MHT across the full OSNAP array is 0.50±0.01 PW. The OSNAP East and West sections contribute 0.42±0.01 PW and 0.08±0.01 PW, respectively. The overturning circulation explains 73% of the total MHT variability. The time-mean freshwater transport across the full OSNAP array is −0.36±0.01 Sv (minus denotes southward transport), with nearly equal contributions from West and East sections (−0.18±0.01 Sv and −0.17±0.01 Sv, respectively). This highlights the important role of the Labrador Sea in exporting freshwater to the North Atlantic.

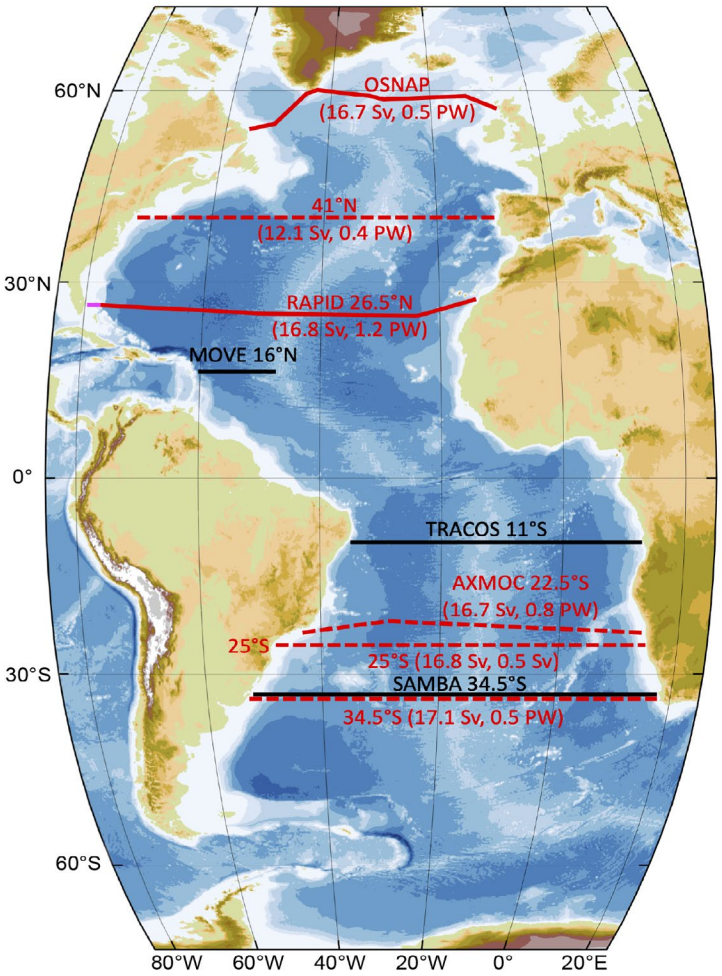

Fig. 3.21. The Atlantic meridional overturning circulation (MOC) observing system: moored arrays (solid red and black lines) and sections across which the MOC and meridional heat transport (MHT) are estimated by synthesizing in situ measurements (Argo, eXpendable BathyThermograph [XBT]) with satellite altimetry data (dashed red lines). The red lines show the sections that have updates covered in this report, while the black lines show the sections for which updates are pending. The record mean MOC and MHT values are shown in parentheses.

The RAPID array, operational since April 2004, is the oldest trans-basin MOC observing array in existence. Since the previous *State of the Climate* report (Volkov et al. 2023b), the RAPID MOC time series has been extended by 14 months to 15 February 2022 (Moat et al. 2023; Fig. 3.22c). The RAPID MHT time series is available through December 2020 (an update will become available upon the processing of cruise data in the Florida Straits). The record mean MOC at ~26.5°N is 16.8 Sv and the standard deviation is 4.6 Sv. The annual mean MOC in 2021 was 15.3 Sv, which is significantly smaller than both the record mean and the annual mean in 2020 (16.9 Sv), given the 0.9 Sv uncertainty of annual transport estimates (McCarthy et al. 2015). The interannual variability of the MOC at ~26.5°N was largely due to the variations in the upper mid-ocean transport (between the Bahamas and Africa) prior to 2018, and it has mainly been driven by the variations in the Florida Current transport after 2018. While an extension of the RAPID MHT time series through February 2022 is pending, the 2004–20 MHT time series has been updated by accounting for the flow-weighted temperature of the Florida Current (Johns et al. 2023). The time-mean MHT at ~26.5°N is 1.20 PW and its standard deviation is 0.38 PW. The MHT variability is dominated by the overturning circulation (and not by the horizontal gyre circulation), as suggested by high correlation between the MHT and MOC (r = 0.96 for 10-day averages). During the decade of 2011–20, the MHT was about 11% smaller than during the first five years of observations. This change was concurrent with a broadening of the Gulf Stream and with altered patterns of ocean heat and freshwater contents (Smeed et al. 2018; Bryden et al. 2020). In 2010–18, both the MOC and MHT were gradually recovering from the 2009/10 dip (Moat et al. 2020), which contributed to oceanic heat convergence in the subtropical gyre, leading to an accelerated sea-level rise along the U.S. southeastern coast and increased flood risk (Domingues et al. 2018; Volkov et al. 2019, 2023a). Johns et al. (2023) explored the ratio MHT/MOC, which is 0.07 PW/Sv on average. Interestingly, the long-term variations of the MHT/MOC ratio are mainly related to the changes in the flow-weighted temperature of the Florida Current that are now included in the overall MHT estimate. There was an overall decrease of the MHT/MOC ratio in 2004–09 and an increase in 2010–20, associated with the cooling and warming of the Florida Current, respectively.

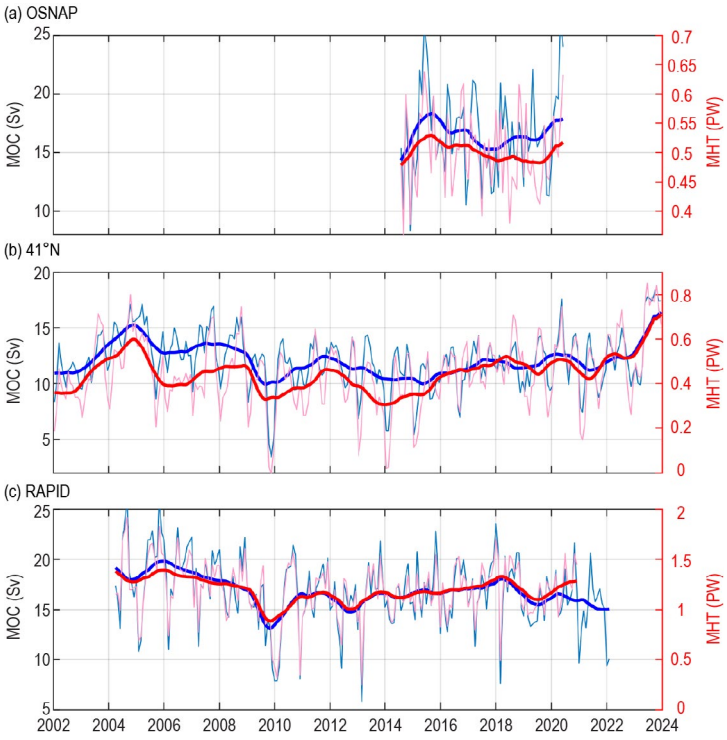

Fig. 3.22. The meridional overturning circulation (MOC) and meridional heat transport (MHT) estimates at the (a) Subpolar North Atlantic Program (OSNAP), (b) 41°N, and (c) RAPID (26.5°N) sections in the North Atlantic. The light blue (pink) lines show the monthly MOC (MHT) time series and the bold blue (red) lines show their yearly moving averages.

The synthetic estimates at 41°N (Fig. 3.22b), based on satellite altimetry and Argo measurements, were reproduced from Willis (2010) and Hobbs and Willis (2012) and extended up to December 2023 (Willis and Hobbs 2024). Each individual estimate represents a three-month average with an uncertainty of 2.3 Sv for the MOC and 0.23 PW for the MHT. The record-high MOC and MHT in 2002–23 were 12.1 Sv and 0.45 PW, respectively. The MOC transport at 41°N was 15.4 Sv in 2023, 12.7 Sv in 2022, and 10.6 Sv in 2021, with only the 2023 mean being statistically different from the time mean given the uncertainty. The MHT in 2022 was 0.67 PW, which is significantly greater than the time mean and the MHT of 0.53 PW in 2022. As the quality control of Argo and altimeter data is always ongoing, improvements in the estimate over the past few years are common. The improvements implemented since the *State of the Climate in 2022* report (Volkov et al. 2023b) resulted in a small decrease in the MOC transport equivalent to about 0.7 Sv in the 2022 values, relative to last year's report. While this change is smaller than the year-to-year

uncertainty in the estimate at 41°N, the recent high values of the MOC in 2023 could be revised after another year of data processing is complete. Nevertheless, last year's increase makes 2023 the highest year on record for MOC volume and heat transports at this latitude in 22 years.

As an assessment of South Atlantic transports, we present novel synthetic MOC/MHT estimates at 22.5°S covering the period from 2007 to 2023 (the AXMOC transect; Fig. 3.23a). The AXMOC time series is obtained by an objective analysis of eXpendable BathyThermograph (XBT) and Argo profiles, optimized by minimizing the difference between the surface in situ dynamic height and sea-surface height from satellite altimetry (Pita et al. 2024). The method adequately represents the energetic Brazil Current, westward propagating signals, and coastal sea-level variability. The time-mean MOC and MHT at 22.5°S are 16.70±0.87 Sv and 0.75±0.06 PW, respectively. In 2023, the MOC and MHT were not significantly different from the record-mean values (by 0.3 Sv and 0.03 PW, respectively). The 2007–23 trends are not statistically significant: 0.50±0.89 Sv decade^{-1} for the MOC and 0.04±0.05 PW decade^{-1} for the MHT. The time-mean and trend estimates agree with those from the synthetic estimates obtained at 25°S using the methodology of Dong et al. (2021); however, the variability in the two estimates is quite different (Fig. 3.23b). This means that the methodology-specific uncertainties are still an important constraint in the overall accuracy of synthetic estimates. At 34.5°S, the MOC and MHT anomalies in 2023 were small and not statistically different from the time mean (Fig. 3.23c).

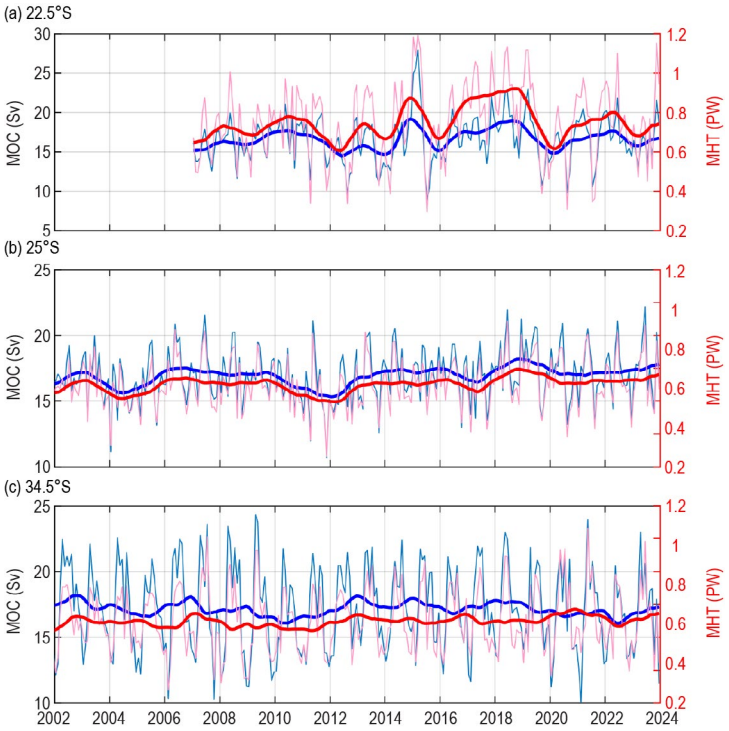

Fig. 3.23. The synthetic meridional overturning circulation (MOC) and meridional heat transport (MHT) estimates at the AXMOC section at (a) 22.5°S and at the (b) 25°S and (c) 34.5°S sections in the South Atlantic. The light blue (pink) lines show the monthly MOC (MHT) time series and the bold blue (red) lines show their yearly moving averages.

The existing observations of the MOC and MHT in the Atlantic Ocean allow an assessment of the climate-relevant state of the large-scale ocean circulation. Because the observational records are still very short compared to climate time scales, it is still not clear whether the MOC has started weakening in response to anthropogenic forcing as suggested by climate models and proxy-based reconstructions. This possible weakening has neither yet been reflected in direct measurements of the MOC at cross-basin moored arrays, nor in synthetic MOC estimates, nor in reconstructions based on sparse hydrographic section data (Caínzos et al. 2022; Worthington et al. 2021; Fu et al. 2020). Continued observations of the MOC and MHT are thus necessary for timely detection of anthropogenic signals and for validating and improving ocean and climate models.

i. Global ocean phytoplankton

—B. A. Franz, I. Cetinić, M. Gao, and T. K. Westberry

Marine phytoplankton contribute roughly 50% of global net primary production, serving the energy needs of oceanic ecosystems and providing a critical pathway for carbon sequestration to the deep oceans (Field et al. 1998; Siegel et al. 2023). The diversity, abundance, and spatio-temporal distribution of phytoplankton are controlled by biotic factors such as zooplankton grazing and viruses, as well as abiotic factors such as nutrient and light availability that are highly dependent on physical properties and processes, including ocean temperature, stratification, and circulation (e.g., Behrenfeld et al. 2006). Spaceborne ocean color radiometers such as Sea-viewing Wide Field-of-view Sensor (SeaWiFS), Moderate Resolution Imaging (MODIS), and the Visible Infrared Imaging Radiometer Suite (VIIRS) provide a synoptic view of spatial and temporal changes in phytoplankton through measurements of near-surface concentrations of phytoplankton pigment chlorophyll-*a* (Chl*a*; mg m^{-3}) and phytoplankton carbon (C_{phy}; mg m^{-3}). Measurements of Chl*a* contain the combined signal of both phytoplankton biomass and physiology, while C_{phy} measures phytoplankton carbon biomass. C_{phy} and Chl*a* often covary, but discrepancies in their distributions are indicative of changes in the physiological or compositional characteristics of phytoplankton communities (Dierssen 2010; Geider et al. 1997; Siegel et al. 2013; Westberry et al. 2016).

In this report, we evaluate the global distribution of phytoplankton over the one-year period from October 2022 through September 2023 (the analysis year) using remotely sensed Chl*a* and C_{phy} measurements from a continuous 26-year record (1997–2023) that combines observations of SeaWiFS (1997–2010), MODIS on Aqua (MODIS-A, 2002–present), and VIIRS on NOAA20 (VIIRS-N_{20}, 2017–present). The MODIS-A daytime sea-surface temperature (SST; °C) is also assessed over a consistent time period to provide context on the physical state of the oceans. The ocean color data from VIIRS-N_{20}, MODIS-A, and SeaWiFS correspond to NASA processing version R2022.0. The Chl*a* product was derived using the Ocean Color Index algorithm of Hu et al. (2012), but with updated algorithm coefficients applied in R2022.0 (Hu et al. 2019; O'Reilly and Werdell 2019). C_{phy} was derived from the particle backscattering coefficient, b_{bp}, at 443 nm (Generalized Inherent Optical Properties algorithm; Werdell et al. 2013; McKinna et al. 2016) and a linear relationship between b_{bp} and C_{phy} (Graff et al. 2015). In merging the time series of SeaWiFS and MODIS-A, differences between the sensors were assessed over the overlapping period from 2003 through 2008, and a mean bias correction (−0.0021 mg m^{-3} in Chl*a* and −6.7e-5 m^{-1} in b_{bp} or −0.78 mg m^{-3} of C_{phy}) was derived and applied to the SeaWiFS time series. Similarly, the overlap period of 2018 to 2020 was used to assess the differences between MODIS-A and VIIRS-N_{20}, and a bias correction (−0.0017 mg m^{-3} in Chl*a* and −3.1e-4 m^{-1} in b_{bp} or −3.6 mg m^{-3} of C_{phy}) was applied to the VIIRS-N_{20} time series. MODIS-A data for 2023 were specifically excluded from this analysis due to as yet uncorrected radiometric calibration instability (G. Meister, NASA/GSFC, personal communication 2024). In contrast, the newer VIIRS-N_{20} instrument has been shown to be very stable (Twedt et al. 2022), and thus it provides the primary reference for the current analysis year. The derived bias corrections between the VIIRS-N_{20} and MODIS-A b_{bp} time series are largely due to the impact of sensor radiometric calibration errors and sensitivity of the b_{bp} retrievals to spectral sampling differences between the sensors (i.e., Werdell and McKinna 2019). While efforts are underway at NASA to reduce this retrieval bias, some additional caution is warranted here in the interpretation of C_{phy} anomalies from VIIRS-N_{20} relative to the climatological record that is dominated by MODIS-A.

Changes in the global distribution of phytoplankton were assessed by subtracting monthly climatological means for MODIS-A Chl*a* and C_{phy} (October 2002–September 2022) from the VIIRS-N_{20} bias-adjusted monthly mean values for the 2023 analysis year. These monthly anomalies were then averaged to produce the global Chl*a* and C_{phy} annual mean anomaly maps (Figs. 3.24a,b). Similar calculations were performed on MODIS-A SST data to produce an equivalent SST annual mean anomaly for the same time period and climatological reference period (Fig. 3.24c). The permanently stratified ocean (PSO), which is used for the analyses depicted in Figs. 3.25 and 3.26, is defined as the region spanning the tropical and subtropical oceans, where

annual average SST is greater than 15°C and surface mixed layers are typically low in nutrients and shallower than the nutricline (black lines near 40°N and 40°S in Fig. 3.24; Behrenfeld et al. 2006).

For the 2023 analysis year, the distribution of SST anomalies (Fig. 3.24c), similar to that of Fig. 3.1a despite the shorter climatological reference period, is consistent with the transition to El Niño conditions in 2023, including a pronounced tongue of anomalously warm waters extending across the equatorial Pacific with anomalously cool waters to the north and south of the tongue. A similar but inverse feature is evident in the Chl*a* anomalies, with concentrations depressed (<10%) within the warm tongue and strongly elevated (>40%) in the adjacent cooler waters (Fig. 3.24a). Similarly, elevated Chl*a* concentrations are observed in the anomalously cool waters of the tropical Indian Ocean. Negative SST anomalies within the PSO generally coincide with deeper surface mixed layers (Deser et al. 2010), resulting in reduced phytoplankton light exposure rates and thus increased cellular Chl*a* and a decoupling between Chl*a* and C_{phy} variability (Behrenfeld et al. 2015). While C_{phy} and Chl*a* anomalies appear to covary in the equatorial Pacific and Indian Oceans, C_{phy} is depressed where Chl*a* is elevated in the North and South Atlantic and in the subtropical North and South Pacific. Patches of elevated and depressed Chl*a* are visible throughout the subpolar and polar regions above and below the PSO (Fig. 3.24a), and the C_{phy} anomalies are generally elevated (Fig. 3.24b). Observed heterogeneity in biomass indicators outside of the PSO is a result of the ephemeral nature of phytoplankton blooms in these waters, as well as poor spatial and temporal sampling due to clouds and low-light conditions that limit our ability to interpret interannual variability in higher-latitude regions.

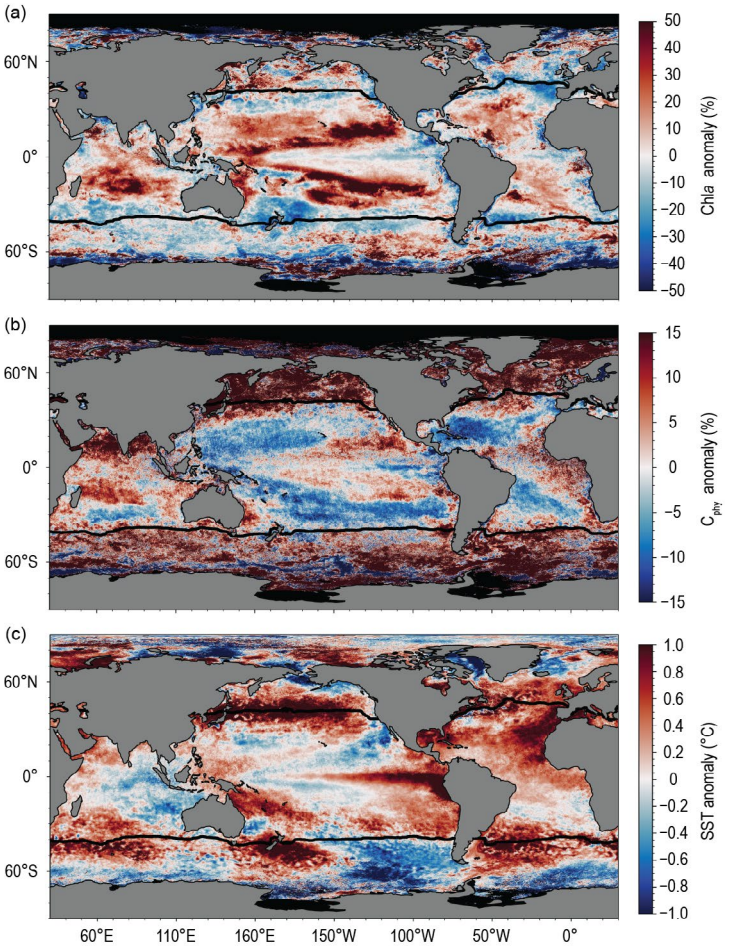

Fig. 3.24. Spatial distribution of average monthly (a) VIIRS-N_{20} chlorophyll-*a* (Chl*a*) anomalies (%), (b) VIIRS-N_{20} phytoplankton carbon (C_{phy}) anomalies (%), and (c) MODIS-A sea-surface temperature (SST) anomalies (°C) for Oct 2022–Sep 2023, where monthly differences were derived relative to the MODIS-A climatological record (Oct 2002–Sep 2022). Chl*a* and C_{phy} are stated as % difference from climatology, while SST is shown as an absolute difference. Also shown in each panel is the location of the mean 15°C SST isotherm (black lines) delineating the permanently stratified ocean (PSO). Differences in the SST anomalies here versus in Fig. 3.1 are owing to differences in climatological periods, smoothing, and data sources.

Annual variability of Chl*a* and C_{phy} within the PSO typically displays two distinct peaks (Figs. 3.25a,b), reflecting the springtime increases of biomass in the Northern Hemisphere (Figs. 3.25c,d) and Southern Hemisphere (SH; Fig. 3.25g,h). The timing of peaks in C_{phy} lag two to three months behind those of Chl*a*, reflecting a reduction in phytoplankton chlorophyll-to-carbon ratios as the seasonal bloom progresses (e.g., Westberry et al. 2016), and the tight coupling between phytoplankton biomass and its losses (e.g., grazing). While the timing of seasonal peaks and troughs observed in the 2023 analysis year is similar to previous years, the SH PSO values for C_{phy} (Fig. 3.25h) and to a lesser degree Chl*a* (Fig. 3.25g) are anomalously low in the first half of the year. This is consistent with the state of the time series at the end of 2022 as reported in Franz et al. (2023) and reflects, at least in part, an erroneous bias in the SH phytoplankton metrics due to the influence of stratospheric aerosols from the 2022 Hunga Tonga–Hunga Ha'apai volcanic eruptions on the atmospheric correction process used for ocean color retrieval

(Zhu et al. 2022; Franz et al. 2024). Another notable feature observed in 2023 is the pronounced outlier of elevated Chl*a* within the tropical PSO in February (Figs. 3.25a,e). This outlier can be traced to an intense bloom of *Noctiluca scintilans* covering the Gulf of Oman and much of the Arabian Sea, where climate-driven seasonal outbreaks of this harmful plankton have been increasing in intensity and range (do Rosário Gomes et al. 2014; Goes et al. 2020).

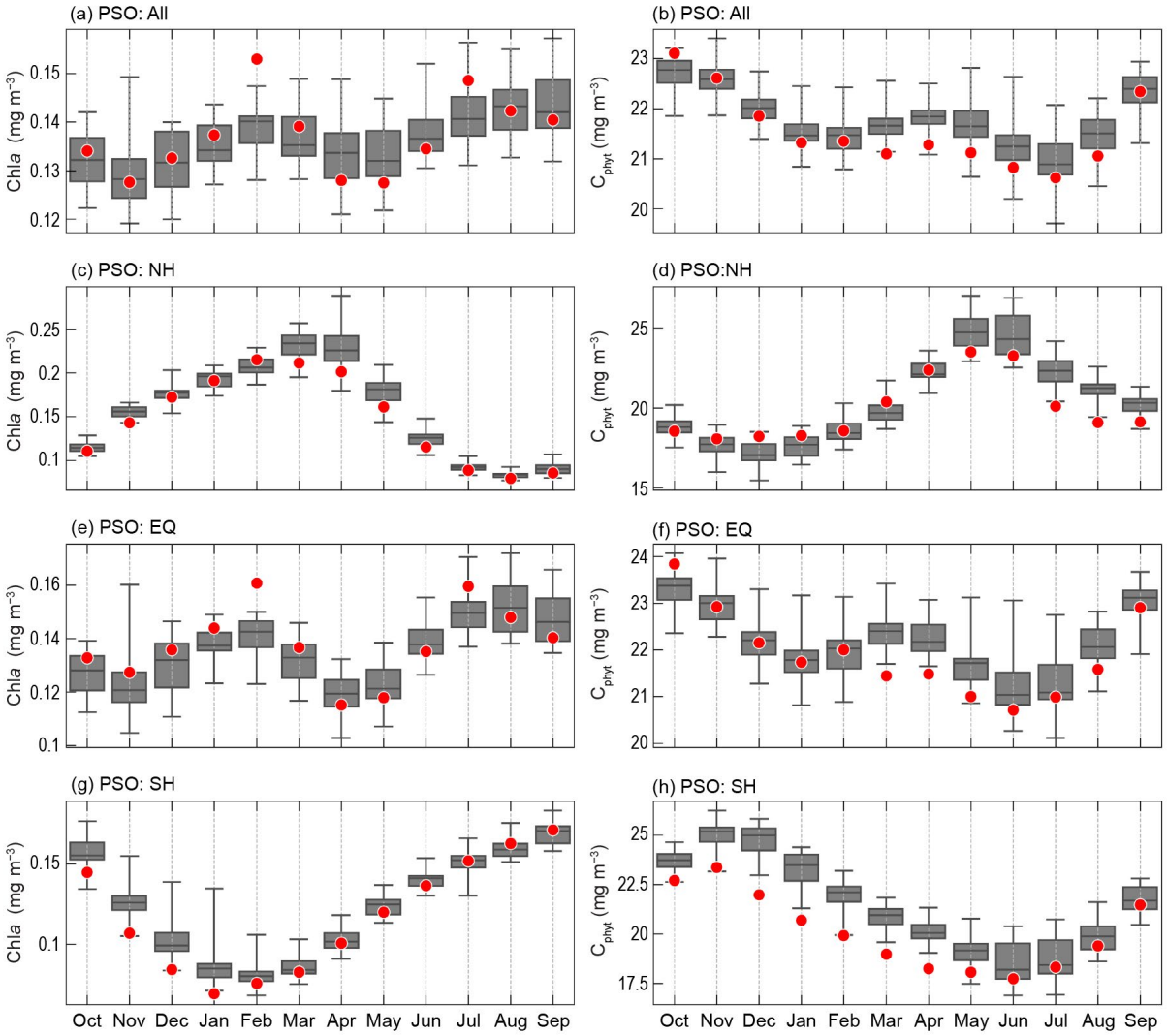

Fig. 3.25. Distribution of Oct 2022–Sep 2023 monthly means (red circles) for (a) VIIRS-N_{20} chlorophyll-*a* (Chl*a*) and (b) VIIRS-N_{20} phytoplankton carbon (C_{phy}) for the permanently stratified ocean (PSO) region (see Fig. 3.26), superimposed on the climatological values as derived from the combined time series of SeaWiFS, MODIS-A, and VIIRS-N_{20} over the period of Oct 1998–Sep 2022. Gray boxes show the interquartile range of the climatology, with a black line for the median value and whiskers extending to minimum and maximum values. Subsequent panels show latitudinally segregated subsets of the PSO for the (c),(d) Northern Hemisphere (NH; above tropics), (e),(f) tropical ±23.5° latitude subregion (EQ), and (g),(h) Southern Hemisphere (SH; below tropics). Units for (a), (c), (e), and (g) are Chl*a* (mg m^{-3}) and those for (b), (d), (f), and (h) are C_{phy} (mg m^{-3}).

Over the 26-year time series of spatially averaged monthly mean Chl*a* within the PSO, concentrations vary by 5.8% (0.008 mg m^{-3}, standard deviation) around a long-term average of 0.136 mg m^{-3} (Fig. 3.26a). C_{phy} over the same 26-year period varies by 3.2% (0.69 mg m^{-3}) around an average of 21.8 mg m^{-3} (Fig. 3.26c). Chl*a* monthly anomalies within the PSO (Fig. 3.26b) vary by 4.5% (0.006 mg m^{-3}) over the multi-mission time series, with the largest deviations generally associated with El Niño–Southern Oscillation (ENSO) events (r=−0.38), as demonstrated by the correspondence of Chl*a* anomaly variations with the Multivariate ENSO Index (MEI; Wolter and Timlin 1998; presented in the inverse to illustrate the covariation). C_{phy} anomalies (Fig. 3.26d), which vary by 2.0% (0.45 mg m^{-3}), are less correlated with the MEI (r=−0.27) due to the inherent lag between environmental change, phytoplankton growth, and biomass accumulation. The

anomalies in 2023 for Chl*a* and C_{phy} within the PSO indicate modestly depressed concentrations overall, consistent with the transition to El Niño conditions that limit phytoplankton production.

Through the continuous observation of ocean color, we are able to track variability in the global distribution of phytoplankton that drive biogeochemical processes, govern the role of the oceans in the global carbon cycle, and through their productivity exert a controlling influence on marine ecosystems, food webs, and fisheries. Subtle changes in Chl*a* and C_{phy} allow us to distinguish climate-driven variability in phytoplankton biomass from changes in physiology and community response. The recently launched Plankton, Aerosol, Cloud, ocean Ecosystem (PACE) mission, which carries the first global hyperspectral instrument designed for the measurement of ocean color, should enable a more precise identification of phytoplankton absorption features (Werdell et al. 2019) and separation of those features from non-algal optical contributions (e.g., Pahlevan et al. 2021; Siegel et al. 2005) and thereby facilitate the assessment of changes in phytoplankton species or community composition (e.g., Kramer et al. 2022; Lange et al. 2020) that will further advance our ability to disentangle the impacts of climate forcing on global phytoplankton communities.

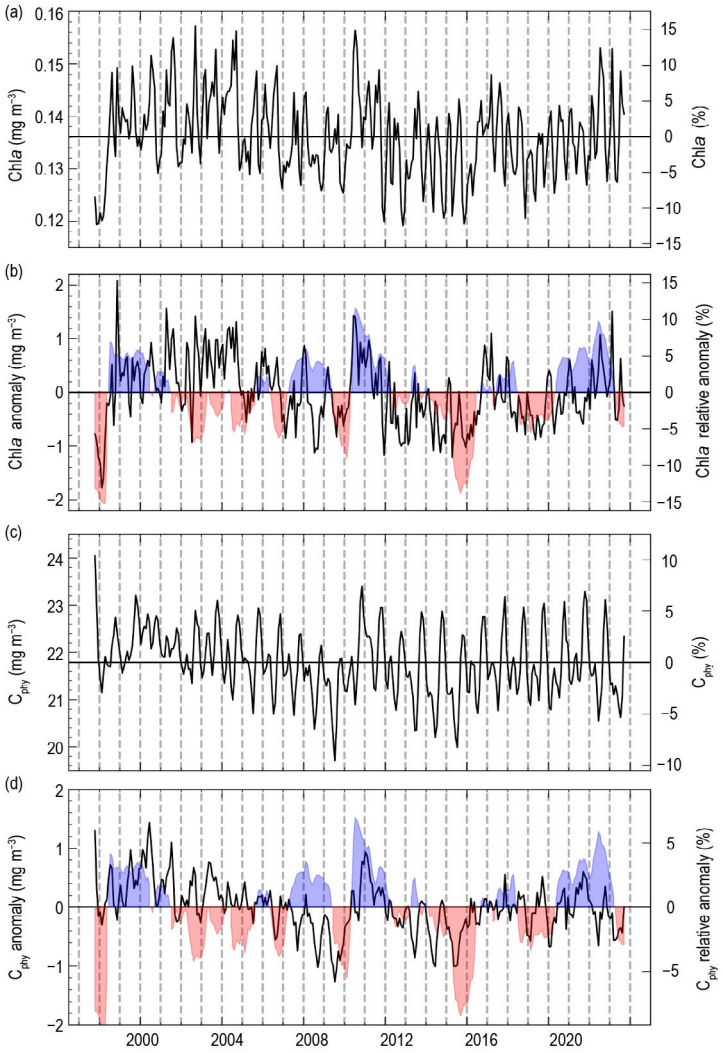

Fig. 3.26. Twenty-six-year, multi-mission record of chlorophyll-*a* (Chl*a*; mg m^{-3}) and phytoplankton carbon (C_{phy}; mg m^{-3}) averaged over the permanently stratified ocean (PSO; Oct 1997–Sep 2023). (a) Monthly Chl*a*, with the horizontal line indicating the multi-mission mean Chl*a* concentration for the entire PSO region. (b) Monthly Chl*a* anomalies after subtraction of the multi-mission climatological mean (Fig. 3.25a). (c) Monthly C_{phy}, with the horizontal line indicating the multi-mission mean C_{phy} concentration for the entire PSO region. (d) Monthly C_{phy} anomalies after subtraction of the multi-mission climatological mean (Fig. 3.25b). Shaded blue and red colors show the Multivariate El Niño–Southern Oscillation (ENSO) Index (MEI), inverted and scaled to match the range of the Chl*a* and C_{phy} anomalies, where blue indicates La Niña and red indicates El Niño conditions.

j. Global ocean carbon cycle

—R. Wanninkhof, J. A. Triñanes, P. Landschützer, A. Jersild, R. A. Feely, and B. R. Carter

1. INTRODUCTION

The oceans play a major role in the global carbon cycle by taking up a substantial fraction of the excess carbon dioxide that humans release into the atmosphere. As a consequence of humankind's collective carbon dioxide (CO_2) release into the atmosphere, referred to as anthropogenic CO_2 (C_{ant}) emissions, the atmospheric CO_2 concentration has risen from pre-industrial levels of about 278 ppm (parts per million) to 419.3±0.1 ppm in 2023 (see section 2g1 for details). Marine C_{ant} is the major cause of anthropogenic ocean acidification. Over the last decade the global ocean has continued to take up C_{ant} and therefore is a major mediator of global climate change. Of the 10.9±0.8 Pg C yr^{-1} C_{ant} released during the period 2013–22, 2.8±0.4 Pg C yr^{-1} (26%) accumulated in the ocean, 3.3±0.8 Pg C yr^{-1} (28%) accumulated on land, and 5.2±0.02 Pg C yr^{-1} (46%) remained in the atmosphere, with an imbalance of −0.4 Pg C yr^{-1} (–3%; see Table 7 in Friedlingstein et al. 2023). This decadal C_{ant} uptake estimate is a consensus view from a combination of measured ocean decadal CO_2 inventory changes, global ocean biogeochemical models, and global air–sea CO_2 flux estimates based on surface ocean fugacity of CO_2 (fCO_{2w})[1] measurements.

This year saw the release of several significant syntheses of ocean C_{ant}, including global and regional chapters of the second REgional Carbon Cycle Assessment and Processes (RECCAP2) assessment (see e.g., DeVries et al. 2023). The C_{ant} accumulation rate estimates from these studies agree with the overall rates given by Friedlingstein et al. (2023), but show differing patterns of variability in the ocean C_{ant} accumulation rate with time.

2. AIR–SEA CARBON DIOXIDE FLUXES

Ocean uptake of CO_2 is estimated from the net air–sea CO_2 flux derived from a bulk flux formula determined from the product of air and surface-seawater fCO_2 difference (ΔfCO_2) and gas transfer coefficients. Gas transfer is parameterized with wind as described in Wanninkhof (2014). This provides a net flux estimate. Here, 0.65 Pg C yr^{-1} is applied as the river adjustment (Regnier et al. 2022) as recommended in the Global Carbon Budget 2023 and RECCAP2 to convert the net flux to the C_{ant} flux. The data sources for fCO_{2w} are annual updates of observations from the Surface Ocean CO_2 Atlas (SOCAT) composed of moorings, autonomous surface vehicles, and ship-based observations (Bakker et al. 2016), with SOCAT v2023 containing 35.6 million data points from 1957 through 2022 (Bakker et al. 2023). The increased observations and improved mapping techniques, including machine learning methods summarized in Rödenbeck et al. (2015), now provide annual global fCO_{2w} fields on a 1° latitude × 1° longitude grid at monthly time scales. For this report, we use a self-organizing maps feed-forward neural network (SOM-FNN) approach of Landschützer et al. (2013, 2014) using SOCATv2023 for training. The monthly 2023 fCO_{2w} maps use as predictor variables: sea-surface temperature (SST; Rayner et al. 2003); chlorophyll-*a* (Globcolour; Maritorena et al. 2010); mixed-layer depth (de Boyer Montégut et al. 2004; Schmidtko et al. 2013), and salinity (Good et al. 2013). For atmospheric CO_2, the zonally-resolved NOAA marine boundary layer atmospheric CO_2 product is used (Dlugokencky et al. 2021). The gas transfer coefficients are determined using European Centre for Medium-Range Weather Forecasts Reanalysis version 5 (ERA5) winds (Hersbach et al. 2018). The air–sea CO_2 flux maps for 2023 do not include fCO_{2w} observations for 2023 but rather are created by extrapolation using the predictor variables. The uptake of the fCO_2-based models such as the Flanders Marine Institute (VLIZ) SOM-FNN used here is substantially larger than the model-based estimates, with differences in uptake of ≈1 Pg C in 2022.

The VLIZ SOM FNN results (Fig. 3.27) show a steady ocean CO_2 sink from 1982 to 1998, followed by a period of decreasing uptake from 1998 to 2002. There is a strong increase in the ocean sink from 2002 onward that continues through 2016, after which the global uptake shows a small increase up to 2023. The C_{ant} flux of 3.8 Pg C yr^{-1} for 2023 (green line in Fig. 3.27) shows a substantial 0.34 Pg C increase in uptake above the 2013–22 average of 3.46±0.11 Pg C yr^{-1}. The amplitude of seasonal variability is ≈1.2 Pg C with a minimum uptake in June–September.

[1] The fugacity is the partial pressure of CO_2 (pCO_2) corrected for non-ideality. They are numerically similar for surface waters with $fCO_2 \approx 0.994\ pCO_2$.

Sea-surface temperature anomalies can manifest themselves in differing ways on fCO_{2w}. Positive SST anomalies will decrease solubility and thereby increase fCO_{2w}. However, in regions with high fCO_{2w} due to upwelling, warmer SSTs as a result of decreased upwelling of cold CO_2-rich water will lower fCO_{2w}.

The annual average flux map for 2023 (Fig. 3.28a) shows the characteristic pattern of high effluxes (ocean-to-air CO_2 fluxes) in tropical, coastal upwelling, and open-ocean upwelling regions. Coastal upwelling regions include those in the Arabian Sea and off the west coasts of North and South America. The western Bering Sea was a strong CO_2 source in 2023, a clear juxtaposition to the strong sink in the surrounding regions. This regional source is hypothesized to result from a local outcropping of shallow isopycnals with high CO_2 values, but this has not been independently verified. Cumulatively, the regions of effluxes are substantial CO_2 sources to the atmosphere (≈1 Pg C). The primary CO_2 uptake regions are in the subtropical and subpolar regions. The largest sinks are poleward of the sub-tropical fronts. In the Southern Ocean, the area near the polar front (~60°S) was a weak to moderate sink in 2023.

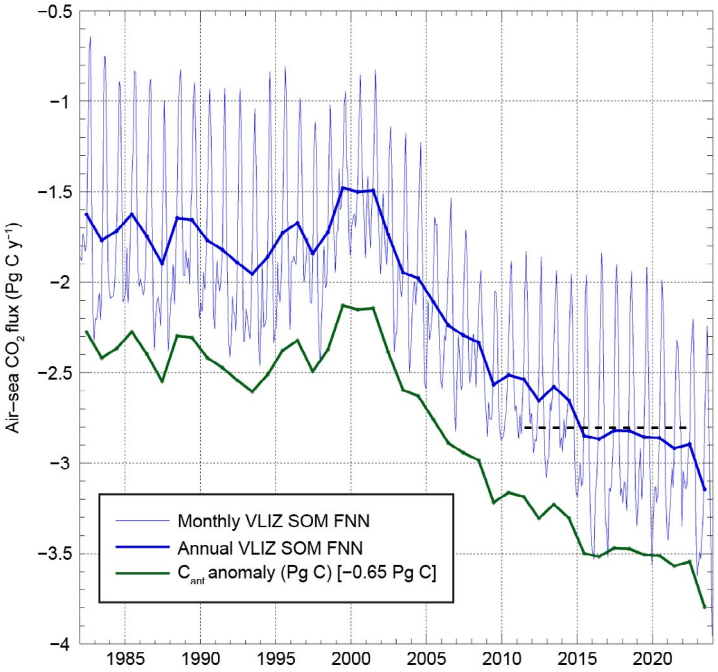

Fig. 3.27. Global annual (thick blue line) and monthly (thin blue line) net air-sea carbon dioxide (CO_2) fluxes (Pg C yr^{-1}) for 1982–2023 using the Flanders Marine Institute (VLIZ) self-organizing maps feed-forward neural network (SOM-FNN) output. The annual anthropogenic CO_2 (C_{ant}) air–sea flux (thick green line) includes a riverine adjustment of –0.65 Pg C. The black dashed line is the 2013–22 mean C_{ant} flux based on models and fCO_2 products (Friedlingstein et al. 2023). Negative values indicate CO_2 uptake by the ocean.

In the Northern Hemisphere, the entire North Atlantic is a large sink while in the North Pacific the sink region is punctuated by a substantial source of CO_2 in the western to central Bering Sea. The Northern Hemisphere sinks are, in part, due to the position of the western boundary currents whose cooling waters when transported poleward cause an increase in solubility and contribute to CO_2 uptake at high latitudes. The Gulf Stream/North Atlantic Drift in the Atlantic extends farther north than the Kuroshio in the Pacific, extending the region of a strong sink in the North Atlantic.

The ocean carbon uptake anomalies (Fig. 3.28c) in 2023 relative to the 1990–2020 average, adjusted for the 20-year trend, show the substantial effect of the El Niño condition in the second half of 2023, with reduced upwelling and lower effluxes in the eastern equatorial Pacific (EEP). The Southern Ocean shows a band of increased uptake (≈45°S–60°S), associated with a weak positive SST anomaly. The larger sink is attributed to weaker exchange with deep water in these regions of mode water outcropping (Hauck et al. 2023). Large regions in the subtropical gyres show positive anomalies due to the marine heat waves prevalent during 2023 (Sidebar 3.1) and the associated lower solubility enhancing outgassing or decreased uptake. Of note is the wedge of anomalously high outgassing in the central equatorial Pacific adjacent to the region of decreased outgassing due to repressed upwelling showing that in the Central Pacific, the thermal effects are larger than the impact of decreased upwelling. Globally, the impact of reduced outgassing in the EEP due to the El Niño, and increasing uptake in the Southern Ocean due to decreased exposure of the surface-to-mode waters, is much greater than the increase in fCO_{2w} due to the marine heatwaves in mid- and high latitudes (Sidebar 3.1).

The spatial differences in CO_2 fluxes between 2023 and 2022 (Fig. 3.28b) resemble that of the longer-term anomaly (Fig. 3.28c). The negative flux anomalies in the EEP are due to the transition from the triple dip La Niña to a strong El Niño in the summer of 2023. The regions of increased effluxes/decreased influxes in the Northern Hemisphere correspond with the positive SST anomalies in the boreal summer. The increased uptake in the Southern Ocean (45°S–60°S) latitude

band resembles that of the longer-term anomaly with the same attribution. The strong source in the western Bering Sea (Fig 3.28a) shows up as a positive anomaly compared to the long-term average but has decreased in the last year.

3. OCEAN INTERIOR INVENTORY ESTIMATES

An important insight from the RECCAP2 synthesis study is that the global air-to-sea CO_2 flux, which was found to have increased by 0.61±0.12 PgC yr^{-1} from 2001 to 2018, is dominated by the flux of C_{ant}. C_{ant} accumulation rate estimates averaged across years therefore provide a constraint on the decadal air–sea CO_2 flux. The C_{ant} in Fig. 3.27 is derived from the net air–sea CO_2 flux by assuming a constant source of CO_2 to the ocean from land and sediment fluxes and assuming that there are no natural variations in the ocean carbon inventory; however, the RECCAP2 synthesis also finds that climate-driven variability in the natural ocean carbon inventory is potentially a significant component of the overall CO_2 flux variations and is inconsistently represented across CO_2 flux estimation methods. It is therefore important to obtain independent estimates of C_{ant} and to separately quantify both the C_{ant} changes and the overall ocean carbon inventory changes.

Ocean carbon inventory changes provide means of estimating ocean C_{ant} accumulation quantity directly. The global RECCAP2 synthesis (DeVries et al. 2023) estimated an overall C_{ant} accumulation rate of 2.7±0.3 Pg C yr^{-1} from 2001 to 2018 based on a collection of reanalysis-forced global ocean biogeochemical model experiments and simulations with an ocean circulation inverse model fit to measurements of ocean physics and transient tracers for air–sea gas exchange. This result is indistinguishable from the consensus estimate of 2.8±0.4 Pg C yr^{-1} for 2013–22 of Friedlingstein et al. (2023) and the 2.8±0.3 Pg C yr^{-1} estimate for 1994–2014 given by Müller et al. (2023) from an analysis of multiple decades of seawater ocean carbon content measurements; however, the RECCAP2 synthesis finds that the global ocean C_{ant} accumulation rate increased by 0.34±0.06 PgC yr^{-1} $decade^{-1}$ and 0.41±0.03 PgC yr^{-1} $decade^{-1}$ from 2001 to 2018 from reanalysis-forced and steady-state ocean circulation inverse models, respectively, whereas the observational study by Müller et al. (2023) showed that the accumulation rate instead slowed by ~0.2 PgC yr^{-1} $decade^{-1}$ between 1994–2004 and 2004–14. Müller et al. (2023) argue that C_{ant} accumulation would be expected to intensify by ~0.2 PgC yr^{-1} $decade^{-1}$ given steady state ocean circulation, constant seawater chemistry, and the observed accelerating atmospheric C_{ant} accumulation between these time periods, so the observed accumulation rate in fact slowed down by 15±11% relative to expectations; however, this claim of a slowing ocean C_{ant} sink, which they attribute to changing ocean chemistry and circulation, can

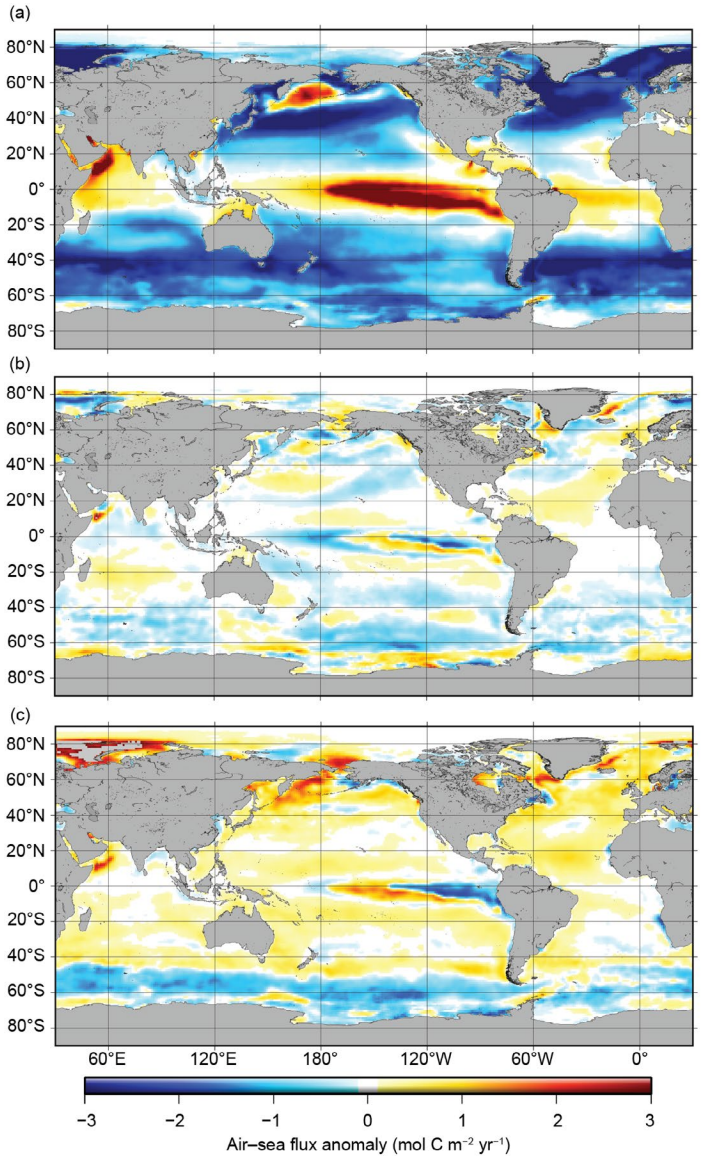

Fig. 3.28. Global map of (a) net air–sea carbon dioxide (CO_2) fluxes for 2023, (b) net air–sea CO_2 flux anomalies for 2023 minus 2022, and (c) net air–sea CO_2 flux anomalies for 2023 relative to 1990–2020 average values adjusted for the 20-year trend using the Flanders Marine Institute (VLIZ) self-organizing maps feed-forward neural network (SOM-FNN) approach. Units are all mol C m^{-2} yr^{-1}. Ocean CO_2 uptake regions are shown in blue. For reference, a global ocean CO_2 uptake of 2.8 Pg C yr^{-1} equals a flux density of –0.65 mol C m^2 yr^{-1}.

only be made with modest statistical confidence. Müller et al. (2023) find meaningful differences from earlier regional estimates: In the South Pacific and the North Atlantic, Müller et al. (2023) find statistically insignificant decreases in accumulation rates where earlier studies (Carter et al. 2019; Woosley et al. 2016) found statistically significant increasing rates; in the South Atlantic, they find a rapidly increasing accumulation rate where an earlier study (Woosley et al. 2016) found a consistent accumulation rate. Methodological decisions that differed among these studies can lead to meaningful variations in the findings.

Comparisons of C_{ant} accumulation rate variations from Müller et al. (2023), the RECCAP2 synthesis, and earlier analyses reveal consistency between the multi-decadal C_{ant} accumulation rates but also show different patterns of regional and temporal accumulation rate variability (Fig. 3.29; Sabine et al. 2004; Gruber et al. 2019; Mueller et al. 2023; Lauvset et al. 2016; DeVries 2014; Davila et al. 2022; Khatiwala et al. 2009; Waugh et al. 2006). The disagreements in the findings from these various C_{ant} accumulation rate estimates therefore parallel an increasing disagreement noted in CO_2 flux estimates derived from global ocean biogeochemistry models and fCO_2 products (Friedlingstein et al. 2023). In both cases the broad patterns of natural and anthropogenic ocean carbon accumulation are clear, but the decadal variations in ocean carbon accumulation are less well constrained and in need of robust uncertainty quantification.

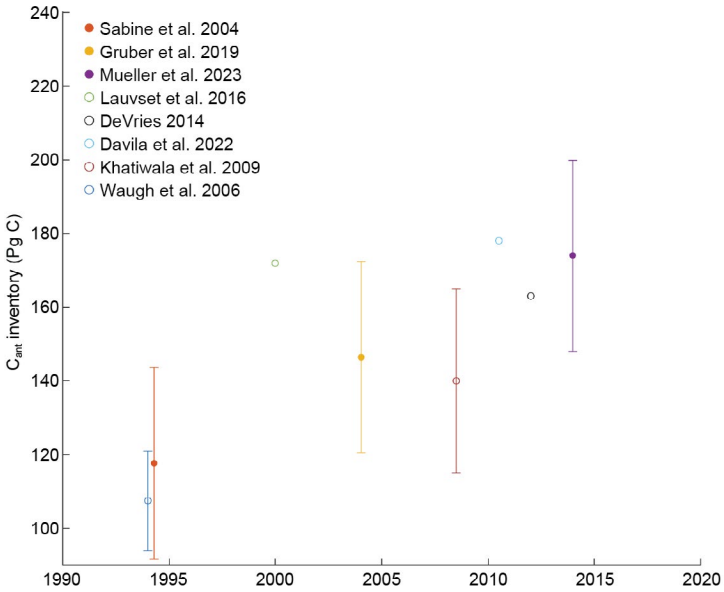

Fig. 3.29. A compilation of data-based global ocean anthropogenic carbon inventory estimates vs. the year for which the estimate is made. While these estimates vary considerably with respect to methodology and the underlying measurements, a general increasing trend can be seen consistent with ongoing ocean anthropogenic CO_2 (C_{ant}) accumulation.

Appendix 1: Acronyms

ACC	Antarctic Circumpolar Current
BASS	Blended Analysis of Surface Salinity
b_{bp}	particle backscattering coefficient
C_{ant}	anthropogenic CO_2
CERES	Clouds and the Earth's Radiant Energy Systems
Chl*a*	chlorophyll-*a*
CO_2	carbon dioxide
COARE	Coupled Ocean Atmosphere Response Experiment
C_{phy}	phytoplankton carbon
E	Evaporation
EBAF	Energy Balanced and Filled
EEP	eastern equatorial Pacific
EKE	eddy kinetic energy
ENSO	El Niño–Southern Oscillation
ERA5	European Centre for Medium-Range Weather Forecasts Reanalysis version 5
FC	Florida Current
fCO_{2w}	surface ocean fugacity of CO_2
FlashFlux	Fast Longwave And Shortwave Radiative Fluxes
GMSL	global mean sea level
GPCP	Global Precipitation Climatology Project
IOD	Indian Ocean dipole
ITCZ	Intertropical Convergence Zone
LH	latent heat
LW	longwave radiation
MEI	Multivariate ENSO Index
MHT	meridional heat transport
MHW	marine heatwave
MOC	meridional overturning circulation
MODIS	Moderate Resolution Imaging Spectroradiometer
MODIS-A	Moderate Resolution Imaging Spectroradiometer on Aqua
NBC	North Brazil Current
NECC	North Equatorial Countercurrent
OAFlux	Objectively Analyzed Air–Sea Heat Fluxes
OHCA	ocean heat content anomaly
OSNAP	Overturning in the Subpolar North Atlantic Program
P	Precipitation
PACE	Plankton, Aerosol, Cloud, ocean Ecosystem
pCO_2	partial pressure of CO_2
PDO	Pacific Decadal Oscillation
PSO	permanently stratified ocean
Q_{net}	net surface heat flux
RAPID	Rapid Climate Change
RECCAP2	REgional Carbon Cycle Assessment and Processes
SD	standard deviation
SeaWiFS	Sea-viewing Wide Field-of-view Sensor
SEC	South Equatorial Current
SH	Southern Hemisphere
SIO	Scripps Institution of Oceanography
SMAP	Soil Moisture Active Passive

SMOS	Soil Moisture and Ocean Salinity
SOCAT	Surface Ocean CO_2 Atlas
SOM-FNN	self-organizing maps feed-forward neural network
SPCZ	South Pacific Convergence Zone
SSS	sea-surface salinity
SST	sea-surface temperature
SSTA	sea-surface temperature anomaly
SW	shortwave radiation
VIIRS	Visible Infrared Imaging Radiometer Suite
VIIRS-N_{20}	Visible Infrared Imaging Radiometer Suite on NOAA20
VLIZ	Flanders Marine Institute
XBT	Expendable Bathythermograph
YC	Yucatan Current
$\Delta\, fCO_2$	fCO_2 difference

Appendix 2: Datasets and sources

Section 3b Sea Surface Temperature

Sub-section	General Variable or Phenomenon	Specific dataset or variable	Source
3b	Sea Surface Temperature	ERSSTv5	https://doi.org/10.7289/V5T72FNM
3b	Sea Surface Temperature	HadSST4	https://www.metoffice.gov.uk/hadobs/hadsst4/
3b	Sea Surface Temperature	NOAA Daily Optimum Interpolated Temperature (DOISST)	https://doi.org/10.25921/RE9P-PT57

Section 3c Ocean Heat Content

Sub-section	General Variable or Phenomenon	Specific dataset or variable	Source
3c	Ocean Heat Content	Argo	http://doi.org/10.17882/42182#98916
3c	Ocean Heat Content	RFROM	https://www.pmel.noaa.gov/rfrom/
3c	Ocean Heat Content	CLIVAR and Carbon Hydrographic Data Office	https://cchdo.ucsd.edu/
3c	Ocean Heat Content	IAP/CAS	http://www.ocean.iap.ac.cn/pages/dataService/dataService.html
3c	Ocean Heat Content	MRI/JMA	www.data.jma.go.jp/gmd/kaiyou/english/ohc/ohc_global_en.html
3c	Ocean Heat Content	NCEI	https://www.ncei.noaa.gov/access/global-ocean-heat-content/
3c	Ocean Heat Content	PMEL/JPL/JIMAR	http://oceans.pmel.noaa.gov
3c	Ocean Heat Content	UK Met Office EN4.2.2	https://www.metoffice.gov.uk/hadobs/en4/download-en4-2-2.html

Section 3d Salinity

Sub-section	General Variable or Phenomenon	Specific dataset or variable	Source
3d2	Ocean Salinity	Argo	https://usgodae.org/argo/argo.html
3d2	Ocean Salinity	Blended Analysis for Surface Salinity	ftp://ftp.cpc.ncep.noaa.gov/precip/BASS
3d2	Ocean Salinity	World Ocean Atlas 2013	www.nodc.noaa.gov/OC5/woa13/
3d3	Ocean Salinity	NCEI salinity anomaly	https://www.ncei.noaa.gov/access/global-ocean-heat-content/
3d3	Ocean Salinity	World Ocean Atlas 2018	www.nodc.noaa.gov/OC5/woa18/

Section 3e Global ocean heat, freshwater, and momentum flux

Sub-section	General Variable or Phenomenon	Specific dataset or variable	Source
3e1	Air-sea fluxes (shortwave/longwave radiation)	CERES Energy Balanced and Filled version 4.2	https://asdc.larc.nasa.gov/project/CERES/CERES_EBAF_Edition4.2
3e1	Air-sea fluxes (shortwave/longwave radiation)	CERES FLASHflux 4A product	https://cmr.earthdata.nasa.gov/search/concepts/C1719147151-LARC_ASDC.html
3e1	Air-sea fluxes (latent heat/sensible heat)	OAFlux2	https://oaflux.whoi.edu/
3e2	Precipitation	Global Precipitation Climatology Project (GPCP) v2.3	https://psl.noaa.gov/data/gridded/data.gpcp.html
3e2	Evaporation	OAFlux2	https://oaflux.whoi.edu/
3e3	Wind stress	OAFlux2	https://oaflux.whoi.edu/

Section 3f Sea Level variability and change

Sub-section	General Variable or Phenomenon	Specific dataset or variable	Source
3f	Ocean Heat Content	Argo monthly climatology	https://sio-argo.ucsd.edu/RG_Climatology.html
3f	Ocean Mass	GRACE/GRACE FO	https://grace.jpl.nasa.gov/data/get-data
3f	Sea Level / Sea Surface Height	Argo	https://usgodae.org/argo/argo.html
3f	Sea Level / Sea Surface Height	NASA MEaSURES	https://podaac.jpl.nasa.gov/dataset/SEA_SURFACE_HEIGHT_ALT_GRIDS_L4_2SATS_5DAY_6THDEG_V_JPL2205
3f	Sea Level/Sea Surface Height	NASA Sea Level Change Program	https://podaac.jpl.nasa.gov/dataset/MERGED_TP_J1_OSTM_OST_ALL_V51
3f	Sea Level / Sea Surface Height	NCEI steric sea level	https://www.ncei.noaa.gov/access/global-ocean-heat-content/
3f	Sea Level / Sea Surface Height	NOAA Laboratory for Sea Level Altimetry	www.star.nesdis.noaa.gov/sod/lsa/SeaLevelRise/LSA_SLR_timeseries.php
3f	Sea Level / Sea Surface Height	Tide Gauge	http://uhslc.soest.hawaii.edu/
3f	Sea Level / Sea Surface Height	University of Texas Center for Space Research Gravity field	https://podaac.jpl.nasa.gov/dataset/TELLUS_GRAC_L3_CSR_RL06_OCN_v04

Section 3g Surface Currents

Sub-section	General Variable or Phenomenon	Specific dataset or variable	Source
3g	ocean currents	Global Drifter Program	https://www.aoml.noaa.gov/phod/gdp/interpolated/data/all.php
3g3	ocean currents	Atlantic ocean monitoring	https://www.aoml.noaa.gov/phod/altimetry/cvar/

Section 3h Meridional Overturning Circulation and Heat Transport in the Atlantic Ocean

Sub-section	General Variable or Phenomenon	Specific dataset or variable	Source
3h	ocean currents	Atlantic Ship of Opportunity XBT	https://www.aoml.noaa.gov/phod/goos/xbt_network/
3h	ocean currents	Argo	https://usgodae.org/argo/argo.html
3h	ocean currents	Florida Current transport	https://www.aoml.noaa.gov/phod/floridacurrent/data_access.php
3h	ocean currents	Global Temperature and Salinity Profile Program (GTSPP)	https://www.ncei.noaa.gov/products/global-temperature-and-salinity-profile-programme
3h	ocean currents	MOVE array	http://www.oceansites.org/tma/move.html
3h	ocean currents	OSNAP	https://www.o-snap.org/
3h	ocean currents	RAPID array	https://rapid.ac.uk/rapidmoc/
3h	ocean currents	SAMBA	http://www.oceansites.org/tma/samba.html

Section 3i Global Ocean Phytoplankton

Sub-section	General Variable or Phenomenon	Specific dataset or variable	Source
3i	Phytoplankton, Ocean Color	MODIS-Aqua	https://oceancolor.gsfc.nasa.gov/reprocessing/

Section 3j Global Ocean Carbon Cycle

Sub-section	General Variable or Phenomenon	Specific dataset or variable	Source
3j2	Ocean Carbon	SOCAT version 2022	https://doi.org/10.25921/r7xa-bt92
3j2	Sea Surface Temperature	NOAA Optimum Interpolation SST (OISST) v2.1	https://www.ncei.noaa.gov/products/optimum-interpolation-sst
3j2	Chlorophyll	GlobColour	https://www.globcolour.info/
3j2	Atmospheric Carbon Dioxide	NOAA Greenhouse Gas Marine Boundary Layer Reference	https://gml.noaa.gov/ccgg/mbl/mbl.html
3j2	Winds [Near] Surface	ERA5	https://www.ecmwf.int/en/forecasts/datasets/reanalysis-datasets/era5
3j2	Ocean Salinity	Hadley Center EN4	https://www.metoffice.gov.uk/hadobs/en4/
3j3	Ocean Temperature	Argo monthly climatology	https://sio-argo.ucsd.edu/RG_Climatology.html
3j3	Ocean Salinity	Argo monthly climatology	https://sio-argo.ucsd.edu/RG_Climatology.html

Sidebar 3.1 Marine Heatwaves in 2023

Sub-section	General Variable or Phenomenon	Specific dataset or variable	Source
SB3.1	Sea Surface Temperature	OISSTv2.1.	https://www.ncei.noaa.gov/products/optimum-interpolation-sst

References

Adler, R. F., and Coauthors, 2018: The Global Precipitation Climatology Project (GPCP) monthly analysis (new version 2.3) and a review of 2017 global precipitation. *Atmosphere*, **9**, 138, https://doi.org/10.3390/atmos9040138.

Bakker, D. C. E., and Coauthors, 2016: A multi-decade record of high-quality fCO_2 data in version 3 of the Surface Ocean CO_2 Atlas (SOCAT). Earth Syst. *Sci. Data*, **8**, 383–413, https://doi.org/10.5194/essd-8-383-2016.

—— , and Coauthors, 2023: Surface Ocean CO2 Atlas Database version 2023 (SOCATv2023) (NCEI Accession 0278913). NOAA/NCEI, accessed 4 January 2024, https://doi.org/10.25921/r7xa-bt92.

Balaguru, K., P. Chang, R. Saravanan, L. R. Leung, Z. Xu, M. Li, and J. S. Hsieh, 2012: Ocean barrier layers' effect on tropical cyclone intensification. *Proc. Natl. Acad. Sci. USA*, **109**, 14343–14347, https://doi.org/10.1073/pnas.1201364109.

Barnoud, A., and Coauthors, 2021: Contributions of altimetry and Argo to non-closure of the global mean sea level budget since 2016. *Geophys. Res. Lett.*, **48**, e2021GL092824, https://doi.org/10.1029/2021GL092824.

Beal, L., V. Hormann, R. Lumpkin, and G. Foltz, 2013: The response of the surface circulation of the Arabian Sea to monsoonal forcing. *J. Phys. Oceanogr.*, **43**, 2008–2022, https://doi.org/10.1175/JPO-D-13-033.1.

Beckley, B., and Coauthors, 2021: Global mean sea level trend from integrated multi-mission ocean altimeters TOPEX/Poseidon, Jason-1, OSTM/Jason-2, and Jason-3 version 5.1. PODAAC, accessed 29 January 2024, https://doi.org/10.5067/GMSLM-TJ151.

—— , and Coauthors, 2023: Assessment of reprocessed TOPEX/Jason/Sentinel-6 altimetry: Impact on global mean sea level estimates. 2023 Ocean Surface Topography Science Team Meeting, San Juan, PR, AVISO, https://doi.org/10.24400/527896/a03-2023.3813.

Behrenfeld, M. J., and Coauthors, 2006: Climate-driven trends in contemporary ocean productivity. *Nature*, **444**, 752–755, https://doi.org/10.1038/nature05317.

—— , and Coauthors, 2015: Reevaluating ocean warming impacts on global phytoplankton. *Nat. Climate Change*, **6**, 323–330, https://doi.org/10.1038/nclimate2838.

Boyer, T. P., and Coauthors, 2018: World Ocean Database 2018. NOAA Atlas NESDIS 87, 207 pp., https://www.nodc.noaa.gov/OC5/WOD/pr_wod.html.

Brown, S., S. Desai, and C. S. Chae, 2023: Progress on the wet path delay correction: Historical, current and future. 2023 Ocean Surface Topography Science Team Meeting, San Juan, PR, AVISO, https://doi.org/10.24400/527896/a03-2023.3701.

Bryden, H. L., W. E. Johns, B. A. King, G. McCarthy, E. L. McDonagh, B. I. Moat, and D. A. Smeed, 2020: Reduction in ocean heat transport at 26°N since 2008 cools the eastern subpolar gyre of the North Atlantic Ocean. *J. Climate*, **33**, 1677–1689, https://doi.org/10.1175/JCLI-D-19-0323.1.

Caesar, L., S. Rahmstorf, A. Robinson, G. Fuelner, and V. Saba, 2018: Observed fingerprint of a weakening Atlantic Ocean overturning circulation. *Nature*, **556**, 191–196, https://doi.org/10.1038/s41586-018-0006-5.

—— , G. D. McCarthy, D. J. R. Thornalley, N. Cahill, and S. Rahmstorf, 2021: Current Atlantic meridional overturning circulation weakest in last millennium. *Nat. Geosci.*, **14**, 118–120, https://doi.org/10.1038/s41561-021-00699-z.

Caínzos, V., A. Hernández-Guerra, G. D. McCarthy, E. L. McDonagh, M. Cubas Armas, and M. D. Pérez-Hernández, 2022: Thirty years of GOSHIP and WOCE data: Atlantic overturning of mass, heat, and freshwater transport. *Geophys. Res. Lett.*, **49**, e2021GL096527, https://doi.org/10.1029/2021GL096527.

Carter, B. R., and Coauthors, 2019: Pacific anthropogenic carbon between 1991 and 2017. *Global Biogeochem. Cycles*, **33**, 597–617, https://doi.org/10.1029/2018GB006154.

Chambers, D. P., A. Cazenave, N. Champollion, H. Dieng, W. Llovel, R. Forsberg, K. von Schuckmann, and Y. Wada, 2017: Evaluation of the global mean sea level budget between 1993 and 2014. *Surv. Geophys.*, **38**, 309–327, https://doi.org/10.1007/s10712-016-9381-3.

Chen, J., B. Tapley, C. Wilson, A. Cazenave, K. W. Seo, and J. S. Kim, 2020: Global ocean mass change from GRACE and GRACE Follow-On and altimeter and Argo measurements. *Geophys. Res. Lett.*, **47**, e2020GL090656, https://doi.org/10.1029/2020GL090656.

Cheng, L., J. Zhu, R. Cowley, T. Boyer, and S. Wijffels, 2014: Time, probe type, and temperature variable bias corrections to historical expendable bathythermograph observations. *J. Atmos. Oceanic Technol.*, **31**, 1793–1825, https://doi.org/10.1175/JTECH-D-13-00197.1.

—— , and Coauthors, 2024: New record ocean temperatures and other related climate indicators in 2023. *Adv. Atmos. Sci.*, **41**, 1068–1082, https://doi.org/10.1007/s00376-024-3378-5.

Davila, X., G. Gebbie, A. Brakstad, S. K. Lauvset, E. L. McDonagh, J. Schwinger, and A. Olsen, 2022: How is the ocean anthropogenic carbon reservoir filled? *Global Biogeochem. Cycles*, **36**, e2021GB007055, https://doi.org/10.1029/2021GB007055.

de Boyer Montégut, C., G. Madec, A. S. Fischer, A. Lazar, and D. Ludicone, 2004: Mixed layer depth over the global ocean: An examination of profile data and a profile-based climatology. *J. Geophys. Res.*, **109**, C12003, https://doi.org/10.1029/2004JC002378.

Deser, C., M. A. Alexander, S.-P. Xie, and A. S. Phillips, 2010: Sea surface temperature variability: Patterns and mechanisms. *Annu. Rev. Mar. Sci.*, **2**, 115–143, https://doi.org/10.1146/annurev-marine-120408-151453.

DeVries, T., and Coauthors, 2023: Magnitude, trends, and variability of the global ocean carbon sink from 1985 to 2018. *Global Biogeochem. Cycles*, **37**, e2023GB007780, https://doi.org/10.1029/2023GB007780.

Dierssen, H. M., 2010: Perspectives on empirical approaches for ocean color remote sensing of chlorophyll in a changing climate. *Proc. Natl. Acad. Sci. USA*, **107**, 17073–17078, https://doi.org/10.1073/pnas.0913800107.

Dlugokencky, E. J., K. W. Thoning, X. Lan, and P. P. Tans, 2021: NOAA greenhouse gas reference from atmospheric carbon dioxide dry air mole fractions from the NOAA GML Carbon Cycle Cooperative Global Air Sampling Network. Accessed 19 January 2024, ftp://aftp.cmdl.noaa.gov/data/trace_gases/co2/flask/surface/.

Domingues, R., and Coauthors, 2015: Upper ocean response to Hurricane Gonzalo (2014): Salinity effects revealed by sustained and targeted observations from underwater gliders. *Geophys. Res. Lett.*, **42**, 7131–7138, https://doi.org/10.1002/2015GL065378.

—— , M. Baringer, and G. Goni, 2016: Remote sources for year-to-year changes in the seasonality of the Florida Current transport. *J. Geophys. Res. Oceans*, **121**, 7547–7559, https://doi.org/10.1002/2016JC012070.

—— , G. Goni, M. Baringer, and D. L. Volkov, 2018: What caused the accelerated sea level changes along the United States East Coast during 2010–2015? *Geophys. Res. Lett.*, **45**, 13 367–13 376, https://doi.org/10.1029/2018GL081183.

Dong, S., G. Goni, R. Domingues, F. Bringas, M. Goes, J. Christophersen, and M. Baringer, 2021: Synergy of in situ and satellite ocean observations in determining meridional heat transport in the Atlantic Ocean. *J. Geophys. Res. Oceans*, **126**, e2020JC017073, https://doi.org/10.1029/2020JC017073.

do Rosário Gomes, H., J. Goes, S. Matondkar, E. Buskey, S. Basu, S. Parab, and P. Thoppil, 2014: Massive outbreaks of *Noctiluca scintillans* blooms in the Arabian Sea due to spread of hypoxia. *Nat. Commun.*, **5**, 4862, https://doi.org/10.1038/ncomms5862.

Durack, P. J., and S. E. Wijffels, 2010: Fifty-year trends in global ocean salinities and their relationship to broad-scale warming. *J. Climate*, **23**, 4342–4362, https://doi.org/10.1175/2010JCLI3377.1.

—— , —— , and R. J. Matear, 2012: Ocean salinities reveal strong global water cycle intensification during 1950 to 2000. *Science*, **336**, 455–458, https://doi.org/10.1126/science.1212222.

Ezer, T., and L. P. Atkinson, 2014: Accelerated flooding along the U.S. East Coast: On the impact of sea-level rise, tides, storms, the Gulf Stream, and the North Atlantic Oscillations. *Earth's Future*, **2**, 362–382, https://doi.org/10.1002/2014EF000252.

Fairall, C. W., E. F. Bradley, J. E. Hare, A. A. Grachev, and J. B. Edson, 2003: Bulk parameterization of air–sea fluxes: Updates and verification for the COARE algorithm. *J. Climate*, **16**, 571–591, https://doi.org/10.1175/1520-0442(2003)016<0571:BPOASF>2.0.CO;2.

Fasullo, J. T., R. S. Nerem, and B. Hamlington, 2016: Is the detection of accelerated sea level rise imminent? *Sci. Rep.*, **6**, 31245, https://doi.org/10.1038/srep31245.

Ffield, A., 2007: Amazon and Orinoco River plumes and NBC rings: Bystanders or participants in hurricane events? *J. Climate*, **20**, 316–333, https://doi.org/10.1175/JCLI3985.1.

Field, C. B., M. J. Behrenfeld, J. T. Randerson, and P. Falkowski, 1998: Primary production of the biosphere: Integrating terrestrial and oceanic components. *Science*, **281**, 237–240, https://doi.org/10.1126/science.281.5374.237.

Fofonoff, N. P., and E. L. Lewis, 1979: A practical salinity scale. *J. Oceanogr. Soc. Japan*, **35**, 63–64, https://doi.org/10.1007/BF02108283.

Font, J., and Coauthors, 2013: SMOS first data analysis for sea surface salinity determination. *Int. J. Remote Sens.*, **34**, 3654–3670, https://doi.org/10.1080/01431161.2012.716541.

Fore, A. G., S. H. Yueh, W. Q. Tang, B. W. Stiles, and A. K. Hayashi, 2016: Combined active/passive retrievals of ocean vector wind and sea surface salinity with SMAP. IEEE Trans. *Geosci. Remote Sens.*, **54**, 7396–7404, https://doi.org/10.1109/TGRS.2016.2601486.

Franz, B. A., I. Cetinić, M. Gao, A. Siegel, and T. K. Westberry, 2023: Global ocean phytoplankton [in "State of the Climate in 2022"]. *Bull. Amer. Meteor. Soc.*, **104** (9), S184–S188, https://doi.org/10.1175/BAMS-D-23-0076.2.

—— , —— , A. Ibrahim, and A. Sayer, 2024: Anomalous trends in global ocean carbon concentrations following the 2022 eruptions of Hunga Tonga-Hunga Ha'apai. *Commun. Earth Environ.*, **5**, 247, https://doi.org/10.1038/s43247-024-01421-8.

Friedlingstein, P., and Coauthors, 2023: Global Carbon Budget 2023. *Earth Syst. Sci. Data*, **15**, 5301–5369, https://doi.org/10.5194/essd-15-5301-2023.

Fu, Y., F. Li, J. Karstensen, and C. Wang, 2020: A stable Atlantic meridional overturning circulation in a changing North Atlantic Ocean since the 1990s. *Sci. Adv.*, **6**, eabc7836, https://doi.org/10.1126/sciadv.abc7836.

—— , and Coauthors, 2023: Seasonality of the meridional overturning circulation in the subpolar North Atlantic. *Commun. Earth Environ.*, **4**, 181, https://doi.org/10.1038/s43247-023-00848-9.

Geider, R. J., H. L. MacIntyre, and T. M. Kana, 1997: Dynamic model of phytoplankton growth and acclimation: Responses of the balanced growth rate and the chlorophyll *a*: Carbon ratio to light, nutrient limitation and temperature. *Mar. Ecol. Prog. Ser.*, **148**, 187–200, https://doi.org/10.3354/meps148187.

Giglio, D., T. Sukianto, and M. Kuusela, 2024: Global ocean heat content anomalies and ocean heat uptake based on mapping Argo data using local Gaussian processes (3.0.0). Accessed 10 February 2024, https://doi.org/10.5281/zenodo.10645137.

Goes, J. I., and Coauthors, 2020: Ecosystem state change in the Arabian Sea fuelled by the recent loss of snow over the Himalayan-Tibetan Plateau region. *Sci. Rep.*, **10**, 7422, https://doi.org/10.1038/s41598-020-64360-2.

Goni, G. J., and W. E. Johns, 2003: Synoptic study of warm rings in the North Brazil Current retroflection region using satellite altimetry. *Interhemispheric Water Exchange in the Atlantic Ocean, G. J. Goni and P. Malanotte-Rizzoli, Eds., Elsevier Oceanography Series*, Vol. 68, Elsevier, 335–356, https://doi.org/10.1016/S0422-9894(03)80153-8.

—— , F. Bringas, and P. N. Di Nezio, 2011: Observed low frequency variability of the Brazil Current front. *J. Geophys. Res.*, **116**, C10037, https://doi.org/10.1029/2011JC007198.

Good, S. A., M. J. Martin, and N. A. Rayner, 2013: EN4: Quality controlled ocean temperature and salinity profiles and monthly objective analyses with uncertainty estimates. *J. Geophys. Res. Oceans*, **118**, 6704–6716, https://doi.org/10.1002/2013JC009067.

Gouretski, V., and L. Cheng, 2020: Correction for systematic errors in the global dataset of temperature profiles from mechanical bathythermographs. *J. Atmos. Oceanic Technol.*, **37**, 841–855, https://doi.org/10.1175/JTECH-D-19-0205.1.

Graff, J. R., T. K. Westberry, A. J. Milligan, M. B. Brown, G. Dall'Olmo, V. van Dongen-Vogels, K. M. Reifel, and M. J. Behrenfeld, 2015: Analytical phytoplankton carbon measurements spanning diverse ecosystems. *Deep-Sea Res. I*, **102**, 16–25, https://doi.org/10.1016/j.dsr.2015.04.006.

Gruber, N., and Coauthors, 2019: The oceanic sink for anthropogenic CO_2 from 1994 to 2007. *Science*, **363**, 1193–1199, https://doi.org/10.1126/science.aau5153.

Hakuba, M. Z., T. Frederikse, and F. W. Landerer, 2021: Earth's energy imbalance from the ocean perspective (2005–2019). Geophys. *Res. Lett.*, **48**, e2021GL093624, https://doi.org/10.1029/2021GL093624.

Hamlington, B. D., C. G. Piecuch, J. T. Reager, H. Chandanpurkar, T. Frederikse, R. S. Nerem, J. T. Fasullo, and S.-H. Cheon, 2020: Origin of interannual variability in global mean sea level. *Proc. Natl. Acad. Sci. USA*, **117**, 13 983–13 990, https://doi.org/10.1073/pnas.1922190117.

Hauck, J., and Coauthors, 2023: The Southern Ocean Carbon Cycle 1985–2018: Mean, seasonal cycle, trends, and storage. *Global Biogeochem. Cycles*, **37**, e2023GB007848, https://doi.org/10.1029/2023GB007848.

Held, I. M., and B. J. Soden, 2006: Robust responses of the hydrological cycle to global warming. *J. Climate*, **19**, 5686–5699, https://doi.org/10.1175/JCLI3990.1.

Hersbach, H., and Coauthors, 2018: ERA5 hourly data on single levels from 1959 to present. Copernicus Climate Change Service (C3S) Climate Data Store (CDS), accessed 2 January 2024, https://doi.org/10.24381/cds.adbb2d47.

Hobbs, W. R., and J. K. Willis, 2012: Midlatitude North Atlantic heat transport: A time series based on satellite and drifter data. *J. Geophys. Res.*, **117**, C01008, https://doi.org/10.1029/2011JC007039.

Hobday, A. J., and Coauthors, 2016: A hierarchical approach to defining marine heatwaves. *Prog. Oceanogr.*, **141**, 227–238, https://doi.org/10.1016/j.pocean.2015.12.014.

Holbrook, N. J., and Coauthors, 2019: A global assessment of marine heatwaves and their drivers. *Nat. Commun.*, **10**, 2624, https://doi.org/10.1038/s41467-019-10206-z.

Hu, C., Z. Lee, and B. Franz, 2012: Chlorophyll algorithms for oligotrophic oceans: A novel approach based on three-band reflectance difference. *J. Geophys. Res.*, **117**, C01011, https://doi.org/10.1029/2011JC007395.

—— , L. Feng, Z. Lee, B. A. Franz, S. W. Bailey, P. J. Werdell, and C. W. Proctor, 2019: Improving satellite global chlorophyll *a* data products through algorithm refinement and data recovery. *J. Geophys. Res. Oceans*, **124**, 1524–1543, https://doi.org/10.1029/2019JC014941.

Hu, Z.-Z., B. Huang, J. Zhu, A. Kumar, and M. J. McPhaden, 2019: On the variety of coastal El Niño events. *Climate Dyn.*, **52**, 7537–7552, https://doi.org/10.1007/s00382-018-4290-4.

Huang, B., and Coauthors, 2015: Extended Reconstructed Sea Surface Temperature version 4 (ERSST.v4), Part I. Upgrades and intercomparisons. *J. Climate*, **28**, 911–930, https://doi.org/10.1175/JCLI-D-14-00006.1.

—— , and Coauthors, 2017: Extended Reconstructed Sea Surface Temperature version 5 (ERSSTv5), Upgrades, validations, and intercomparisons. *J. Climate*, **30**, 8179–8205, https://doi.org/10.1175/JCLI-D-16-0836.1.

—— , and Coauthors, 2020: Uncertainty estimates for sea surface temperature and land surface air temperature in NOAAGlobalTemp version 5. *J. Climate*, **33**, 1351–1379, https://doi.org/10.1175/JCLI-D-19-0395.1.

—— , C. Liu, V. Banzon, E. Freeman, G. Graham, B. Hankins, T. Smith, and H.-M. Zhang, 2021: Improvements of the Daily Optimum Interpolation Sea Surface Temperature (DOISST) version 2.1. *J. Climate*, **34**, 2923–2939, https://doi.org/10.1175/JCLI-D-20-0166.1.

Hughes, T., and Coauthors, 2017: Global warming and recurrent mass bleaching of corals. *Nature*, **543**, 373–377, https://doi.org/10.1038/nature21707.

IPCC, 2021: Climate Change 2021: The Physical Science Basis. V. Masson-Delmotte et al., Eds., Cambridge University Press, 2391 pp., https://doi.org/10.1017/9781009157896.

Ishii, M., Y. Fukuda, S. Hirahara, S. Yasui, T. Suzuki, and K. Sato, 2017: Accuracy of global upper ocean heat content estimation expected from present observational datasets. *SOLA*, **13**, 163–167, https://doi.org/10.2151/sola.2017-030.

Jiang, S., C. Zhu, Z.-Z. Hu, N. Jiang, and F. Zheng, 2023: Triple-dip La Niñas in 2020-2022: Understanding the role of the annual cycle in the tropical Pacific SST. Environ. *Res. Lett.*, **18**, 084002, https://doi.org/10.1088/1748-9326/ace274.

Johns, W. E., S. Elipot, D. A. Smeed, B. Moat, B. King, D. L. Volkov, and R. H. Smith, 2023: Towards two decades of Atlantic Ocean mass and heat transports at 26.5°N. Philos. *Trans. Roy. Soc.*, **A381**, 20220188, https://doi.org/10.1098/rsta.2022.0188.

Johnson, G. C., and J. M. Lyman, 2012: Sea surface salinity [in "State of the Climate in 2011"]. *Bull. Amer. Meteor. Soc.*, **93** (7), S68–S69, https://doi.org/10.1175/2012BAMSStateoftheClimate.1.

—— , —— , J. K. Willis, T. Boyer, J. Antonov, S. A. Good, C. M. Domingues, and N. Bindoff, 2014: Ocean heat content [in "State of the Climate in 2013"]. *Bull. Amer. Meteor. Soc.*, **95** (7), S54–S57, https://doi.org/10.1175/2014BAMSStateoftheClimate.1.

—— , and Coauthors, 2015: Ocean heat content [in "State of the Climate in 2014"]. *Bull. Amer. Meteor. Soc.*, **96** (7), S64–S66, https://doi.org/10.1175/2015BAMSStateoftheClimate.1.

—— , J. Reagan, J. M. Lyman, T. Boyer, C. Schmid, and R. Locarnini, 2020: Salinity [in "State of the Climate in 2019"]. *Bull. Amer. Meteor. Soc.*, **101** (8), S129–S183, https://doi.org/10.1175/BAMS-D-20-0105.1.

—— , and Coauthors, 2022: Ocean heat content [in "State of the Climate in 2021"]. *Bull. Amer. Meteor. Soc.*, **103** (8), S153–S157, https://doi.org/10.1175/2022BAMSStateoftheClimate.1.

Kato, S., and Coauthors, 2018: Surface Irradiances of Edition 4.0 Clouds and the Earth's Radiant Energy System (CERES) Energy Balanced and Filled (EBAF) data product. *J. Climate*, **31**, 4501–4527, https://doi.org/10.1175/JCLI-D-17-0523.1.

Kennedy, J. J., N. A. Rayner, C. P. Atkinson, and R. E. Killick, 2019: An ensemble data set of sea surface temperature change from 1850: The Met Office Hadley Centre HadSST.4.0.0.0 data set. *J. Geophys. Res. Atmos.*, **124**, 7719–7763, https://doi.org/10.1029/2018JD029867.

Khatiwala, S., F. Primeau, and T. Hall, 2009: Reconstruction of the history of anthropogenic CO_2 concentrations in the ocean. *Nature*, **462**, 346–349, https://doi.org/10.1038/nature08526.

Kramer, S. J., D. A. Siegel, S. Maritorena, and D. Catlett, 2022: Modeling surface ocean phytoplankton pigments from hyperspectral remote sensing reflectance on global scales. *Remote Sens. Environ.*, **270**, 112879, https://doi.org/10.1016/j.rse.2021.112879.

Kumar, P., B. Hamlington, S. Cheon, W. Han, and P. Thompson, 2020: 20th century multivariate Indian Ocean regional sea level reconstruction. *J. Geophys. Res. Oceans*, **125**, e2020JC016270, https://doi.org/10.1029/2020JC016270.

Landschützer, P., N. Gruber, D. C. E. Bakker, U. Schuster, S. Nakaoka, M. R. Payne, T. P. Sasse, and J. Zeng, 2013: A neural network-based estimate of the seasonal to inter-annual variability of the Atlantic Ocean carbon sink. *Biogeosciences*, **10**, 7793–7815, https://doi.org/10.5194/bg-10-7793-2013.

—— , —— , —— , and —— , 2014: Recent variability of the global ocean carbon sink. *Global Biogeochem. Cycles*, **28**, 927–949, https://doi.org/10.1002/2014GB004853.

Lange, P. K., and Coauthors, 2020: Radiometric approach for the detection of picophytoplankton assemblages across oceanic fronts. *Opt. Express*, **28**, 25 682–25 705, https://doi.org/10.1364/OE.398127.

Lauvset, S. K., and Coauthors, 2016: A new global interior ocean mapped climatology: The 1° x 1° GLODAP version 2. *Earth Syst. Sci. Data*, **8**, 325–340, https://doi.org/10.5194/essd-8-325-2016.

—— , A. Brakstad, K. Våge, A. Olsen, E. Jeansson, and K. A. Mork, 2018: Continued warming, salinification and oxygenation of the Greenland Sea gyre. *Tellus*, **70A** (1), 1–9, https://doi.org/10.1080/16000870.2018.1476434.

Leuliette, E. W., and J. K. Willis, 2011: Balancing the sea level budget. *Oceanography*, **24** (2), 122–129, https://doi.org/10.5670/oceanog.2011.32.

Le Vine, D. M., E. P. Dinnat, G. S. E. Lagerloef, P. de Matthaeis, S. Abraham, C. Utku, and H. Kao, 2014: Aquarius: Status and recent results. *Radio Sci.*, **49**, 709–720, https://doi.org/10.1002/2014RS005505.

Levitus, S., and Coauthors, 2012: World ocean heat content and thermosteric sea level change (0–2000 m), 1955–2010. *Geophys. Res. Lett.*, **39**, L10603, https://doi.org/10.1029/2012GL051106.

Li, F., and Coauthors, 2021: Subpolar North Atlantic western boundary density anomalies and the Meridional Overturning Circulation. *Nat. Commun.*, **12**, 3002, https://doi.org/10.1038/s41467-021-23350-2.

Li, G., L. Cheng, J. Zhu, K. E. Trenberth, M. E. Mann, and J. P. Abraham, 2020: Increasing ocean stratification over the past half-century. *Nat. Climate Change*, **10**, 1116–1123, https://doi.org/10.1038/s41558-020-00918-2.

Li, L., R. W. Schmitt, C. C. Ummenhofer, and K. B. Karnauskas, 2016: North Atlantic salinity as a predictor of Sahel rainfall. *Sci. Adv.*, **2**, e1501588, https://doi.org/10.1126/sciadv.1501588.

Li, X., Z.-Z. Hu, M. J. McPhaden, C. Zhu, and Y. Liu, 2023: Triple-dip La Niñas in 1998–2001 and 2020–2023: Impact of mean state changes. *J. Geophys. Res. Atmos.*, **128**, e2023JD038843, https://doi.org/10.1029/2023JD038843.

Loeb, N. G., and Coauthors, 2018: Clouds and the Earth's Radiant Energy System (CERES) Energy Balanced and Filled (EBAF) top-of-atmosphere (TOA) edition-4.0 data product. *J. Climate*, **31**, 895–918, https://doi.org/10.1175/JCLI-D-17-0208.1.

—— , G. C. Johnson, T. J. Thorsen, J. M. Lyman, F. G. Rose, and S. Kato, 2021: Satellite and ocean data reveal marked increase in Earth's heating rate. *Geophys. Res. Lett.*, **48**, e2021GL093047, https://doi.org/10.1029/2021GL093047.

Lozier, M. S., and Coauthors, 2017: Overturning in the Subpolar North Atlantic Program: A new international ocean observing system. *Bull. Amer. Meteor. Soc.*, **98**, 737–752, https://doi.org/10.1175/BAMS-D-16-0057.1.

—— , and Coauthors, 2019: A sea change in our view of overturning in the subpolar North Atlantic. *Science*, **363**, 516–521, https://doi.org/10.1126/science.aau6592.

Lumpkin, R., and S. L. Garzoli, 2005: Near-surface circulation in the tropical Atlantic Ocean. *Deep-Sea Res. I*, **52**, 495–518, https://doi.org/10.1016/j.dsr.2004.09.001.

—— , and —— , 2011: Interannual to decadal changes in the western South Atlantic's surface circulation. *J. Geophys. Res.*, **116**, C01014, https://doi.org/10.1029/2010JC006285.

—— , G. Goni, and K. Dohan, 2012: Surface currents [in "State of the Climate in 2011"]. *Bull. Amer. Meteor. Soc.*, **93** (7), S75–S78, https://doi.org/10.1175/2012BAMSStateoftheClimate.1.

—— , F. Bringas, G. Goni, and B. Qiu, 2023: Surface currents [in "State of the Climate in 2022"]. *Bull. Amer. Meteor. Soc.*, **104** (9), S177–S180, https://doi.org/10.1175/BAMS-D-23-0076.2.

Lyman, J. M., and G. C. Johnson, 2014: Estimating global ocean heat content changes in the upper 1800 m since 1950 and the influence of climatology choice. *J. Climate*, **27**, 1945–1957, https://doi.org/10.1175/JCLI-D-12-00752.1.

—— , and —— , 2023: Global high-resolution random forest regression maps of ocean heat content anomalies using in situ and satellite data. *J. Atmos. Oceanic Technol.*, **40**, 575–586, https://doi.org/10.1175/JTECH-D-22-0058.1.

Mantua, N. J., and S. R. Hare, 2002: The Pacific decadal oscillation. *J. Oceanogr.*, **58**, 35–44, https://doi.org/10.1023/A:1015820616384.

Maritorena, S., O. Hembise Fanton d'Andon, A. Mangin, and D. A. Siegel, 2010: Merged satellite ocean color data products using a bio-optical model: Characteristics, benefits and issues. *Remote Sens. Environ.*, **114**, 1791–1804, https://doi.org/10.1016/j.rse.2010.04.002.

Marti, F., and Coauthors, 2022: Monitoring the ocean heat content change and the Earth energy imbalance from space altimetry and space gravimetry. *Earth Syst. Sci. Data*, **14**, 229–249, https://doi.org/10.5194/essd-14-229-2022.

McCarthy, G., and Coauthors, 2015: Measuring the Atlantic meridional overturning circulation at 26°N. Prog. *Oceanogr.*, **130**, 91–111, https://doi.org/10.1016/j.pocean.2014.10.006.

McKinna, L. I. W., P. J. Werdell, and C. W. Proctor, 2016: Implementation of an analytical Raman scattering correction for satellite ocean-color processing. *Opt. Express*, **24**, A1123–A1137, https://doi.org/10.1364/OE.24.0A1123.

Moat, B. I., and Coauthors, 2020: Pending recovery in the strength of the meridional overturning circulation at 26°N. Ocean Sci., **16**, 863–874, https://doi.org/10.5194/os-16-863-2020.

—— , D. Smeed, D. Rayner, W. E. Johns, R. H. Smith, D. L. Volkov, M. O. Baringer, and J. Collins, 2023: Atlantic meridional overturning circulation observed by the RAPID-MOCHA-WBTS (RAPID-Meridional Overturning Circulation and Heatflux Array-Western Boundary Time Series) array at 26N from 2004 to 2022 (v2022.1). Accessed 18 January 2024, https://doi.org/10.5285/04c79ece-3186-349a-e063-6c86abc0158c.

Mulet, S., and Coauthors, 2021: The new CNES-CLS18 global mean dynamic topography. *Ocean Sci.*, **17**, 789–808, https://doi.org/10.5194/os-17-789-2021.

Müller, J. D., and Coauthors, 2023: Decadal trends in the oceanic storage of anthropogenic carbon from 1994 to 2014. *AGU Adv.*, **4**, e2023AV000875, https://doi.org/10.1029/2023AV000875.

Nerem, R. S., D. P. Chambers, E. W. Leuliette, G. T. Mitchum, and B. S. Giese, 1999: Variations in global mean sea level associated with the 1997–1998 ENSO event: Implications for measuring long term sea level change. *Geophys. Res. Lett.*, **26**, 3005–3008, https://doi.org/10.1029/1999GL002311.

—— , B. D. Beckley, J. T. Fasullo, B. D. Hamlington, D. Masters, and G. T. Mitchum, 2018: Climate-change–driven accelerated sea-level rise detected in the altimeter era. *Proc. Natl. Acad. Sci. USA*, **115**, 2022–2025, https://doi.org/10.1073/pnas.1717312115.

Oliver, E. C. J., J. A. Benthuysen, S. Darmaraki, M. G. Donat, A. J. Hobday, N. J. Holbrook, R. W. Schlegel, and A. Sen Gupta, 2021: Marine heatwaves. *Annu. Rev. Mar. Sci.*, **13**, 313–342, https://doi.org/10.1146/annurev-marine-032720-095144.

O'Reilly, J. E., and P. J. Werdell, 2019: Chlorophyll algorithms for ocean color sensors – OC4, OC5 & OC6. *Remote Sens. Environ.*, **229**, 32–47, https://doi.org/10.1016/j.rse.2019.04.021.

Pahlevan, N., B. Smith, C. Binding, D. Gurlin, L. Li, M. Bresciani, and C. Giardino, 2021: Hyperspectral retrievals of phytoplankton absorption and chlorophyll-*a* in inland and nearshore coastal waters. *Remote Sens. Environ.*, **253**, 112200, https://doi.org/10.1016/j.rse.2020.112200.

Palmer, M. D., K. Haines, S. F. B. Tett, and T. J. Ansell, 2007: Isolating the signal of ocean global warming. *Geophys. Res. Lett.*, **34**, L23610, https://doi.org/10.1029/2007GL031712.

Pita, I., M. Goes, D. L. Volkov, S. Dong, G. Goni, and M. Cirano, 2024: An ARGO and XBT observing system for the Atlantic Meridional Overturning Circulation and Meridional Heat Transport (AXMOC) at 22.5°S. J. Geophys. *Res. Oceans*, **129**, e2023JC020010, https://doi.org/10.1029/2023JC020010.

Purkey, S. G., and G. C. Johnson, 2010: Warming of global abyssal and deep Southern Ocean waters between the 1990s and 2000s: Contributions to global heat and sea-level rise budgets. *J. Climate*, **23**, 6336–6351, https://doi.org/10.1175/2010JCLI3682.1.

Qiu, B., and S. Chen, 2021: Revisit of the occurrence of the Kuroshio Large Meander south of Japan. *J. Phys. Oceanogr.*, **51**, 3679–3694, https://doi.org/10.1175/JPO-D-21-0167.1.

——, ——, N. Schneider, E. Oka, and S. Sugimoto, 2020: On the reset of the wind-forced decadal Kuroshio extension variability in late 2017. *J. Climate*, **33**, 10813–10828, https://doi.org/10.1175/JCLI-D-20-0237.1.

Rahmstorf, S., J. Box, G. Feulner, M. E. Mann, A. Robinson, S. Rutherford, and E. J. Schaffernicht, 2015: Exceptional twentieth-century slowdown in Atlantic Ocean overturning circulation. *Nat. Climate Change*, **5**, 475–480, https://doi.org/10.1038/nclimate2554.

Rasmusson, E. M., and T. H. Carpenter, 1982: Variation in tropical sea surface temperature and surface wind fields associated with Southern Oscillation/El Niño. *Mon. Wea. Rev.*, **110**, 354–384, https://doi.org/10.1175/1520-0493(1982)110<0354:VITSST>2.0.CO;2.

Rayner, N. A., D. E. Parker, E. B. Horton, C. K. Folland, L. V. Alexander, D. P. Rowell, E. C. Kent, and A. Kaplan, 2003: Global analyses of sea surface temperature, sea ice, and night marine air temperature since the late nineteenth century. *J. Geophys. Res.*, **108**, 4407, https://doi.org/10.1029/2002JD002670.

Reagan, J., T. Boyer, C. Schmid, and R. Locarnini, 2022: Subsurface salinity [in "State of the Climate in 2021"]. *Bull. Amer. Meteor. Soc.*, **103** (8), S160–S162, https://doi.org/10.1175/BAMS-D-22-0072.1.

——, ——, ——, and ——, 2023: Subsurface salinity [in "State of the Climate in 2022"]. *Bull. Amer. Meteor. Soc.*, **104** (9), S165–S167, https://doi.org/10.1175/BAMS-D-23-0076.2.

Regnier, P., L. Resplandy, R. G. Najjar, and P. Ciais, 2022: The land-to-ocean loops of the global carbon cycle. *Nature*, **603**, 401–410, https://doi.org/10.1038/s41586-021-04339-9.

Ren, L., K. Speer, and E. P. Chassignet, 2011: The mixed layer salinity budget and sea ice in the Southern Ocean. *J. Geophys. Res.*, **116**, C08031, https://doi.org/10.1029/2010JC006634.

Reynolds, R. W., T. M. Smith, C. Liu, D. B. Chelton, K. S. Casey, and M. G. Schlax, 2007: Daily high-resolution-blended analyses for sea surface temperature. *J. Climate*, **20**, 5473–5496, https://doi.org/10.1175/2007JCLI1824.1.

Riser, S. C., and Coauthors, 2016: Fifteen years of ocean observations with the global Argo array. *Nat. Climate Change*, **6**, 145–153, https://doi.org/10.1038/nclimate2872.

Rödenbeck, C., and Coauthors, 2015: Data-based estimates of the ocean carbon sink variability – First results of the Surface Ocean pCO_2 Mapping intercomparison (SOCOM). *Biogeosciences*, **12**, 7251–7278, https://doi.org/10.5194/bg-12-7251-2015.

Roemmich, D., and J. Gilson, 2009: The 2004–2008 mean and annual cycle of temperature, salinity, and steric height in the global ocean from the Argo Program. *Prog. Oceanogr.*, **82**, 81–100, https://doi.org/10.1016/j.pocean.2009.03.004.

Sabine, C. L., and Coauthors, 2004: The oceanic sink for anthropogenic CO_2. *Science*, **305**, 367–371, https://doi.org/10.1126/science.1097403.

Saji, N. H., B. N. Goswami, P. N. Vinayachandran, and T. Yamagata, 1999: A dipole mode in the tropical Indian Ocean. *Nature*, **401**, 360–363, https://doi.org/10.1038/43854.

Schlesinger, M. E., and N. Ramankutty, 1994: An oscillation in the global climate system of period 65–70 years. *Nature*, **367**, 723–726, https://doi.org/10.1038/367723a0.

Schmidtko, S., G. C. Johnson, and J. M. Lyman, 2013: MIMOC: A global monthly isopycnal upper-ocean climatology with mixed layers. *J. Geophys. Res. Oceans*, **118**, 1658–1672, https://doi.org/10.1002/jgrc.20122.

Schmitt, R. W., 1995: The ocean component of the global water cycle. *Rev. Geophys.*, **33**, 1395–1409, https://doi.org/10.1029/95RG00184.

Siegel, D. A., S. Maritorena, N. B. Nelson, M. J. Behrenfeld, and C. R. McClain, 2005: Colored dissolved organic matter and its influence on the satellite-based characterization of the ocean biosphere. *Geophys. Res. Lett.*, **32**, L20605, https://doi.org/10.1029/2005GL024310.

——, and Coauthors, 2013: Regional to global assessments of phytoplankton dynamics from the SeaWiFS mission. *Remote Sens. Environ.*, **135**, 77–91, https://doi.org/10.1016/j.rse.2013.03.025.

——, T. DeVries, I. Cetinić, and K. M. Bisson, 2023: Quantifying the ocean's biological pump and its carbon cycle impacts on global scales. *Annu. Rev. Mar. Sci.*, **15**, 329–356, https://doi.org/10.1146/annurev-marine-040722-115226.

Skliris, N., R. Marsh, S. A. Josey, S. A. Good, C. Liu, and R. P. Allan, 2014: Salinity changes in the World Ocean since 1950 in relation to changing surface freshwater flux. *Climate Dyn.*, **43**, 709–736, https://doi.org/10.1007/s00382-014-2131-7.

——, J. D. Zika, G. Nurser, S. A. Josey, and R. Marsh, 2016: Global water cycle amplifying at less than the Clausius-Clapeyron rate. *Sci. Rep.*, **6**, 38752, https://doi.org/10.1038/srep38752.

Smeed, D. A., and Coauthors, 2018: The North Atlantic Ocean is in a state of reduced overturning. *Geophys. Res. Lett.*, **45**, 1527–1533, https://doi.org/10.1002/2017GL076350.

Smith, K. E., M. T. Burrows, A. J. Hobday, A. Sen Gupta, P. J. Moore, M. Thomsen, T. Wernberg, and D. A. Smale, 2021: Socioeconomic impacts of marine heatwaves: Global issues and opportunities. *Science*, **374**, eabj3593, https://doi.org/10.1126/science.abj3593.

——, and Coauthors, 2023: Biological impacts of marine heatwaves. *Annu. Rev. Mar. Sci.*, **15**, 119–145, https://doi.org/10.1146/annurev-marine-032122-121437.

Stackhouse, P. W., D. P. Kratz, G. R. McGarragh, S. K. Gupta, and E. B. Geier, 2006: Fast Longwave and Shortwave Radiative Flux (FLASHFlux) products from CERES and MODIS measurements. 12th Conf. on Atmospheric Radiation, Madison, WI, Amer. Meteor. Soc., P1.10, https://ams.confex.com/ams/Madison2006/techprogram/paper_113479.htm.

Sweet, W. V., J. Park, J. J. Marra, C. Zervas, and S. Gill, 2014: Sea level rise and nuisance flood frequency changes around the United States. NOAA Tech. Rep. NOS CO-OPS 073, 66 pp., https://tidesandcurrents.noaa.gov/publications/NOAA_Technical_Report_NOS_COOPS_073.pdf.

Talley, L. D., 2002: Salinity patterns in the ocean. *The Earth System: Physical and Chemical Dimensions of Global Environmental Change*, Vol. 1, Encyclopedia of Global Environmental Change, M. C. MacCracken and J. S. Perry, Eds., John Wiley and Sons, 629–640.

Twedt, K., N. Lei, X. Xiong, A. Angal, S. Li, T. Chang, and J. Sun, 2022: On-orbit calibration and performance of NOAA-20 VIIRS reflective solar bands. *IEEE Trans. Geosci. Remote Sens.*, **60**, 1–13, https://doi.org/10.1109/TGRS.2021.3108970.

Volkov, D. L., S.-K. Lee, R. Domingues, H. Zhang, and M. Goes, 2019: Interannual sea level variability along the southeastern seaboard of the United States in relation to the gyre-scale heat divergence in the North Atlantic. *Geophys. Res. Lett.*, **46**, 7481–7490, https://doi.org/10.1029/2019GL083596.

—— , R. Domingues, C. S. Meinen, R. Garcia, M. Baringer, G. Goni, and R. H. Smith, 2020: Inferring Florida Current volume transport from satellite altimetry. *J. Geophys. Res. Oceans*, **125**, e2020JC016763, https://doi.org/10.1029/2020JC016763.

—— , K. Zhang, W. E. Johns, J. K. Willis, W. Hobbs, M. Goes, H. Zhang, and D. Menemenlis, 2023a: Atlantic meridional overturning circulation increases flood risk along the United States southeast coast. *Nat. Commun.*, **14**, 5095, https://doi.org/10.1038/s41467-023-40848-z.

—— , and Coauthors, 2023b: Meridional overturning circulation and heat transport in the Atlantic Ocean [in "State of the Climate in 2022"]. *Bull. Amer. Meteor. Soc.*, **104** (9), S181–S184, https://doi.org/10.1175/BAMS-D-23-0076.2.

von Schuckmann, K., and Coauthors, 2023: Heat stored in the Earth system 1960–2020: Where does the energy go? *Earth Syst. Sci. Data*, **15**, 1675–1709, https://doi.org/10.5194/essd-15-1675-2023.

Von Storch, H., and F. W. Zwiers, 1999: Statistical Analysis in Climate Research. Cambridge University Press, 484 pp.

Walsh, K. J. E., and Coauthors, 2016: Tropical cyclones and climate change. *Wiley Interdiscip. Rev.: Climate Change*, **7**, 65–89, https://doi.org/10.1002/wcc.371.

Wanninkhof, R., 2014: Relationship between wind speed and gas exchange over the ocean revisited. *Limnol. Oceanogr. Methods*, **12**, 351–362, https://doi.org/10.4319/lom.2014.12.351.

Waugh, D. W., T. M. Hall, B. I. McNeil, R. Key, and R. J. Matear, 2006: Anthropogenic CO_2 in the oceans estimated using transit time distributions. *Tellus*, **58B**, 376–389, https://doi.org/10.1111/j.1600-0889.2006.00222.x.

Weijer, W., W. Cheng, O. A. Garuba, A. Hu, and B. T. Nadiga, 2020: CMIP6 models predict significant 21st century decline of the Atlantic meridional overturning circulation. *Geophys. Res. Lett.*, **47**, e2019GL086075, https://doi.org/10.1029/2019GL086075.

Werdell, P. J., and L. I. McKinna, 2019: Sensitivity of inherent optical properties from ocean reflectance inversion models to satellite instrument wavelength suites. *Front. Earth Sci.*, **7**, 54, https://doi.org/10.3389/feart.2019.00054.

—— , and Coauthors, 2013: Generalized ocean color inversion model for retrieving marine inherent optical properties. *Appl. Opt.*, **52**, 2019–2037, https://doi.org/10.1364/AO.52.002019.

—— , and Coauthors, 2019: The Plankton, Aerosol, Cloud, Ocean Ecosystem mission: Status, science, advances. *Bull. Amer. Meteor. Soc.*, **100**, 1775–1794, https://doi.org/10.1175/BAMS-D-18-0056.1.

Westberry, T. K., and Coauthors, 2016: Annual cycles of phytoplankton biomass in the subarctic Atlantic and Pacific Ocean. *Global Biogeochem. Cycles*, **30**, 175–190, https://doi.org/10.1002/2015GB005276.

Wiese, D. N., D.-N. Yuan, C. Boening, F. W. Landerer, and M. M. Watkins, 2022: JPL GRACE and GRACE-FO Mascon Ocean, Ice, and Hydrology Equivalent HDR Water Height RL06.1M CRI Filtered version 3.0. PODAAC, accessed 13 February 2024, https://doi.org/10.5067/TEMSC-3MJ62.

Willis, J. K., 2010: Can in situ floats and satellite altimeters detect long-term changes in Atlantic Ocean overturning? *Geophys. Res. Lett.*, **37**, L06602, https://doi.org/10.1029/2010GL042372.

—— , and W. R. Hobbs, 2024: Atlantic meridional overturning circulation near 41N from altimetry and Argo observations. Zenodo, accessed 10 January 2024, https://doi.org/10.5281/zenodo.8170366.

Wolter, K., and M. S. Timlin, 1998: Measuring the strength of ENSO events: How does 1997/98 rank? *Weather*, **53**, 315–324, https://doi.org/10.1002/j.1477-8696.1998.tb06408.x.

Woosley, R. J., F. J. Millero, and R. Wanninkhof, 2016: Rapid anthropogenic changes in CO_2 and pH in the Atlantic Ocean: 2003–2014. *Global Biogeochem. Cycles*, **30**, 70–90, https://doi.org/10.1002/2015GB005248.

Worthington, E. L., B. I. Moat, D. A. Smeed, J. V. Mecking, R. Marsh, and G. D. McCarthy, 2021: A 30-year reconstruction of the Atlantic meridional overturning circulation shows no decline. *Ocean Sci.*, **17**, 285–299, https://doi.org/10.5194/os-17-285-2021.

Wüst, G., 1936: Oberflächensalzgehalt, Verdunstung und Niederschlag auf dem Weltmeere. Länderkundliche Forschung: Festschrift zur Vollendung des sechzigsten Lebensjahres Norbert Krebs, J. Engelhorns Nachfahren, 347–359.

Xie, P., and Coauthors, 2014: An in situ-satellite blended analysis of global sea surface salinity. *J. Geophys. Res. Oceans*, **119**, 6140–6160, https://doi.org/10.1002/2014JC010046.

Yashayaev, I., and J. W. Loder, 2017: Further intensification of deep convection in the Labrador Sea in 2016. *Geophys. Res. Lett.*, **44**, 1429–1438, https://doi.org/10.1002/2016GL071668.

Yin, X., B. Huang, Z.-Z. Hu, D. Chan, and H.-M. Zhang, 2023: Sea-surface temperatures [in "State of the Climate in 2022"]. *Bull. Amer. Meteor. Soc.*, **104** (9), S153–S156, https://doi.org/10.1175/BAMS-D-23-0076.2.

Yu, L., 2011: A global relationship between the ocean water cycle and near-surface salinity. *J. Geophys. Res.*, **116**, C10025, https://doi.org/10.1029/2010JC006937.

—— , 2019: Global air–sea fluxes of heat, fresh water, and momentum: Energy budget closure and unanswered questions. *Annu. Rev. Mar. Sci.*, **11**, 227–248, https://doi.org/10.1146/annurev-marine-010816-060704.

—— , and R. A. Weller, 2007: Objectively analyzed air–sea heat fluxes for the global ice-free oceans (1981–2005). Bull. *Amer. Meteor. Soc.*, **88**, 527–540, https://doi.org/10.1175/BAMS-88-4-527.

Zhu, Y., and Coauthors, 2022: Perturbations in stratospheric aerosol evolution due to the water-rich plume of the 2022 Hunga-Tonga eruption. *Commun. Earth Environ.*, **3**, 248, https://doi.org/10.1038/s43247-022-00580-w.

Zweng, M. M., and Coauthors, 2018: Salinity. Vol. 2, World Ocean Atlas 2018, NOAA Atlas NESDIS 82, 50 pp., https://www.ncei.noaa.gov/sites/default/files/2020-04/woa18_vol2.pdf.